Design of Hydrogels for Extrusion-based 3D Bioprinting with Excellent Spatial Resolution and High Cell Viability

Zur Erlangung des akademischen Grades einer
DOKTORIN DER INGENIEURWISSENSCHAFTEN (DR.-ING.)

von der KIT-Fakultät für Chemieingenieurwesen und Verfahrenstechnik des
Karlsruher Instituts für Technologie (KIT)
genehmigte

DISSERTATION

von
Dipl.-Ing. Bruna Regina Maciel
aus Cascavel, Brasilien

Tag der mündlichen Prüfung: 17.11.2023

Erstgutachter: Prof. Dr. Norbert Willenbacher
Zweitgutachterin: Prof. Dr. Ute Schepers

Acknowledgements

So many people contributed in different ways along the years so that I could be where I am now. Here goes an attempt of expressing my gratitude.

Firstly, I must thank Norbert, for giving me the chance to work as a scientist and pursue my doctorate degree. There were a lot of lessons learned on how to conduct research and publish scientific papers, but you also inspired me for being a responsible, honest and essentially good person. I would like to thank Claude and Bernhard for all the guidance during these years. Thank you Claude for the scientific discussions and for indicating the best direction several times. Bernhard, you always had a piece of advice at hand and made complicated situations a lot easier.

Many thanks to all the colleagues at the MVM institute, specially to the AME group. Bo and Johanna, thank you for making the beginning of my PhD journey a bit easier with all the tips while we shared the office. Lilie, thanks for unravelling the administration bureaucracy. Karim, thank you for the scientific discussions as well as the fun talks! Thank you Katrin, you helped me relive my PC more than once! Annika, you made my moving to a new appartment very efficient. Karsten, thank you for always being so eager to help, irrespective of technical or non-technical issues. Max, thank you for all the German lessons. Keeevin, thank you for always being there, no matter what! To all my colleagues, I sincerely appreciate the work collaboration, constructive suggestions and fun moments during these years.

Sonja, Alisa and Xenia, I am immensely grateful for our work collaboration and for you patiently guiding me through the biological world at IFG. Thank you Prof. Ute Schepers for kindly providing the resources and expertise so that my bioprinting experiments could happen.

To all my students, who were a big part of my motivation to work, I am extremely grateful! I could learn so much from you and hopefully also teach one thing or two. Tiago, Julian, Teresia, Vanessa, Annabell, Kubilay, Ke and Marc, you are the best.

I want to give my deepest appreciation to my parents, Lurdes and Luiz. I received nothing but unconditional love and support during my whole life regardless the adventure I chose, either in Brazil or in Germany. Your encouragement and kindness certainly paved the way for my achievements. Mãe e pai, obrigada por tudo! Amo vocês!

After more than 10 years together, a huge thanks to my husband (and colleague) Felipe, who was the first to encourage me to face this PhD trajectory and had to deal with all its consequences. Thank you for making my days happier just by being there. You are my home! Jaqueline, the best mother-in-law, thank you for always rooting and praying for me!

Dani, Paulo and Teresia, you are the best friends I could never imagine I would find in Germany. Thank you for being there for me, you make a huge difference. I am also grateful to all my friends who, even living far away, still manage to be part of my life and keep me going.

Preface

This publication based dissertation consists of four peer-reviewed scientific journal articles. These include the main results of my experimental work, done at the Karlsruhe Institute of Technology (KIT), Institute for Mechanical Process Engineering and Mechanics, Applied Mechanics Group, from April 2018 until June 2023.
This thesis includes an abstract, a general introduction and the following adapted publications:

1. B. Maciel, C. Oelschlaeger, N. Willenbacher. Chain flexibility and dynamics of alginate solutions in different solvents. *Colloid and Polymer Science* (2020) 298, 791–801.

2. B. R. Maciel, K. Baki, C. Oelschlaeger, N. Willenbacher. The Influence of Rheological and Wetting Properties of Hydrogel-based Bio-Inks on Extrusion-based Bioprinting. *Chemie Ingenieur Technik* (2022) 94(3), 1–10

3. B. R. Maciel, K. Wang, M. Müller, C. Oelschlaeger, N. Willenbacher. Targeted Micro-Phase Separation – a Generic Design Concept to Control the Elasticity of Extrudable Hydrogels. *Materials & Design* (2023) 227, 111803

4. B. R. Maciel, A. Grimm, C. Oelschlaeger, U. Schepers, N. Willenbacher. Targeted micro-heterogeneity in bioinks allow for 3D printing of complex constructs with improved resolution and cell viability. *Biofabrication* (2023) 15, 045013

The thesis concludes with a summary and an outlook, as well as a joint bibliography. The bibliography includes all references of all publications. Hereby the publications are slightly changed in respect of text and citation format. Furthermore, some diagrams and images are modified in size and color, taking into account the format of this dissertation.

Abstract

In this thesis, polymeric as well as particulate hydrogels were thoroughly characterized and optimized to be used as bioinks in extrusion-based 3D bioprinting. The design concept developed here allowed for excellent spatial resolution and high cell viability. 3D bioprinting is an evolving versatile technique for biomedical applications. In this technique, bioinks are deposited to form three-dimensional constructs of specific geometry. Bioinks comprise living cells embedded in a biocompatible carrying material, normally a hydrogel. These are formed from particulate or, most frequently, crosslinked polymeric networks. In order to better understand the hydrogel mechanical properties, detailed investigation of the precursor polymer solution was conducted in this study. Biopolymers such as alginate, gelatin, chitosan, collagen are commonly used as bioinks due to biocompatibility, capability of gelation and formation of high swollen hydrogels as well as high availability. Here, alginate solutions of concentrations relevant to bioprinting were investigated. Mechanical rheometry, specifically rotational rheometry, squeeze flow, and capillary rheometry, and two microrheology methods, namely multiple-particle tracking (MPT) and diffusing wave spectroscopy (DWS) have been used to get new insight into structural and dynamical properties of alginate dissolved in solvents widely used for bioprinting, namely deionized water, phosphate-buffered saline (PBS), and, for the first time, Dulbecco Modified Eagle Medium (DMEM) cell media. Results demonstrated that alginate rheological properties depend on the solvent quality at concentrations higher than 1 wt.%. In aqueous salt-free and PBS solutions, experimental scaling exponents for the concentration dependence of the specific viscosity η_{sp} and the plateau modulus G_0 agree well with theoretical predictions for neutral polymers in a good solvent. For alginate dissolved in DMEM, all exponents agree with predictions for polymers in theta solvents. Chain persistence length l_p values, as determined here directly from high frequency rheometry for the first time, are independent of alginate concentration and temperature. These findings suggest no change in the conformation of alginate chains with temperature. Additionally, the results reported in this thesis are important as previous findings suggest that polymer chain flexibility might affect cell adhesion.

The study of structural and dynamic properties of alginate in different solvents commonly used for bioprinting is relevant for better understanding polymer conformation and flexibility at relevant concentration values. Nonetheless, during 3D printing, specially extrusion-based bioprinting (EBB), bioinks are usually pre-crosslinked or undergo gelation and exhibit a gel-like state during printing. EBB is the most commonly used technique for 3D bioprinting due to ease of use, low cost and larger material availability. Pneumatic or mechanical forces are used for the extrusion, and the bioink should form uniform filaments in order to be printable. Hydrogels are typically prone to wall slip under flow. So far, most 3D bioprinting investigations regarding hydrogel extrusion do not mention wall slip or tacitly assume no-slip condition. Therefore, little is known about how slip behavior influences printing quality on EBB and whether the material of the nozzle used is relevant. The wall slip and flow behavior of alginate as well as gelatin based hydrogels with respect to the impact of these rheological and wetting properties on extrusion-based bioprinting (EBB) was investigated in this thesis. Capillary rheometry and printing tests were employed to evaluate slip at high stresses relevant for EBB. Rotational rheometry performed at low shear stresses revealed that slip at low stresses is more pronounced on polypropylene (PP) and polytetrafluoroethylene (PTFE) plates than on stainless steel plates for all samples. Moreover, results show that alginate hydrogels present much higher slip velocity and lower slip stress than gelatin gels, presenting much stronger slip behavior. This result is presumably due to the formation of a highly heterogeneous microstructure for alginate gels and has an unfavorable impact on the printing quality with the production of large fluctuations in line width and higher line spread ratio. The EBB experiments performed here confirmed that a higher yield stress of the bioink requires a higher extrusion pressure but improves the shape fidelity of multilayered 3D constructs, while increasing gel elasticity enhanced layer stacking quality.

The pronounced heterogeneity presumably attributed to the alginate sample could explain the strong wall slip and the poor printing quality observed in our study. Due to a potential impact of micro-heterogeneity on macro-rheological properties and extrusion quality, microstructural heterogeneities of four different hydrogel systems were extensively investigated here. There is currently a need of more complex and

heterogeneous engineered hydrogel composites in order to mimic the native human tissue microenvironment. However, there is a lack of understanding about micro-heterogeneity formation and its spatial distribution. Controlling the hydrogels mechanical properties and understanding their complex microstructures is critical for gel applications, e.g., in life sciences ranging from controlling the texture of food gels to 3D bioprinting and tissue engineering. In this thesis we present a generic design concept for tuning the elasticity of polymer and particulate extrudable hydrogels at a given total polymer or particle concentration. Targeted micro-phase separation generates heterogeneities on the length scale 1-100μm, corresponding to gel elasticity variation of more than two orders of magnitude. Four different strategies for inducing micro-phase separation in hydrogels are presented in our study: Micro-mechanical and structural heterogeneity was enhanced in alginate hydrogels by accelerating crosslinking kinetics; the addition of PVA prevented alginate crosslinking and produced softer, more homogeneous hydrogels, while introducing PVA into gelatin gels resulted in more heterogeneous materials with higher elasticity; Higher ionic strength in Laponite-based hydrogels induced nanoparticle aggregation, producing materials of higher elasticity; Addition of alginate to Laponite gels prevented cluster formation due to nanoparticle-polysaccharide interactions, resulting in more homogeneous, softer composite materials. Here, high degree of homogeneity and uniformity in the microstructure were only observed for precursor polymer solutions or gels comprised of only one component and for nanoclay dispersions in the absence of salt. On the other hand, crosslinked polymeric hydrogels where a second polymer or a crosslinker were added showed heterogeneous microstructure for all systems investigated in this work. By abandoning the often tacitly assumed uniformity of the gel on the microscale, we gain additional degrees of freedom to achieve high gel strength and improved extrudability without increasing polymer or particle concentration or adding chemical crosslinkers.

The concept of introducing heterogeneities via micro-phase separation was further employed in this thesis in hydrogels used as bioinks in order to investigate its effect not only in elasticity enhancement but also in other rheological properties as well as in bioprinting. Ideal bioinks have complex micro-environment that mimic human

tissue, allow high printing quality and provide high cell viability after printing. We developed two strategies for enhancing gelatin-based bioinks heterogeneity in the length scale 1-100μm and thereby improve printing quality and cell viability. When poly(vinyl alcohol) is added to homogeneous gelatin gels, pore-shaped viscous inclusions are formed due to micro-phase separation. This phenomenon leads to pronounced slip behavior, as revealed in this study by rotational rheometry, and superior printing quality of complex 3D constructs as well as high human hepatocarcinoma (HepG2) and normal human dermal fibroblasts (NHDF) cell viability due to reduced shear damage during extrusion. Similar printability and cell viability results are obtained here with gelatin/nanoclay composites. The formation of polymer/nanoclay clusters increases the gel brittle performance, facilitating extrusion and therefore enhancing printing quality as well as cell viability. A thorough spatial and micro-mechanical heterogeneity characterization of the hydrogels in the hydrated state was conducted in this thesis via micro-rheology technique Multiple Particle Tracking. We found that size and fraction of micro-heterogeneities in the bioink dictate uniform filament printing and have to be limited according to the printed feature size. Finally, we conclude that targeted introduction of micro-heterogeneities in bioinks through micro-phase separation proved to be an effective technique for high resolution 3D printing of complex constructs with high cell viability.

Zusammenfassung

In dieser Arbeit wurden sowohl polymere als auch partikuläre Hydrogele gründlich charakterisiert und für den Einsatz als Biotinten im extrusionsbasierten 3D-Biodruck optimiert. Das hier entwickelte Designkonzept ermöglicht eine hervorragende räumliche Auflösung und eine hohe Zellviabilität. 3D-Biodruck ist eine sich entwickelnde, vielseitige Technik für biomedizinische Anwendungen. Bei dieser Technik werden Biotinten aufgebracht, um dreidimensionale Konstrukte mit spezifischer Geometrie zu bilden. Biotinten bestehen aus lebenden Zellen, die in ein biokompatibles Trägermaterial, normalerweise ein Hydrogel, eingebettet sind. Diese werden meist aus vernetzten polymeren oder aus partikulären Netzwerken gebildet. Um die mechanischen Eigenschaften von Hydrogelen besser zu verstehen, wurde in dieser Arbeit eine detaillierte Untersuchung der unvernetzten Polymerlösung durchgeführt. Biopolymere wie Alginat, Gelatine, Chitosan und Kollagen werden aufgrund ihrer Biokompatibilität, ihrer Fähigkeit zur Gelierung und Bildung stark gequollener Hydrogele sowie ihrer hohen Verfügbarkeit häufig als Biotinten verwendet. Hier wurden Alginatlösungen in für das Bioprinting relevanten Konzentrationen untersucht. Mechanische Rheometrie, insbesondere Rotationsrheometrie, Squeeze-Flow und Kapillarrheometrie, sowie zwei mikrorheologische Methoden, nämlich Multiple-Particle-Tracking (MPT) und Diffusing-Wave-Spektroskopie (DWS) wurden eingesetzt, um neue Einblicke in die strukturellen und dynamischen Eigenschaften von Alginat zu gewinnen, das in den für das Bioprinting weit verbreiteten Lösungsmitteln, nämlich deionisiertem Wasser, phosphate-buffered saline (PBS) und erstmals auch in Dulbecco Modified Eagle Medium (DMEM) Zellmedien, gelöst ist. Die Ergebnisse zeigen, dass die rheologischen Eigenschaften von Alginat bei Konzentrationen von mehr als 1 Gew.-% von der Qualität des Lösungsmittels abhängen. In wässrigen salzfreien Lösungen und PBS-Lösungen stimmen die experimentellen Skalierungsexponenten für die Konzentrationsabhängigkeit der spezifischen Viskosität η_{sp} und des Plateaumoduls G_0 gut mit den theoretischen Vorhersagen für neutrale Polymere in einem guten Lösungsmittel überein. Für in DMEM gelöstes Alginat stimmen alle Exponenten mit den Vorhersagen für Polymere in Theta-Lösungsmitteln

überein. Die Werte der Persistenzlänge einer Polymerkette l_p, die hier zum ersten Mal direkt aus der Hochfrequenzrheometrie bestimmt wurden, sind unabhängig von der Alginatkonzentration und der Temperatur. Diese Ergebnisse deuten darauf hin, dass sich die Konformation der Alginatketten mit der Temperatur nicht ändert. Darüber hinaus sind die in dieser Arbeit berichteten Ergebnisse wichtig, da frühere Erkenntnisse darauf hindeuten, dass die Flexibilität der Polymerketten die Zelladhäsion beeinflussen könnte.

Die Untersuchung der strukturellen und dynamischen Eigenschaften von Alginat in verschiedenen Lösungsmitteln, die üblicherweise für das Bioprinting verwendet werden, ist wichtig für ein besseres Verständnis der Polymerkonformation und -flexibilität bei relevanten Konzentrationswerten. Beim 3D-Druck, insbesondere beim extrusionsbasierten Bioprinting (EBB), sind die Biotinten jedoch in der Regel vorvernetzt oder geliert und weisen während des Drucks einen gelartigen Zustand auf. EBB ist aufgrund der einfachen Anwendung, der geringen Kosten und der guten Materialverfügbarkeit die am häufigsten verwendete Technik für das 3D-Bioprinting.

Für die Extrusion werden pneumatische oder mechanische Kräfte eingesetzt, und die Biotinte sollte gleichmäßige Filamente bei Austritt aus der Düse bilden, um druckbar zu sein. Hydrogele neigen typischerweise zum Wandgleiten beim Fließen. Bislang wird in den meisten Untersuchungen zum 3D-Bioprinting im Zusammenhang mit der Extrusion von Hydrogelen das Wandgleiten nicht erwähnt oder es wird stillschweigend angenommen, dass kein Gleiten auftritt. Daher ist wenig darüber bekannt, wie das Wandgleiten die Druckqualität bei EBB beeinflusst und ob das Material der verwendeten Düse eine Rolle spielt. In dieser Arbeit wurde das Wandgleiten- und Fließverhalten von Hydrogelen auf Alginat- und Gelatinebasis im Hinblick auf die Auswirkungen dieser rheologischen und benetzenden Eigenschaften auf das extrusionsbasierte Bioprinting (EBB) untersucht. Kapillarrheometrie und Drucktests wurden eingesetzt, um das Wandgleiten bei hohen, für EBB relevanten Spannungen zu bewerten. Die bei niedrigen Schubspannungen durchgeführte Rotationsrheometrie ergab, dass das Gleiten bei niedrigen Spannungen bei allen Proben auf Polypropylen- (PP) und Polytetrafluorethylen- (PTFE) Platten stärker ausgeprägt ist als auf Edelstahlplatten. Darüber hinaus zeigen die Ergebnisse, dass Alginat-Hydrogele eine

viel höhere Gleitgeschwindigkeit und eine geringere Gleitspannung aufweisen als Gelatinegele und daher ein viel stärkeres Gleitverhalten zeigen. Dieses Ergebnis ist vermutlich auf die Bildung einer sehr heterogenen Mikrostruktur bei Alginatgelen zurückzuführen und wirkt sich ungünstig auf die Druckqualität aus, da es zu großen Schwankungen in der Linienbreite und einer höheren Spreiteung der Linien kommt. Die hier durchgeführten EBB-Experimente bestätigten, dass eine höhere Fließgrenze der Biotinte einen höheren Extrusionsdruck erfordert, aber die Formtreue von mehrschichtigen 3D-Konstrukten verbessert, während eine höhere Gel-Elastizität die Qualität der Schichtstapelung verbessert.

Die ausgeprägte Heterogenität, die vermutlich auf die Alginatprobe zurückzuführen ist, könnte das starke Wandgleiten und die schlechte Druckqualität erklären, die in unserer Studie beobachtet wurde. Aufgrund der möglichen Auswirkungen der Mikroheterogenität auf die makrorheologischen Eigenschaften und die Extrusionsqualität wurden hier mikrostrukturelle Heterogenitäten von vier verschiedenen Hydrogelsystemen eingehend untersucht. Gegenwärtig besteht ein Bedarf an komplexeren und heterogeneren Hydrogel-Kompositwerkstoffen, um die natürliche Mikroumgebung des menschlichen Gewebes zu imitieren. Es mangelt jedoch an Kenntnissen über die Bildung von Mikroheterogenität und deren räumliche Verteilung. Die Kontrolle der mechanischen Eigenschaften von Hydrogelen und das Verständnis ihrer komplexen Mikrostrukturen ist entscheidend für Gelanwendungen, z. B. in den Biowissenschaften, von der Kontrolle der Konsistenz von Lebensmittelgelen bis hin zum 3D-Bioprinting und Tissue Engineering. In dieser Arbeit stellen wir ein generisches Designkonzept vor, um die Elastizität von polymeren und partikulären extrudierbaren Hydrogelen bei einer gegebenen Gesamtpolymer- oder Partikelkonzentration einzustellen. Gezielte Mikrophasentrennung erzeugt Heterogenitäten auf der Längenskala von 1-100µm, was einer Variation der Gel-Elastizität von mehr als zwei Größenordnungen entspricht. In unserer Studie werden vier verschiedene Strategien zur Herbeiführung der Mikrophasentrennung in Hydrogelen vorgestellt: Die mikromechanische und strukturelle Heterogenität wurde in Alginathydrogelen durch Beschleunigung der Vernetzungskinetik verbessert; Die Zugabe von PVA verhinderte die Alginatvernetzung und führte zu weicheren,

homogeneren Hydrogelen, während die Zugabe von PVA in Gelatinegelen zu heterogeneren Materialien mit höherer Elastizität führte; Eine höhere Ionenstärke in Hydrogelen auf Laponit-Basis führte zur Aggregation von Nanopartikeln und damit zu Materialien mit höherer Elastizität; Die Zugabe von Alginat zu Laponit-Gelen verhinderte die Bildung von Clustern aufgrund der Wechselwirkungen zwischen Nanopartikeln und Polysacchariden, was zu homogeneren, weicheren Verbundmaterialien führte. Ein hohes Maß an Homogenität und Gleichmäßigkeit der Mikrostruktur wurde nur bei Polymerlösungen oder Gelen, die nur aus einer Komponente bestehen, und bei Laponit-Dispersionen in Abwesenheit von Salz beobachtet. Dagegen zeigten vernetzte polymere Hydrogele, denen ein zweites Polymer oder ein Vernetzer zugesetzt wurde, bei allen in dieser Arbeit untersuchten Systemen eine heterogene Struktur. Indem die oft stillschweigend angenommene Gleichförmigkeit des Gels auf der Mikroskala aufgeben wurde, zusätzliche Freiheitsgrade wurden erworben, um eine hohe Gelfestigkeit und verbesserte Extrudierbarkeit zu erreichen, ohne die Polymer- oder Partikelkonzentration zu erhöhen oder chemische Vernetzer hinzuzufügen.

Das Konzept der Einführung von Heterogenitäten durch Mikrophasentrennung wurde in dieser Arbeit in Hydrogelen, die als Biotinten verwendet werden, weiter angewandt, um ihre Auswirkungen nicht nur auf die Verbesserung der Elastizität, sondern auch auf andere rheologische Eigenschaften sowie auf das Bioprinting zu untersuchen. Ideale Biotinten haben eine komplexe Mikroumgebung, die menschliches Gewebe nachahmt, eine hohe Druckqualität ermöglicht und eine hohe Lebensfähigkeit der Zellen nach dem Druck gewährleistet. Zwei Strategien wurden entwickelt, um die Heterogenität von Biotinten auf Gelatinebasis auf einer Längenskala von 1-100 µm zu verbessern und dadurch die Druckqualität und die Lebensfähigkeit der Zellen zu erhöhen. Wenn Poly(vinylalkohol) zu homogenen Gelatinegelen hinzugefügt wird, bilden sich aufgrund von Mikrophasentrennung porenförmige viskose Einschlüsse. Dieses Phänomen führt zu einem ausgeprägten Gleitverhalten, wie in dieser Studie mit Hilfe der Rotationsrheometrie festgestellt wurde, und zu einer besseren Druckqualität komplexer 3D-Konstrukte sowie zu einer hohen Lebensfähigkeit von Zellen des menschlichen Hepatokarzinoms (HepG2) und Normal-Human-Dermal-Fibroblasts

(NHDF) aufgrund einer geringeren Scherschädigung während der Extrusion. Ähnliche Ergebnisse in Bezug auf Druckbarkeit und Zellviabilität werden hier mit Gelatine/Nanoclay-Verbundstoffen erzielt. Die Bildung von Polymer/Nanoclay-Clustern erhöht die Sprödigkeit des Gels, erleichtert die Extrusion und verbessert somit die Druckqualität und die Lebensfähigkeit der Zellen. In dieser Arbeit wurde die gründliche räumliche und mikromechanische Heterogenität der Hydrogele im hydratisierten Zustand mittels mikrorheologischer Technik (Multiple Particle Tracking) charakterisiert. Es wurde festgestellt, dass Größe und Anteil der Mikroheterogenitäten in der Biotinte begrenzt werden und kleiner als die gedruckte Featuregröße sein müssen, weil sie den gleichmäßigen Filamentdruck diktieren. Abschließend kommen wir zu dem Schluss, dass sich die gezielte Einführung von Mikroheterogenitäten in Biotinten durch Mikrophasentrennung als effektive Technik für den hochauflösenden 3D-Druck komplexer Konstrukte mit hoher Zellviabilität erwiesen hat.

Contents

1 Introduction

3D bioprinting is a promising technique for biomedical applications. Its global market is estimated to grow from USD 1.7 billion in 2021 to USD 5.3 billion in 2030 [1]. The direct depositing of living cells embedded in biocompatible materials, the so called bioink, allows uniform cell distribution in 3D constructs for a variety of applications, such as tissue engineering, drug delivery and in vitro experiments [2]. 3D bioprinting offers high reproducibility, precise cell deposition with spatial freedom and the ability to produce heterogeneous constructs that mimic the natural tissue complexity [3]. 3D scaffolds have the capacity of better mimicking natural tissue in comparison to 2D methods of cell culture [4]. In 3D conformation, cell-cell and cell-environment interactions are similar to the ones *in vivo.* Moreover, due to spheroids formation, the cells morphology is conserved and its metabolism and topology are comparable to the native tissue.

Tissue engineering has the potential to revolutionize regenerative medicine and wound healing in the years to come. Although 3D bioprinting still faces many translational challenges [5], development of several 3D bioprinted scaffolds for tissue engineering were reported in the literature [6,7]. Bone marrow derived stem cells as well as osteoblasts were printed in order to promote bone tissue differentiation and (re)generation [8]. Chondrocytes were printed in an effort to repair cartilage damage [9], a recurrent problem that causes joint pain in patients. Different types of endothelial and fibroblasts cells were printed in hollow cylinder-like shapes to promote formation of microvascular grafts [10] to be employed in coronary diseases. Keratinocytes and fibroblasts were printed in order to promote formation of different skin layers for repairing wounds [11]. In addition, printing of various types of cancer cells allows the formation of 3D tumor models for investigation of cancer progression, creating a reproducible prediction of clinical response [12].

In general, living cells are incorporated in adequate biocompatible carrier materials, forming the bioink. The bioink is placed in a 3D printer and constructs are

formed in a layer-by-layer manner. Once the printing is complete, the 3D scaffold is then placed in cell growth media for the cells to grow and the tissue to mature at adequate temperature and oxygen level (Fig.1.1).

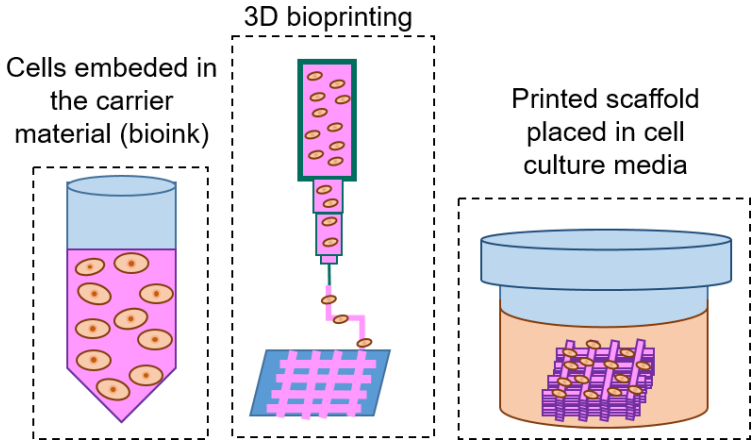

Figure 1.1 – General steps for 3D bioprinting process

This thesis will focus on the characterization and design of bioinks, i.e. biocompatible hydrogels used to embed the cells during 3D printing, aiming an improved printing quality and cell viability. Regardless of cell line and tissue type, printing quality and cell viability after printing are important parameters that must be optimized [13]. Printing quality depends mainly on the rheological properties of the bioink used, namely viscosity, yield stress and elasticity [14]. However, the achievable printing resolution depends on the 3D printing method as well.

Cell viability, a crucial parameter in 3D bioprinting, indicates the cell survival rate after printing. Generally, cell viability depends on the amount of shear stress perceived by the cells while printing and is related to the bioink rheological properties as well as to the printing method and parameters used [15]. In order to increase viability while optimizing printability, bioink mechanical properties and printing parameters have to be tuned accordingly to reduce shear as well as extensional forces experienced by the cells [16]. In our study, we employed an extrusion based bioprinter and systematically characterized various types of bioinks, from polymer precursor solution to hydrogels, using macro- and micro-rheology techniques in order to optimize both printing quality and cell viability.

1.1 Dynamics of polymer solutions in different solvents

Polymer solutions are common constituents of bioinks due to the potential of network formation as well as biocompatibility. Understanding the rheological properties of such solutions as well as how polymer chains behave in different solvents is of great interest for several applications where these materials are processed, including bioprinting.

Dynamics of polymer solutions are dependent of the concentration regime [17,18]. In the dilute regime, described by the Zimm model [19], the molecules behave as single chains and the polymer conformation depends on the solvent quality. In a θ solvent, the chain occupies the same volume as in a melt (zero net excluded volume), while in a poor solvent the polymer chain volume shrinks and in a good solvent it expands [20]. By increasing the polymer concentration, individual chains start to overlap each other at the overlap concentration c^* [21]. At this concentration, the total polymer volume fraction is equal the volume fraction of the polymer inside its pervaded volume. At polymer concentrations higher than c^*, the semi-dilute regime takes place, as described by the Rouse model [22]. The polymer chains behave similarly to the dilute regime for length scales smaller than the correlation length ξ. For length scales larger than ξ, electrostatic and excluded volume interactions are screened, as the polymer chain exhibits random walk statistics [20].

When the polymer concentration is higher than c_e (entanglement concentration), polymer chains begin to exhibit entanglements that restrain each other's motion. The dynamics of entangled solutions are predicted by the tube model and characterized by the tube diameter, which is longer than the correlation length [23]. The reptation model can be used to determine the longest relaxation time of the polymer chain.

Polymer elasticity is a result of entropy changes that take place when stretching and deforming the polymer molecules [24]. The scaling predictions of viscosity, elastic plateau modulus and relaxation time as a function of concentration c for polymers in the semi-dilute unentangled and entangled regimes can be found in Table 1.1:

Table 1.1 - Scaling predictions for polymer solutions in the semi-dilute unentangled and entangled regimes (adapted from Publication I).

	Unentangled semi-dilute			**Entangled semi-dilute**		
	η_{sp}	G_0	T_R	η_{sp}	G_0	T_R
Polyelectrolytes in **salt free**	$c^{0.50}$	c^{1}	$c^{-0.5}$	$c^{1.5}$	$c^{1.5}$	c^{0}
Polyelectrolytes in **high salt**	$c^{1.25}$	c^{1}	$c^{0.25}$	$c^{3.75}$	$c^{2.25}$	$c^{1.5}$
Neutral polymers in **good solvent**	$c^{1.3}$	c^{1}	$c^{0.31}$	$c^{3.75}$	$c^{2.3}$	$c^{1.6}$
Neutral polymers in **theta solvent**	c^{2}	------	c^{1}	$c^{4.7}$	$c^{2.3}$	$c^{2.3}$

1.2 3D Bioprinting techniques

The mainly employed techniques in 3D bioprinting are extrusion based, stereolithography, inkjet, laser-assisted and micro-valve based bioprinting [25] [26]. Stereolithography and laser-assisted offer the highest printing resolution among all techniques, but also the longest fabrication time as well as the largest limitation of bioink materials available. Inkjet and micro-valve techniques allow for deposition of low viscous bioinks, which is beneficial to cell viability. On the other hand, these methods are limited to low cell density and suffer from nozzle clogging. In this thesis, extrusion based-bioprinting (EBB) technique [27] was employed. It is the most affordable and easy to use method. In addition, EBB allows for a wide array of bioink materials to be printed, from very low to extremely high viscosity (30-10^7 mPa.s) [28]. However, it is the technique that presents the highest shear stresses experienced by the cells, leading to lower cell viability in comparison to other methods. In EBB, bioinks are placed in a syringe or cartridge and extruded through a nozzle of diameter ranging from 0.1 to 1 mm, directly on a substrate. Therefore, EBB requires bioinks that form uniform and stable filaments upon extrusion. The simplest EBB technique is the pneumatic-based one, where air pressure is the driving force for the extrusion process (Fig.1.2A). The piston-driven technique consists of a motor moving a piston (Fig.1.2B), while the screw-

driven technique includes a feed screw directly conveying the bioink (Fig.1.2C). The use of a mechanical system allows for improved flow rate control in comparison to the pneumatic method. However, the screw-driven technique might impose higher shear stresses on the bioink during extrusion, thus affecting cell viability.

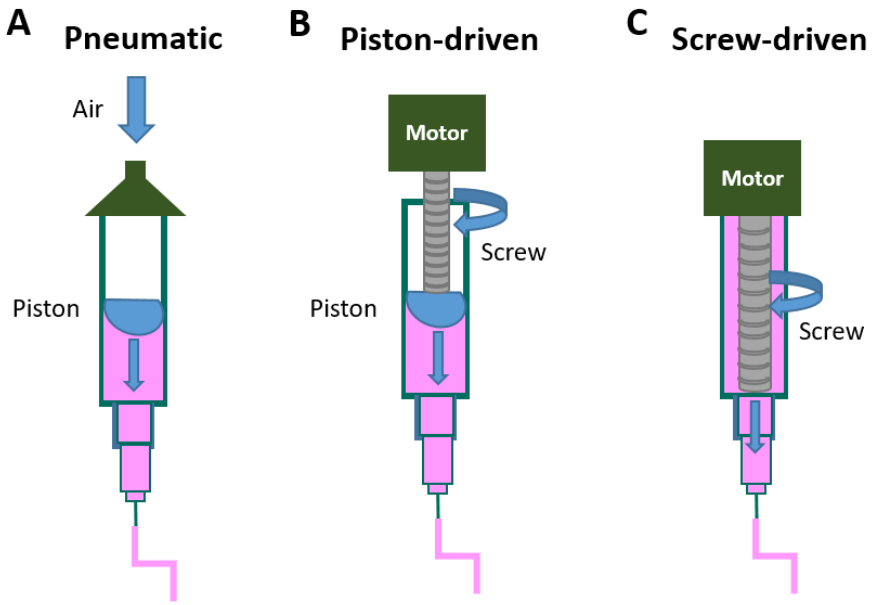

Figure 1.2 – Extrusion-based bioprinting (EBB) techniques. Based on [27].

Viscosity, shear thinning as well as yield stress and wall slip are relevant rheological parameters to be considered for successful EBB as they can all affect the printing and cell encapsulation efficiency. Viscosity of the hydrogels should be sufficiently high to retain the shape of the printed object during and after the printing process and to ensure a good cell support and miscibility [29]. However, too high viscosity might lead to high shear forces perceived by the cells and lower cell viability. Another key parameter of bioinks is the shear thinning behavior, i.e. the decrease of viscosity with increasing shear rate [30]. This phenomenon enables printing at feasible pressure and flow rates. The flow behavior of a bioink during EBB is dictated by these rheological properties, as the velocity field within a pipe depends on the type of fluid. For shear thinning fluids, the flow profile is flatter in the middle and drops faster towards the wall, i.e. the center region of low shear rate is broader but the shear rate in the narrower outer region is higher (Fig.1.3) [31]. This type of fluid behavior is commonly described by a power law model:

$$\eta = m\dot{\gamma}^{n-1} \quad (1.1)$$

Where η is the viscosity, $\dot{\gamma}$ is the shear rate, m and n are model parameters.

In addition to viscosity and shear thinning behavior, the yield stress, i.e. the amount of stress necessary for the onset of shear deformation, plays also a crucial role in both cell miscibility and filament formation and deposition. Recent work demonstrated that materials with higher yield strength exhibit better shape fidelity [32]. However, too high yield stresses hinder cell incorporation, i.e. cells have to be added prior to structure formation or cross-linking. It should be noted that the shear stress $\tau(r)$ within a straight capillary decreases from its maximum value at the wall (r=R) to zero at the center of the nozzle (r=0) (Fig.1.3). Therefore, only the fraction of ink in the outer region where the shear stress τ exceeds the yield stress τ_y is deformed and the inner region undergoes a plug flow [33] .

Due do the high amount of water in its composition, hydrogels employed as bioinks can exhibit wall slip behavior when extruded. Wall slip happens when a thin layer of low viscosity and also depleted from cells forms close to the cartridge or needle wall. Most of the shear deformation takes place in that thin layer while the remaining volume remains undeformed (plug flow) and moves with a slip velocity *Vs* (Fig.1.3) [33]. Wall slip enables high printing speed at low imposed pressure and may also be beneficial for cell viability. The occurrence of wall slip on one hand depends on the roughness of the nozzle wall, but also on the interfacial energy between the nozzle surface and the liquid phase of the bioink.

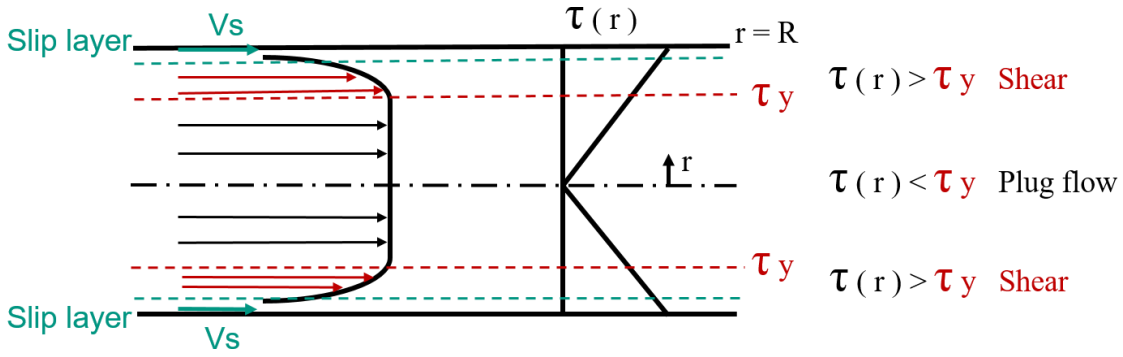

Figure 1.3 – Expected plug flow profile during EBB for a shear-thinning fluid with a yield stress τ_y as well as in the presence of wall slip with slip velocity V_S. Based on [33].

In addition to the previously mentioned rheological properties, the bioink microstructure and heterogeneity in micro-length scale also dictate the filament formation and uniformity as well as cell viability. The insufficient control over heterogeneity formation in bioinks results in limited production of biomimetic materials [34]. The employment of multicomponent bioinks in EBB allows for new possibilities in mirroring heterogeneous and complex native tissues, favoring cell growth [35]. Too heterogeneous bioinks, however, might impact the bulk mechanical properties as well as impair printing quality and printed filament uniformity. The multicomponent bioink rheological as well as microstructural parameters have to be carefully adjusted in order to protect cells during EBB and promote cell growth but also to optimize printing quality and filament deposition.

1.3 Hydrogels as bioinks for EBB

Bioinks are generally constituted of living cells embedded in a biocompatible material. Hydrogels are the most used materials as cell carriers in bioinks, as they confer a highly hydrated 3D structural environment to living cells [36]. Hydrogels consisting of biopolymers, such as alginate, gelatin, chitosan and collagen, are often employed, due to their high biocompatibility and mostly large availability. Biopolymers, however, generally show limitations in their mechanical properties as well as fluctuations in composition and product quality. Biocompatible synthetic polymers, namely poly(vinyl alcohol) (PVA), polyethylene glycol (PEG) and polycaprolactone are often incorporated into biopolymer hydrogels due to their adjustable chemical structures and physical characteristics in order to improve desired mechanical properties [37], such as increase in elasticity, viscosity or printing quality.

Typical ways of increasing hydrogel elasticity consist of simply increasing polymer or crosslinker concentration, modifications on the polymer chain, addition of particles or fibers for reinforcement, or solvent exchange [38,39]. In addition, targeted material combinations and composites help improve mechanical properties, printability as well as biocompatibility regarding specific cell lines [40]. Particulate hydrogels as well as

composite materials of biopolymers reinforced with nanoparticles or nanofibers have recently arisen as bioink alternatives. Nanoparticles, such as nanoclay, bioactive glasses and hydroxyapatite, as well as nanofibers, namely carbon and cellulose nanofibers, are known to favorably contribute to the bioink mechanical properties and may even enhance biocompatibility as well as cell adhesion [41,42].

Another strategy for improving hydrogels mechanical properties is the double network (DN) technique, where two (or more) polymers with different crosslinking mechanisms are mixed and the single networks are either physically or chemically crosslinked [43,44]. The crosslinking process is a critical step, as it must confer mechanical stability to the hydrogel but should not be toxic to the living cells.

Hydrogel mechanical properties should be optimized for maximizing mechanical stability during printing but also for minimizing shear forces perceived by living cells. Techniques that employ liquid or very soft bioinks in EBB have been developed in order to increase cell viability during extrusion. 3D printing of complex structures has been described using the FRESH technology with soft collagen bio-inks and support materials that can be melted away [45], or using the NICE technique to print a soft hydrogel consisting of GelMA, kappa-carrageena and nanosilicates by increasing the printing temperature to 37°C [46]. However, there is a lack of bioink materials that allow room temperature printing of self-standing structures with high cell viability.

1.4 Mechanical properties of bioinks for EBB

Before the printing process, hydrogels used as bioinks should not exhibit too high elasticity or yield stress otherwise it might hinder uniform incorporation of cells [32]. Besides, high shear forces at the step when cells are embedded might already negatively influence cell viability. During printing, bioinks in EBB must show mechanical stability for consistent filament formation and a pre-crosslinking step of the polymer solution or composite is often required when no support material is used. After bioprinting, a final crosslinking step is applied for long term as well as thermal stability of the bioink during cell culture and tissue maturation, which normally occurs for several days at 37°C.

This work focused on the study of the rheological properties of precursor polymer solutions as well as of pre-crosslinked hydrogels used as bioinks. These bioinks are investigated at the same state as they are used in the printing process when bioink filaments are formed. Bioink properties at this stage of the bioprinting process along with the 3D printer setup control the achievable resolution and printing quality of the 3D construct [47]. Besides, this is the step that dictates cell viability, as the cells experience the highest shear forces in the process [48,49].

Bulk rheological parameters of bioinks, such as shear elasticity G_0, Young's modulus E, yield stress τ_y and viscosity η, have been widely studied [16], but there seems to be no universal agreement on the fine tuning of these properties for an optimum printing quality [50]. Results seem to be material dependent and do not offer a general design strategy. Similar lack of understanding is also observed for hydrogel wall slip behavior. Hydrogels are non-Newtonian materials that are prone to slip due to the high amount of water [51,52]. In the literature, the non-slip condition is tacitly assumed during hydrogel flow and very little was found about wall slip effects on bioprinting.

Another aspect not yet fully understood is the heterogeneity formation on the micrometer length scale and its effect on macro mechanical properties of hydrogels. Bioinks should exhibit a heterogeneous microstructure in order to mimic the complexity of human tissue for cells to interact and proliferate [53,54]. Accordingly, biomechanical gradients are normally not achievable with single component or single phase materials [55]. Hence, multi-material approach is employed for bioink preparation. Besides, micro-fluidic techniques and lithography were employed for introducing heterogeneity in injectable hydrogels with certain precision [56]. However, controlling and characterizing macro-porosity and micro-heterogeneities formation in hydrogels in water-swollen state remains very challenging [57]. Visualization and characterization of micro-heterogeneity in hydrated hydrogels could give a new insight into the effects of bioink microstructure on the bulk mechanical properties as well as on printing quality and cell viability.

1.4.1 Macro-rheology of bioinks

Bulk rheological investigations of bioinks include mainly elasticity, yield stress and viscosity measurements. The evaluation of bioink elasticity is generally conducted in terms of shear oscillatory measurements to obtain the storage and loss moduli *G'*, *G''* at small deformations corresponding to the linear response regime [58]. In stress-controlled oscillatory shear experiments, a sinusoidal stress $\tau(t)$ is applied $\tau(t) = \tau_A . \sin \omega t$, where τ_A is the amplitude and ω the angular frequency. The linear response of the strain is then given by $\gamma(t) = \gamma_A . \sin(\omega t + \delta)$, where δ is the phase shift angle. The shear stress $\tau(t)$ is proportional to the strain amplitude γ_A and can be represented as $\tau(t) = \gamma_A . (G'(\omega)(\sin(\omega t) + G''(\omega)(\cos(\omega t))$. $G'(\omega)$ is defined as the storage modulus and $G''(\omega)$ as the loss modulus. The storage and loss modulus are the real and imaginary parts of the complex modulus $G^*(\omega) = G'(\omega) + iG''(\omega)$. The storage modulus represents the storage of elastic energy, while the loss modulus indicates the viscous dissipation during a stress or strain cycle. For polymer networks, the storage modulus *G'* is almost independent of frequency. Therefore, the bulk shear modulus G_0 is deduced from the value of *G'* at a constant angular frequency (Fig. 1.4A). The plateau modulus G_0 is a key structural parameter for entangled solutions and/or chemically crosslinked networks, it is related to the physical and/or chemical crosslinking density and hence the mesh size of the network [59].

Uniaxial compression is another commonly used method to evaluate bioink elasticity, where the Young's modulus *E* is obtained as the slope of the linear region of a stress-strain curve [60] (Fig.1.4B). In general, elasticity has been used to describe bioinks stability, extrudability, printing quality as well as mechanical resemblance to native human tissue. Moreover, it is assumed that the elasticity of hydrogels used as bioinks should be in the same order of magnitude of natural soft and connective tissue for implants to provide good utility [61].

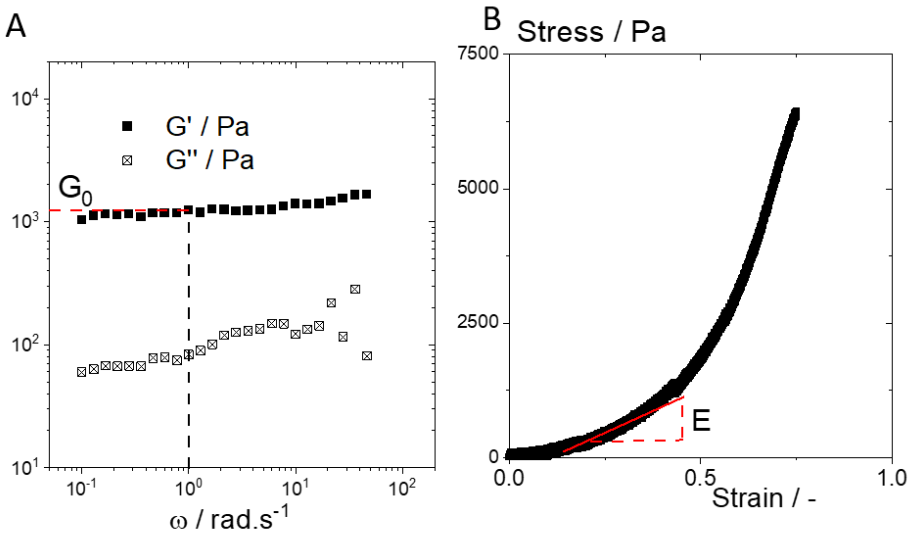

Figure 1.4 – Elasticity measurements in terms of oscillatory shear, with $G'(\omega)$, $G''(\omega)$ and G_0 (A) and uniaxial compression, with E modulus determination (B).

Hydrogel yield stress τ_y has also been used to describe bioink stability, shape fidelity or printing quality [62]. The yield stress of a material is usually assessed via a creep test with a rotational rheometer, where shear stress is stepwise increased and the deformation is measured [63]. The yield stress may then be determined using the two-tangent method where deformation is plotted as a function of shear stress using logarithmic scales. Then, one tangent is fitted to the data in the low shear, elastic response regime while the second tangent is fitted to the plastic deformation region. The value extracted from the crossover of the two tangents is the yield stress (Fig.1.5A), i.e the necessary stress applied for the material to plastically deform and flow. Another way of determining yield stress is performing oscillatory shear experiments. The oscillation amplitude is increased at constant frequency value and the yield stress is given by the stress amplitude at which the crossover of the shear moduli *G''* and *G'* [64] occurs, as illustrated in Fig.1.5B.

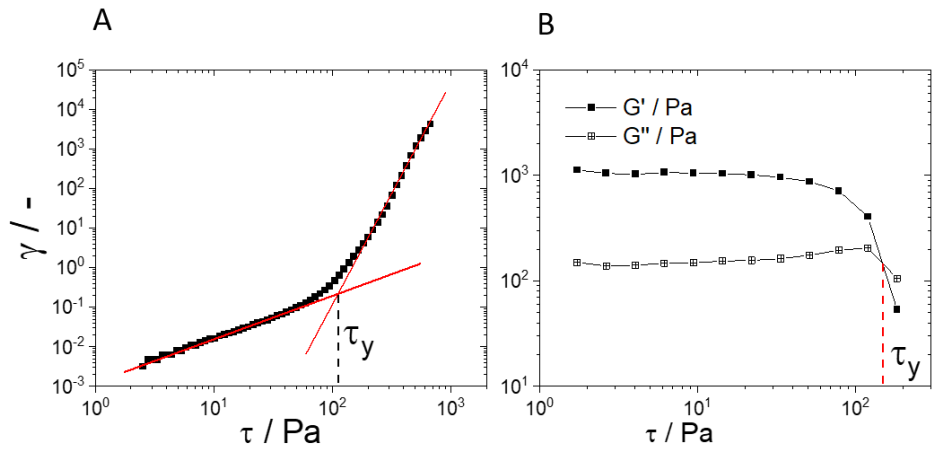

Figure 1.5 – Yield stress τ_y determination in terms of creep tests (A) and oscillatory shear experiments (B).

Viscosity is the most often used rheological parameter to characterize bioinks and evaluate printability [65]. Viscosity η is defined as the proportionality between the local shear stress τ_{yx} and the change of velocity with position in a fluid $\frac{dv_x}{dy}$ [31]:

$$\tau_{yx} = \eta \frac{dv_x}{dy} \quad (1.2)$$

In the case of the commonly used parallel-plate geometry, the shear viscosity η is defined as $\eta(\dot{\gamma}) = \tau(\dot{\gamma})/\dot{\gamma}$, where the shear stress τ is the stress applied in the parallel direction of the flow and the shear rate $\dot{\gamma}$ is the speed of the moving plate divided by the gap distance between plates [59]. The viscosity of most diluted polymer solutions remains constant irrespective of shear rate, they are called Newtonian fluids. Most complex fluids, however, do not exhibit Newtonian behavior and the viscosity can vary with shear rate and/or time. Capillary rheometry is often used for determining viscosity values at shear rates higher than 10^3 s^{-1}, normally not accessible with a rotational rheometer.

In order to be easily extrudable, bioinks have to present a shear thinning behavior, that is viscosity should decrease upon increasing shear rates [66], as exemplarily demonstrated in Fig.1.6A. However, when characterizing hydrogels which exhibit yield

stress, the flow behavior should only be considered for shear rates or stresses above the yield stress. This phenomenon is mostly neglected in the literature, where unphysical viscosity values at shear stresses lower than the yield stress are often used for material characterization. Similar to elasticity, viscosity can impact extrusion and final cell viability. Highly viscous as well as highly elastic materials might transfer higher stresses to living cells, reducing cell viability considerably [67].

When characterizing rheological properties of hydrogels using rotational rheometers, wall slip can be a source of measurement errors (Fig.1.6B). Rough plates are therefore often used to mitigate this effect [68]. On the other hand, wall slip behavior of hydrogels can impact flow properties, affect printability and even be indicative of pronounced micro-heterogeneity. Wall slip can be observed in steady shear experiments supported by video imaging of the sample rim. The apparent slip stress indicates the onset of slip and the apparent slip velocity, calculated as the velocity of the plate rim, displays the magnitude of slip in the material [51,52] .

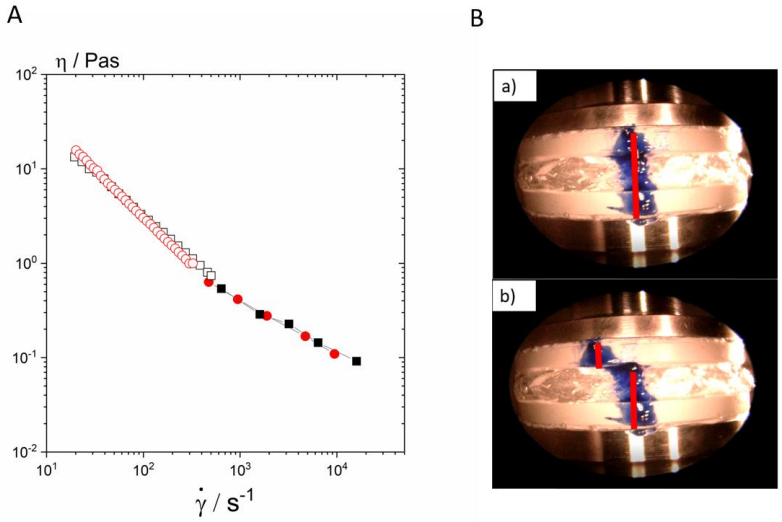

Figure 1.6 – Viscosity measurement of shear-thinning fluids (A) and visualization of wall slip during measurement with a parallel-plate rheometer (B). Adapted from Publication II.

1.4.2 Micro-mechanical characterization of hydrogels

Hydrogels micro-mechanical properties and microstructure in water swollen state have been characterized in terms of micro-indentation [69,70], atomic force microscopy (AFM) [71,72], multiple particle tracking (MPT) [73,74] and diffuse wave spectroscopy (DWS) [75]. Hydrogel mechanical strength and heterogeneity characterization is important not only in the field of biomedicine, but also for the perception of texture, sensory and organoleptic properties in food and cosmetics gels [76,77], as well as mechanical robustness of filtration and adsorbent gels [78].

Regarding biomedical applications, the local visco-elastic properties and microstructure of the material can dictate drug as well as living cells adhesion, cell interaction, growth, differentiation and nutrient diffusion [72,79]. Specifically in the tissue engineering field, there is a need of more complex and heterogeneous engineered hydrogel composites in order to mimic the native human tissue microenvironment [80]. A targeted combination of materials is decisive to develop a heterogeneous construct with both biomechanical and biochemical gradients [55]. In general, little is known about the correlation between micro-heterogeneities and macro-elasticity of hydrogels. More specifically, there is a lack of studies showing how these micro-heterogeneities might influence filament formation uniformity and printing quality in EBB. Moreover, micro-heterogeneities characteristics, such as size and type, may have an impact on cell viability.

1.4.3 Multiple Particle Tracking (MPT) for micro-mechanical characterization of hydrogels and bioinks

MPT has been used for characterizing local mechanical properties and heterogeneity of polymer solutions, food and hydrogels used for cell culture. For homogeneous materials, MPT reveals the same viscosity of elastic modulus as bulk rheological measurements. However, it gives details on local elasticity and viscosity of heterogeneous materials that cannot be detected with bulk rheology. Moreover, the spatial visualization of heterogeneities in the hydrogel high swollen state can be

extremely useful in several hydrogel applications. MPT can provide information on hydrogel microstructure and micromechanical properties in the hydrated state without any sample modification.

Limitations on the use of currently available imaging methods for hydrogel microstructure characterization have been reported in the literature [57,81,82]. Sample processing such as drying and coating with conductive material which is normally required for scanning electron microscopy (SEM), or the need of a contrast agent as in microcomputed tomography (μCT), leads to difficulties in resolution, limited depth penetration, artefact production or even destruction of the original 3D hydrogel microstructure, generating inaccurate results. MPT technique has been proved to be an effective tool for microstructural and local flow behavior characterization, especially in cases where other microscopy methods fail. Turbid, highly concentrated colloidal dispersions [83] as well as fiber suspensions with similar refractive index of the continuous phases, such as lyophilized collagen [81] are examples of materials with complex microstructural properties that were successfully characterized using rheological data as well as Voronoi plots or overlay of images obtained from MPT experiments.

Additionally, this technique has been employed for viscoelastic and microstructural characterization of food emulsions and gels [84]. More specifically, studies on viscoelastic properties of low concentrated gelatin [85] and alginate [86] solutions as well as sol-gel transition dynamics of gelatin [87] applying MPT have been reported. Most of these studies, however, focus on the flow behavior of liquid state polymer solutions and very soft materials or on the kinetics of the liquid-solid transition during hydrogel formation [88,89]. To our knowledge so far, there is few published data on visualization of micro-heterogeneities in biomaterials or biocompatible hydrogels using MPT [74,81,90].

The underlying idea of MPT is to monitor the Brownian motion of tracer particles embedded in a material of interest and thereby achieve information about the rheological properties of the surrounding fluid. The samples to be investigated are placed between a glass slide and a cover slip, and the fluorescence microscope is focused halfway into the sample. 2D images of the fluorescent particles are recorded using a high speed

camera. Movies constituted from the images sequence are analysed and the mean square displacement of each fluctutating bead is calculated. An overlay of all images recorded can be used to spatially visualize the microstructure of the material [83]. Besides, the Voronoi triangulation can be used to directly visualize viscous and elastic regions, generating a “rheological contrast” map in the sample [91].

The local viscoelastic modulus *G*(ω)* around a sphere as a function of the frequency *ω* can be determined from the generalized Stokes-Einstein equation (GSE) [92]:

$$G^*(\omega) = \frac{k_b T}{\pi a i\omega \left\langle \Delta\tilde{r}^2(i\omega) \right\rangle} = G'(\omega) + iG''(\omega) \quad (1.3)$$

with a being the tracer particle radius, k_B the Boltzmann constant, T the temperature and $\langle \Delta\tilde{r}^2(i\omega) \rangle$ the Mean Square Displacement (MSD) of the tracer particles.

Tracers trapped in an elastic network exhibit a time-independent MSD directly related to the apparent local shear modulus (Eq.1.4) of this region:

$$G_{0,MPT} = \frac{2k_B T}{3\pi a \Delta r^2} \quad (1.4)$$

Tracers freely diffusing in a viscous environment exhibit a linearly increasing MSD and the apparent viscosity η_{MPT} of the surrounding fluid is determined using Eq. 1.5 obtained from the Stokes-Einstein relation, and the relation $\langle \Delta r^2(\tau) \rangle = 4D\tau$, where D is the diffusion coefficient related to the MSD $\langle \Delta r^2(\tau) \rangle$ as a function of the lag time τ [93]:

$$\eta_{MPT} = \frac{k_B T}{6\pi a D} \quad (1.5)$$

The non-Gaussian parameter *α* (Eq. 1.6) describes the deviation of the MSD values from a Gaussian distribution expected for an ergodic homogeneous, uniform sample [94]:

$$\alpha = \frac{\left\langle x^4(\tau) \right\rangle}{3\left\langle x^2(\tau) \right\rangle^2} - 1 \quad (1.6)$$

in which x^4 and x^2 are the fourth and second moments of the probability distribution of particle displacement. This displacement distribution is also known as the van Hove correlation function.

1.4.4 DWS for characterization of polymer structural and dynamical properties

DWS has been successfully employed for the investigation of viscoelastic and structural properties of semiflexible polymers and self-assembled structures. Local structural variations or high frequency relaxation processes were studied in polymeric thickeners [91], starch solutions [95], clay suspensions [96], intermediate filament networks [97] and semi-flexible micellar solutions [98,99].

DWS is an extension of the traditional dynamic light scattering technique in which multiple light scattering is analyzed. This passive micro-rheology method allows for monitoring the displacement of micron sized colloidal particles without external driving force. Viscoelastic properties of complex transparent materials can be measured in frequency range varying from 10^{-1} to 10^{6} rad.s^{-1}. Thermal motion of the colloidal particles lead to intensity fluctuations of the scattered light. These fluctuations are recorded by an appropriate detector at a fixed scattering angle and the intensity autocorrelation function (ICF) is generated. The ICF decay gives the ensemble average of the particles MSD $\langle \Delta r^2(t) \rangle$ [100,101].

Both viscoelastic moduli $G'(\omega)$ and $G''(\omega)$ are obtained based on the GSE equation (Eq. 1.3) [92]. It should also be noted that the GSE relation is valid only under the assumption that the material surrounding the sphere can be treated as an isotropic and homogeneous continuum, i.e. that the particle size is larger than the structural length scales of the probed material.

For polymer solutions, both the plateau modulus G_0 and the terminal relaxation time T_R are often only obtained at high frequencies not achievable with a rotational rheometer. DWS high frequency rheological measurements allow for obtaining the plateau modulus G_0 and the terminal relaxation time T_R, which is given as the inverse of the angular frequency corresponding to the first crossover of G' and G''. Moreover, it is possible to determine the mesh size ξ of a polymer network according to the classical

theory of rubber elasticity assuming thermal equilibrium, namely $G_0 = k_B T/\xi^3$, where $k_B\ is$ the Boltzmann constant and *T* the temperature. Another structural parameter that can be determined using DWS high frequency rheological measurements is the persistence length l_p of viscoelastic fluids. In this regime, the stress relaxation is controlled by the internal dynamics of individual molecules and the moduli G' and G'' show characteristic scaling behavior $G' \sim G'' \sim \omega^{\delta}$.

First, the Rouse-Zimm modes dominate and δ = 5/9 (Fig. 1.7A). At even higher frequencies internal bending modes of single Kuhn segments determine G' and G'', hence these dynamic parameters are related to the bending modulus β often expressed in terms of the persistence length through $\beta = k_B T l_p$. In this frequency range, the scaling exponent δ =3/4 is found (Fig.1.7) [102,103]. The transition between these scaling regimes is marked by the inverse of the shortest Rouse relaxation time $\omega_0 = T_0^{-1}$ (Fig. 1.7B) which is directly related to the persistence length:

$$\omega_0 = \frac{k_B T}{8\eta_s {l_p}^3} \qquad (1.7)$$

where η_s is the solvent viscosity. The persistence length l_p is indicative of the polymer chain flexibility and might affect living cells adhesion to the polymer network [104].

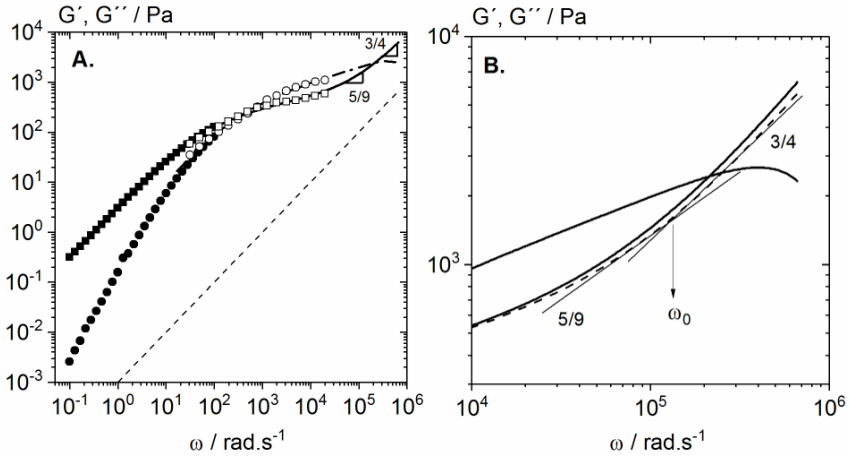

Figure 1.7 – Dynamic shear moduli of an alginate solution obtained from rotational rheometry, oscillatory squeeze flow and DWS measurements overall covering a large

frequency range (A) High frequency region and determination of ω_0 (B). Figure obtained from Publication I.

1.5 Evaluating 3D bioprinting success

Significant advances in 3D bioprinting were reported for cartilage, bone and skin tissues [105]. However, these reports consist of quite simple tissue structures without major vascularization or complexity in terms of cell types, geometry and chemical as well as mechanical degrees. 3D bioprinting is nowadays restricted to small-scale constructs in the pre-clinical and translational stages. Current research evaluates 3D bioprinting success *in vitro* in terms of printing quality of the scaffold as well as cell viability, differentiation, formation of cell signaling molecules or secretion of proteins [106]. Printability and shape fidelity of bioinks are essential for the long-term cell culture and hence for supporting cell proliferation and differentiation [107]. This thesis focuses on assessing the printing quality of the bioinks developed here as well as the cell viability after printing for selected bioinks in order to evaluate the 3D bioprinting success.

1.5.1 Printing quality in EBB

Uniform filament formation, high resolution and shape fidelity are important parameters that contribute to an improved printing quality of 3D scaffolds. In EBB, bioinks should exhibit mechanical properties that allow filament formation, as droplets do not confer high printing quality in this bioprinting method. Printing quality can be evaluated by different methods, but this evaluation is almost always based on the quality of the filament formation. One of the most used techniques is calculating the spread ratio, which is the printed line width divided by the nozzle outlet diameter (Fig. 1.8A). The spread ratio measured along a printed line gives information on the filament uniformity. The lower the spread ratio in a fairly uniform filament, the higher the shape fidelity of the bioink. By printing adjacent lines, filament fusion due to surface tension or lack of elasticity can be assessed (Fig.1.8B). Another commonly used parameter is the so called printability index P_r [47,49], as given by Eq. 1.8:

$$P_r = \frac{\pi}{4}.\frac{1}{C} = \frac{Pe^2}{16A} \quad (1.8)$$

Where *C* is the circularity of an enclosed area, *Pe* is the perimeter and *A* is the area. A high geometry accuracy when printing grid structures would give $P_r = 1$, meaning that the pores exhibit a square geometry. A round geometry would give $P_r < 1$ while an irregular shape would give $P_r > 1$ (Fig. 1.8C). The higher the square fidelity, higher the overall shape fidelity of the bioink.

The methods described above are normally applied for 2D or planar structures. When more layers are printed and a 3D object is formed, the total height can be measured and compared to the construct designed height (Fig.1.8D). This would give a measure of the scaffold shape fidelity in 3D and also of the overall stability of the layer stacking [47]. For specific applications where overhangs are printed, the bioink resistance to gravity can be evaluated by printing a filament on top of a pillar array (Fig.1.8E). Filament collapse or sagging can be measured and the bioink evaluated for potential overhang printing. It is also important to differentiate between planar objects and 3D printed scaffolds. A bioink might offer good results of spread ratio and P_r in 2D but not necessarily be stable when 3D constructs are printed because of poor layer stacking properties or filament collapse.

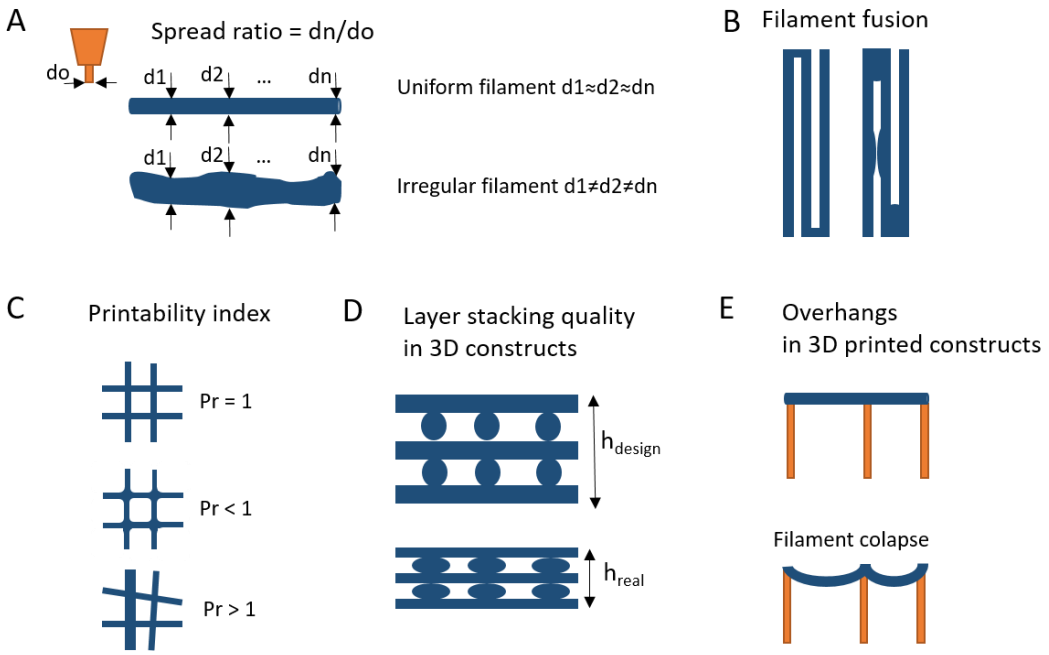

Figure 1.8 – Printing quality evaluation methods for EBB. Based on [47].

1.5.2 Cell viability in EBB

Cell viability is a crucial outcome in 3D bioprinting. Several studies have investigated the impact of shear stress generated during bioprinting on cell viability [48][108][15]. Shear stress strongly affects cell adhesion, proliferation, phenotype and metabolism, and all these parameters may have an effect on the overall cell viability. Material properties that are critical to cell viability when printing include bioink mechanical characteristics such as viscosity, elasticity and yield stress [49,62], but also bioink chemical aspects, namely additives, crosslinking and overall toxicity [108,109]. The search for biocompatible extrudable materials has forced the modification of already established biocompatible hydrogels in terms of polymer chain modification, chemical reactions or addition of chemical crosslinkers as well as addition of particles and fibers for reinforcement. This leads not only to changes in the material rheological properties but also to variation in the toxicity perceived by different cell lines. Generally, high viscous/elastic hydrogels are able to transfer higher shear stresses to cells, impairing cell viability [49]. Similarly, hydrogels with high yield stress hinder cell embedding and might damage the cells [62]. However, distinct cell lines might respond differently to the

shear stresses applied as well as to the toxicity levels of the bioink and the absolute cell viability may vary depending on the cell robustness and specificities [49].

Not only the material plays an important role on cell viability but also the extrusion parameters and process settings [15]. The shape of micro-nozzles used in EBB can dictate the shear force magnitude that the living cells perceive, as tapered nozzles are less harmful than cylindrical needles [110,111]. In tapered nozzles, high shear stress values are concentrated only at the tip of the nozzle, while in cylindrical needles shear stresses are high along the whole needle. This means that cells are more susceptible to suffer from shear forces when passing through the needle. Besides, nozzles with smaller outlet diameters might require a higher extrusion force. More specifically, in the pneumatic EBB method high extrusion pressure leads to high wall shear stress values, which can be harmful to living cells. The wall shear stress τ_w in a cylinder is given by the Equation 1.9 [112]:

$$\tau_w = \frac{\Delta P.r}{2l} \quad (1.9)$$

where ΔP corresponds to the pressure difference, r is the needle diameter and l the needle length.

Optimizing extrusion pressure as well as micro-nozzle size and shape resulting in high cell viability and yet maintaining high printing quality is still a challenge to be overcome [13].

Motivation and Outline

This thesis covers the detailed but broad macro- and micro-rheological characterization of a polymer solution as well as of various hydrogel systems used as bioinks for extrusion-based 3D bioprinting. In general, we present a new strategy for tailoring mechanical properties of extrudable gels and bioinks by inducing micro-heterogeneities in several hydrogel systems already stablished as biocompatible cell carrier materials, namely pure alginate, gelatin and Laponite hydrogels, mixtures of PVA with alginate and with gelatin as well as mixtures of Laponite with alginate and with gelatin. Extrudability and printing quality of these systems as well as cell viability for the gelatin-based gels were evaluated taking into consideration the impact of the micro-mechanical properties.

The first scientific article included in this thesis presents the thorough macro- and micro-rheological characterization of alginate solutions. Alginate is one of the most frequent used biopolymers in bioprinting and tissue engineering, due to its availability, ease of gelation and biocompatibility. Alginate was dissolved in different solvents and in concentrations widely used for bioprinting and was characterized using micro-rheology techniques such as DWS and MPT in order to get new insight into structural and dynamical properties. Parameters such as chain flexibility, relaxation time, specific viscosity and plateau modulus and its dependence on temperature as well as on solvent quality were obtained for the first time. PBS and DMEM are solvents widely used in bioinks, but there is a lack of detailed studies on how these solvents affect alginate structural and dynamical properties. Therefore, the investigation of the polymer precursor solution is of high interest.

When used as bioinks for EBB, polymer solutions are crosslinked or undergo gelation in order to form a network and become hydrogels. Only in this gel-like state bioinks are able to form filaments upon extrusion. EBB is the most used method for 3D printing bioinks, due to its low cost, ease of operation and material availability. Extrudability of bioinks strongly depends on rheological properties, such as elasticity, shear thinning behavior and yield stress. However, little attention is given to bioinks wall slip behavior. Due to the high amount of water, hydrogels are prone to slip under flow.

In the second scientific publication included in this thesis, we investigated the phenomenon of wall slip on EBB employing alginate and gelatin-based hydrogels and using different nozzle materials commonly used in bioprinting, namely stainless steel, PP and PTFE. The wettability and rheological properties under controlled shear stress conditions relevant for EBB were evaluated for different alginate and gelatin based hydrogels. Improved gel printability, such as high layer stacking quality and shape fidelity, were found in gels with not only high shear elasticity but also high yield stress. We hoped to clarify the role of wall slip on the printing quality of hydrogels commonly used as bioinks in EBB. In this study, pronounced wall slip and non-uniform printed filaments suggested a stronger hydrogel heterogeneity. This phenomenon was further investigated in the next scientific publications.

Bulk rheological properties are assumed to dictate extrudability of hydrogels, whereas the impact of local micro-mechanical properties or micro-heterogeneities on the printing quality is mostly overlooked. Moreover, there is a lack of control over heterogeneity formation at the micrometer scale. Among the mechanical properties, elasticity is one of the most important rheological parameters for an extrudable hydrogel. Generally, higher elasticity allows for lower line spread ratio and improved layer stacking when printing 3D constructs. Techniques for increasing elasticity of hydrogels range from simply increasing polymer or crosslinker concentration to chemical modifications in the polymer chain as well as addition of reinforcements or additional chemical crosslinkers. In the third scientific article presented in this thesis we introduce a new strategy for tailoring hydrogels elasticity. Targeted micro-phase separation generates heterogeneities on a mesoscopic length scale (1-100µm) corresponding to gel elasticity variation of more than two orders of magnitude. Four different strategies for inducing micro-phase separation in polymeric as well as particulate hydrogels are presented and the corresponding extrusion quality is evaluated. By abandoning the often tacitly assumed uniformity of the hydrogel on the microscale, we gain additional degrees of freedom to achieve high gel strength and improved extrudability without increasing polymer or particle concentration or adding chemical crosslinkers. MPT micro-rheology was applied to investigate microstructural changes and characterize microheterogeneity of the hydrogels in the hydrated state. We hoped to establish correlations between the

micro-heterogeneities' characteristics, such as size and degree of phase separation, and the macro elasticity of hydrogels. The effects of heterogeneity and elasticity increase on the extrusion quality were investigated as well.

Among the various hydrogel systems studied here, mixtures of gelatin and PVA as well as gelatin and Laponite stand out due to the excellent printing quality of complex 3D constructs at room temperature without any supporting material. On the fourth scientific publication included in this thesis, excellent printing quality was achieved by the targeted introduction of liquid (in gelatin/PVA gels) and solid (in gelatin/Laponite gels) micro-heterogeneities. The impact of these different types of heterogeneities generated by micro-phase separation on the bulk rheological properties were carefully studied. Effects were observed not only on the hydrogel elasticity, but also on the viscosity, wall slip and breakage stress of the bioinks. The size and fraction of these heterogeneous inclusions were carefully characterized and the optimum conditions for obtaining excellent printing quality were evaluated. Moreover, the facilitated extrusion due to the micro-heterogeneities has shown to be beneficial for cells during printing, mitigating shear forces experienced by them and improving cell viability. HepG2 and NHDF cell lines were used in the experiments and cell viability was assessed post printing. HepG2 liver carcinoma cells are one of the most used immortalized cell types for in vitro testing in biomedical applications while NHDF is a primary cell line culture commonly employed for soft tissue engineering.

Publication I

2 Chain flexibility and dynamics of alginate solutions in different solvents

Full title: Chain flexibility and dynamics of alginate solutions in different solvents

Authors: Bruna Maciel, Claude Oelschlaeger and Norbert Willenbacher

Status: published

Maciel, B., Oelschlaeger, C. & Willenbacher, N. Chain flexibility and dynamics of alginate solutions in different solvents. *Colloid Polym Sci* **298**, 791–801 (2020). https://doi.org/10.1007/s00396-020-04612-9

Abstract

Mechanical rheometry, specifically rotational rheometry, squeeze flow and capillary rheometry, and two microrheology methods, namely Multiple Particle Tracking (MPT) and Diffusing Wave Spectroscopy (DWS) have been used to get new insight into structural and dynamical properties of alginate dissolved in solvents widely used for bioprinting, namely deionized water, phosphate buffered saline (PBS) and Dulbecco Modified Eagle Medium (DMEM) cell media. Results demonstrate that alginate rheological properties depend on the solvent quality at concentrations higher than 1wt.%. In this high concentration regime, in aqueous salt free and PBS solutions, experimental scaling exponents for the concentration dependence of the specific viscosity η_{sp} and the plateau modulus G_0 agree well with theoretical predictions for neutral polymers in good solvent whereas for the terminal relaxation time T_R the exponent is slightly higher than theoretically predicted, presumably due to the formation of aggregates. For alginate dissolved in DMEM, all exponents for η_{sp}, G_0 and T_R agree with predictions for polymers in theta solvents, which might be related to the formation of polyelectrolyte complex as a result of interactions between alginate and amino acids.

Chain persistence length l_p values, as determined directly from high frequency rheometry for the first time, are independent of alginate concentration and temperature. Lower absolute l_p values were found for DMEM solutions compared to the other solvents. Moreover, scaling exponents for η_{sp}, G_0 and T_R do not change with temperature, within 20 and 60°C. These findings suggest no change in the conformation of alginate chains with temperature.

2.1 Introduction

Alginate is an anionic polysaccharide derived from marine brown algae [113]. The linear copolymer backbone is composed of consecutive blocks of α-L-guluronic (G-blocks) and β-D-mannuronic (M-blocks) linked by a β-(1-4) glycosidic bond. It is a biomaterial that has found numerous applications in biomedical science and engineering due to its favorable properties, including biocompatibility and ease of gelation [113]. Recently, alginate has become particularly attractive as it has been used as scaffold for cell cultivation because it can form robust cell-compatible hydrogels in physiological conditions [114]. In particular, it has been employed as bioink in a relatively novel tissue engineering (TE) strategy, namely the 3D bioprinting technology [115]. Bioink is one of the most important components in bioprinting and the role of the alginate is to provide a matrix scaffold to cell growth allowing reliable fabrication of 3D constructs after printing. Both mechanical and chemical properties of alginate in hydrogel form, obtained in presence of divalent cations e.g., Ca^{2+}, have been widely studied and well established [116]. However, for better printing efficiency, properties of the hydrogel must be improved, therefore it is very important to accurately characterize and understand properties of alginate in solution especially under physiological and cell media conditions. In the literature, however, rheological and structural properties of alginate have been mainly reported in aqueous salt free solutions and in presence of NaCl [117–121]. In most of these reports, the scaling behavior of the specific viscosity η_{sp} dependence on alginate concentration in both the dilute and semi-dilute regime has been assessed and results were compared to theoretical predictions for polyelectrolyte in salt-free solutions and in the high salt limit [122]. Few of them [116] also investigated

the concentration dependence of the terminal relaxation time T_R, which was determined to fit the shear viscosity flow curve using a generalized non-Newtonian Cross model [123,124]. To our knowledge, the concentration dependence of another key structural parameter, namely the plateau modulus G_0 has never been investigated. This quantity is directly related to the mesh-size λ of the system with $\lambda = (k_B T/G_0)^{1/3}$ [125]. Additionally, in many studies, the persistence length l_p of alginate in dilute solutions has been determined based on intrinsic viscosity [126,127], size-exclusion chromatography [128,129] measurements and electron microscopy images [130,131]. In all these studies, $l_p$values between 12-16 nm were found independent of the technique used and ionic strength. These above experimental data are in qualitative good agreement with calculated values (~12 nm) obtained from modeling simulations [132,133]. In contrast, fluorescence correlation spectroscopy (FCS) [134] performed in the very dilute regime and small angle X-ray scattering (SAXS) measurements [135] covering a more concentrated regime, up to 30 g/l, provide smaller l_p values around 5 nm and 1-2.5 nm, respectively. An accurate characterization of the persistence length of alginate chains is of high importance, as the chain flexibility is supposed to affect cell adhesion as suggested by Lee et al. [104].

In this study, we use classical rotational rheology, squeeze flow and capillary rheometry as well as two microrheology methods, namely Multiple Particle Tracking (MPT) and Diffusing Wave Spectroscopy (DWS) to get new insight into structural and dynamical properties of bioinks composed of pure alginate dissolved in water, phosphate buffered saline (PBS) and Dulbecco Modified Eagle Medium (DMEM) cell media. DWS allows for characterizing viscoelastic properties of alginate solutions in a very broad frequency range, from 1 to 10^6 rad.s^{-1}, and for the first time we determine the persistence length l_p of latter solutions in the semi-dilute entangled regime directly from high frequency rheological measurements. Variation of l_p with alginate concentration, type of solvent and temperature is investigated too.

Another structural parameter investigated here is the plateau modulus G_0. This parameter is determined at intermediate frequencies by measuring it directly and we investigate its dependence on alginate concentration in a large concentration range for the three different solvents. We also determine the specific viscosity η_{sp} as well as the

relaxation time T_R and establish for each parameter the scaling laws characterizing its concentration dependence. These results are compared with scaling predictions for polyelectrolytes in the salt free and in the high salt limit and for neutral polymers in good and theta solvents [17,20,136]. Variations of those parameters with temperature are also investigated. Table 2.1 below gives scaling predictions in semi-dilute unentangled and entangled solutions.

Table 2.1 - Scaling predictions for polyelectrolytes in salt free and in the high salt limit, neutral polymers in good and theta solvents for semidilute unentangled and entangled solutions [17,20,122,136].

	Unentangled semidilute			**Entangled semidilute**		
	η_{sp}	G_0	T_R	η_{sp}	G_0	T_R
Polyelectrolytes in **salt free**	$c^{0.50}$	c^{1}	$c^{-0.5}$	$c^{1.5}$	$c^{1.5}$	c^{0}
Polyelectrolytes in **high salt**	$c^{1.25}$	c^{1}	$c^{0.25}$	$c^{3.75}$	$c^{2.25}$	$c^{1.5}$
Neutral polymers in **good solvent**	$c^{1.3}$	c^{1}	$c^{0.31}$	$c^{3.75}$	$c^{2.3}$	$c^{1.6}$
Neutral polymers in **theta solvent**	c^{2}	------	c^{1}	$c^{4.7}$	$c^{2.3}$	$c^{2.3}$

2.2 Materials and methods

2.2.1 Sample characteristics

Sodium alginate was purchased as alginic acid sodium salt from brown algae, BioReagent product line, from Sigma-Aldrich Chemie GmBH (Taufkirchen, Germany). The molar mass of each monomer, i.e G- and M-blocks, is 198 g/mol and the charge to charge distance in each group is 0.435 nm and 0.57 nm, respectively [113]. The total molar mass determined from intrinsic viscosity measurements is in the range of 300-500 kg/mol. Phosphate buffer saline (PBS) in tablet form was purchased from Sigma-Aldrich and Dulbecco's Modified Eagle's Medium (DMEM w: 4.5 g/L Glucose, w: L-Glutamine, w: Sodium pyruvate, w/o: Phenol red, w: 3.7 g/L NaHCO3) from PAN Biotech (Aidenbach, Germany). Alginate solutions were prepared stirring the powder with three

different solvents: Mili-Q water, 1xPBS (~0.15 M salt) and DMEM for approximately 1 hour until they appeared limpid and homogeneous, at concentrations that vary from 0.05 wt.% to 7 wt.%. The pH value for alginate in salt free and in PBS solutions was 7.4±0.1, whereas alginate in DMEM solutions presented a slightly higher pH of 8.5±0.2. For the sake of convenience, alginate solutions in milli-Q water will subsequently be referred to as aqueous solutions or salt free solutions.

2.2.2 Rotational rheometry

A rotational rheometer, Rheoscope I from Thermo Haake (Karlsruhe, Germany), equipped with a cone-plate measuring cell (diameter 50 mm, cone angle 1°) was used to perform steady as well as small amplitude oscillatory shear experiments covering the frequency range from 0.1 to 100 rad.s^{-1} at 20°C and 37°C. Strain sweep experiments performed prior to frequency sweeps ensured that the selected strain amplitude was sufficiently small to provide a linear material response at all investigated frequencies.

2.2.3 Oscillatory squeeze flow

Oscillatory squeeze flow experiments were performed at 20°C using a piezo-driven axial vibrator (PAV) customized at the Institute for Dynamic Material Testing (Ulm, Germany). This rheometer characterizes fluid linear viscoelastic properties in a frequency range between 0.1 to almost 10 kHz. Here, gap heights between two stainless steel plates between 18 and 43 µm have been used, corresponding to very small sample volumes, typically ~100 µl. A detailed description of the operating principles and technical details of the instrument can be found in [137].

2.2.4 Capillary rheometry

Steady shear experiments at high shear rates up to 106 s^{-1} were performed at 20°C using a self-assembled capillary rheometer [138]. The samples were forced to flow through capillaries of diameter 0.5 mm but different lengths (10 – 40 mm) with a piston of 15 mm diameter at controlled volume flow rates corresponding to constant shear rate values. The resulting extrusion pressure was recorded using a pressure transducer

(pressure range from 0 up to 200 bars, Industrial Sensors Incorporated, United States of America) and is proportional to the shear viscosity of the fluid [31].

2.2.5 Diffusing wave spectroscopy (DWS)

DWS is an extension of the traditional dynamic light scattering technique in which multiple light scattering is analyzed. This method allows for monitoring the displacement of micron sized colloidal particles with subnanometer precision and on timescales as short as 10 ns, so that it provides access to frequencies well above 104 rad.s^{-1}. Due to the Brownian motion of particles, the detector records intensity fluctuations from which the intensity autocorrelation function (ICF) and then the mean square displacement (MSD) $\langle \Delta r^2(t) \rangle$ can be calculated. Finally, both viscoelastic moduli $G'(\omega)$ and $G''(\omega)$ are obtained based on a generalized Stokes Einstein equation (GSE) [92]. In our experiments, we have added polystyrene particles of diameter 300, 720 or 1400 nm as tracers. The choice of particle size was made to obtain the most accurate ICF in the time range investigated by our DWS setup for each alginate concentration. Additionally, prior to performing DWS measurements, we verified that no particles agglomeration occurred using light microscopy. It should also be noted that the GSE relation is valid only under the assumption that the material surrounding the sphere can be treated as an isotropic and homogeneous continuum, i.e. that the particle size is larger than the structural length scales of the probed material. For all alginate solutions investigated here, we estimated that the plateau modulus G_0 is larger than 10 Pa. From this value, we can directly determine the mesh size ξ of the network according to the classical theory of rubber elasticity assuming thermal equilibrium, namely $G_0 = k_B T/\xi^3$, where k_B *is* the Boltzmann constant and T the temperature. We obtain a maximum mesh size of 75 nm and this value is much smaller than the size of the smallest tracer particles used.

A customized setup based on the DWS ResearchLab device (LS Instruments, Fribourg, Switzerland) was used. Samples were filled in standard glass cuvettes (Hellma) with a path length of 2 mm and a width of 5 mm. The temperature was controlled within ±0.1°C using a temperature control chamber. The measurements were conducted at 20°C and 37°C and for some selected concentrations also at 60°C. A 200 mW single frequency laser (Torus 532, Laser Quantum) operating at a wavelength λ

=532 nm was used to illuminate the sample. We collected the transmitted light using a single-mode optical fiber and single photon counting detector with high quantum efficiency and subsequently analyzed it employing a digital correlator. More details about the DWS device and data processing can be found in Oelschlaeger et al. [139].

From these high frequency rheological measurements, the persistence length of viscoelastic fluids can be determined. In this regime, the stress relaxation is controlled by the internal dynamics of individual molecules and the moduli G' and G'' show characteristic scaling behavior:

$$G' \sim G'' \sim \omega^{\delta} \qquad (2.1)$$

First the Rouse-Zimm modes dominate and $\delta = 5/9$. At even higher frequencies internal bending modes of single Kuhn segments determine G' and G'' hence these dynamic parameters are related to the bending modulus β often expressed in terms of the persistence length through $\beta = k_B T l_p$. In this frequency range, the scaling exponent δ =3/4 is found as predicted by Morse [102] and Gittes & MacKintosh [103]. The transition between these scaling regimes is marked by the inverse of the shortest Rouse relaxation time $\omega_0 = T_0^{-1}$ which is directly related to the persistence length:

$$\omega_0 = \frac{k_B T}{8 \eta_s {l_p}^3} \qquad (2.2)$$

where η_s is the solvent viscosity.

2.2.6 Multiple-particle tracking (MPT)

This technique allows for characterizing local mechanical and structural heterogeneities of complex materials on a micrometer length scale [140,141]. As both methods, DWS and bulk rheology, provide only averaged sample properties, using MPT, we want to verify that alginate solutions are uniform and homogeneous solutions. MPT experiments were performed using an inverted fluorescence microscope (Axio Observer D1, Zeiss), equipped with a Fluar 100x, N.A. 1.3, oil-immersion lens or a C-Apochromat, 40x, N.A. 1.2, water-immersion lens. In this study we have used green fluorescent polystyrene microspheres with 0.2 µm diameter (Bangs Laboratories) as tracer particles. The mixture containing the investigated fluid including the tracers was injected into a

self-build chamber at 20°C, consisting of a coverslip and microscope glass slide with height ~150 µm. Images of these fluorescent beads were recorded onto a computer via a sCMOS camera Zyla X (Andor Technology). Displacements of particle centers were monitored in a 127 × 127 µm field of view, at a rate of 50 frames/s. Movies of the fluctuating microspheres were analysed by a custom MPT routine incorporated into the software Image Processing System (Visiometrics iPS) and a self-written Matlab program [91] based on the widely used Crocker and Grier [142] tracking algorithm. For MPT experiments, a relative experimental error of 5% was estimated.

2.3 Results and discussion

2.3.1 Comparison of mechanical rheometry and DWS measurements

The variation of the dynamic shear moduli G' and G'' as a function of frequency as determined from both mechanical and optical (DWS) rheometry are given in Fig. 2.1a for a 3 wt.% alginate aqueous solution at 20°C. Good agreement is found between mechanical and optical methods. For both techniques, the shapes of the relaxation patterns coincide over the whole frequency range, and also the absolute values agree very well. Similar results were obtained for all systems investigated here irrespective of the type of solvent used. At low frequencies $\omega < 5$ rad.s^{-1}, the terminal flow regime with $G' \sim \omega^2$ and $G'' \sim \omega$ is observed and at intermediate frequencies, both moduli cross each other at ω =330 rad.s^{-1} and a well-developed quasi-plateau in G' (G'increases slightly with ω), which extends at least over one decade in frequency (2x10^3 rad.s^{-1}< ω < 2x10^4 rad.s^{-1}) is found. At high frequencies, $\omega > 5 \times 10^4$ rad.s^{-1}, the viscous response is first dominated by the Rouse-Zimm modes with a scaling exponent $G'' \sim \omega^{5/9}$ and at even higher frequencies, $\omega > 1.5 \times 10^5$ rad.s^{-1}, internal bending modes of single Kuhn segments dominate with $G'' \sim \omega^{3/4}$ as predicted theoretically. However, G' does not scale as $G' \sim \omega^{5/9}$ or $G' \sim \omega^{3/4}$ in the frequency range investigated here, for this parameter the scaling occur at higher frequencies. For the l_p calculation, the solvent contribution was subtracted from the G'' curve as shown in Fig. 2.1b. Using eq. 2.2, we found ω_0 =1.32 x

10^5 rad.s^{-1} and l_p = 15.6 ± 3.1 nm for this system. The characteristic rheological parameters terminal relaxation time T_R and plateau modulus G_0 have been derived directly from the modulus curves. T_R is given by the inverse angular frequency corresponding to the first crossover of G' and G''. The plateau modulus G_0 is defined as the value of the modulus G' at the frequency of $\omega = 10^4$ rad.s^{-1} for all the investigated solutions.

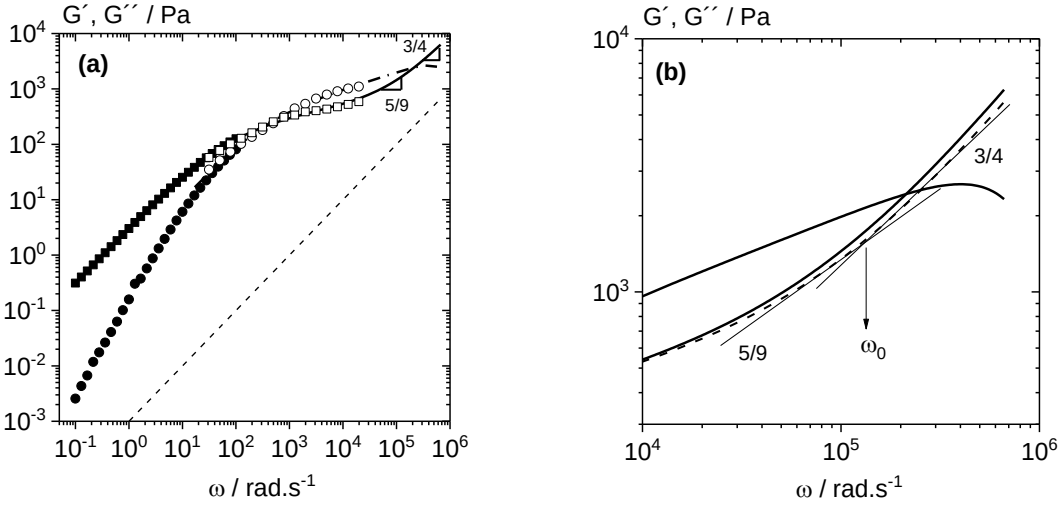

Figure 2.1 **– (a)** Dynamic shear moduli G′ and G″ of a 3 wt.% alginate aqueous solution obtained from DWS (G′ dash-dotted line, and G″ solid line), oscillatory squeeze flow (G′ open circles, G″ open squares), and rotational rheometry (G′ closed circles, G″ closed squares) at T = 20°C. The modulus of water G″ = ωη$_s$ is included for reference (dashed line). (**b)** Enlarge of the high frequency region. Raw DWS data (solid lines), G´´ after subtracting water contribution (dashed line)

2.3.2 Comparison of mechanical rheometry and MPT measurements

Here, we use for the first time the multiple particle tracking (MPT) technique to characterize local viscoelastic properties of alginate solutions. More particularly, MPT is used to obtain information about the heterogeneity of these systems in a range of concentrations relevant for the bioprinting process, from the weakly to the highly entangled regime, i.e. from 1 to 7 wt.%. Fig. 2.2 shows the variation of MSDs as a function of time for PS particles of diameter 0.2 µm dispersed in a slightly entangled 1 wt.% alginate aqueous solution. All MSD traces vary almost linearly with time, indicating

that the motion of the tracer particles is purely diffusive and that the microenvironment surrounding the particles responds like a viscous liquid. From the averaged MSD, we determined the viscosity η_{MPT} using the relation $\langle \Delta r^2(\tau) \rangle = 4D\tau$ where the Stokes-Einstein relation gives $D = \frac{k_B T}{6\pi R \eta_{MPT}}$ with *R* being the tracer particle radius, k_B the Boltzmann constant and *T* the temperature. We found $\eta_{MPT} = 130 \pm 40$ mPa.s and within experimental error this value is in good agreement with the viscosity value $\eta_{Bulk} = 185 \pm 20$ mPa.s obtained from steady shear measurements.

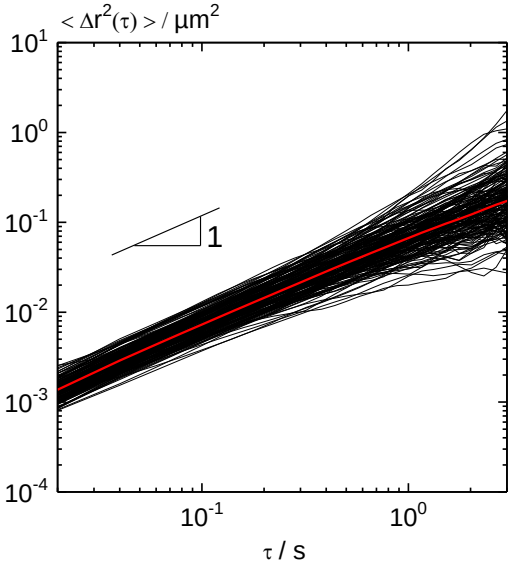

Figure 2.2 - MSDs of individual PS particles of diameter 0.2 μm dispersed in a 1 wt.% alginate aqueous solution. The red curve is the ensemble-average MSD

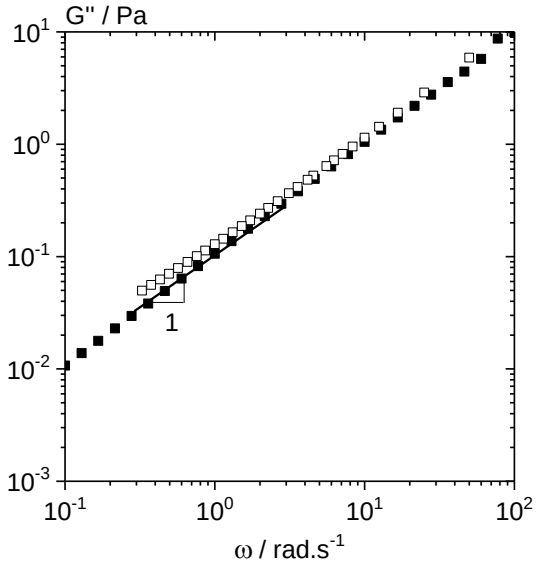

Figure 2.3 - Frequency-dependent viscous modulus G´´ obtained from rotational rheometry (solid squares) and calculated from the ensemble average MSD (open squares) for a 1 wt.% alginate aqueous solution

Additionally, the value of the non-Gaussian parameter α, calculated for the whole ensemble of MSDs is α≈1, which is a strong indicator for the homogeneity of the solution. This parameter describes the deviation of the MSD values from a Gaussian distribution expected for a homogeneous, uniform sample [143]. This quantity is zero for a Gaussian distribution, while broader distributions result in large values $\alpha \gg 0$. Similar, low α-values were found for all other solutions irrespective of the concentration and solvent used confirming the homogeneity of those systems. From the average MSD shown in Fig. 2.2

we extracted the linear viscoelastic moduli G' and G'' using the generalized Stokes-Einstein relation. Unphysical storage modulus values G' (not shown) are obtained due to the limitation of the Laplace transform for this weakly elastic solution and only the loss modulus G'' is shown. Fig. 2.3 shows very good agreement between G'' data obtained from MPT and bulk rheology in the shared frequency range, as expected for a Newtonian fluid the loss modulus increases linearly with frequency. However, for alginate solutions at concentrations > 1 wt.%, that exhibit a significant degree of bulk elasticity (G' > 100 Pa) but very short relaxation times (< 0.05 s), MPT viscoelastic moduli cannot be determined accurately due to the limitation of the MPT technique to measure very small particle displacements. Indeed, the lower limit of accessible MSD is ~10^{-4} μm^2 which corresponds to the static error of our setup [144]. Despite this limitation, we were able to determine the non-Gaussian parameter α for these highly concentrated solutions, but only at lag times higher than that corresponding to the static error.

2.3.3 Comparison of steady shear measurements, oscillatory shear and squeeze flow rheometry as well as DWS microrheology

In this section, we investigate the flow behaviour of a 3 wt.% alginate aqueous solution characterized using various mechanical techniques, namely steady rotational shear and capillary rheometry, oscillatory shear and squeeze flow, as well as DWS optical microrheology. We observe very good agreement between different methods over a broad frequency/shear rate range from 0.01 to 10^6 s^{-1} as shown in Fig. 2.4. The complex viscosity $|\eta^*|$ data, obtained from oscillatory shear and squeeze flow mechanical rheometry as well as DWS microrheology agree very well with steady shear viscosity η data determined from rotational and capillary rheometry, demonstrating that the Cox-Merz rule is valid for the system investigated. Particularly, at high frequencies/shear rates, $\omega/\dot{\gamma} > 10^3$ s^{-1}, the flow curve from DWS measurements agrees very well with the data obtained from capillary rheometry, which is the prevalent technique to measure viscosity in the high shear regime. In this case, DWS has the advantage of very low sample amount, ca. 2 mL, whereas for capillary rheometry around 100 mL of material is necessary. DWS optical microrheology proves to be a suitable complementary technique to the mechanical rheometry, especially in the frequency

range that rotational rheometry cannot cover. Variations of rheological parameters with alginate concentration, solvent and temperature will be shown and discussed in the next section.

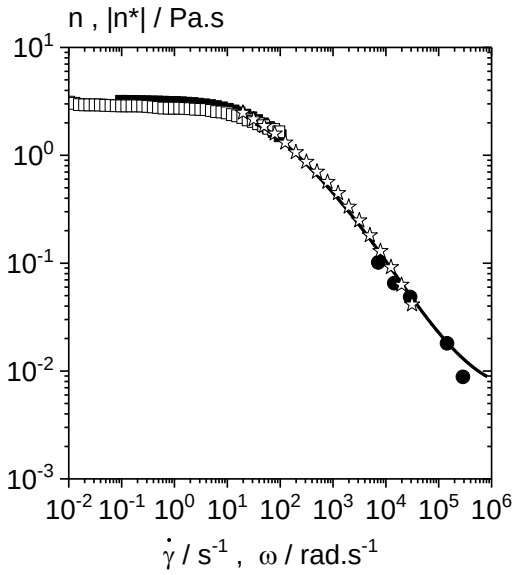

Figure 2.4 - Flow curve of a 3 wt.% alginate aqueous solution at 20°C. Steady shear viscosity from rotational (open squares) and capillary (solid circles) rheometry. Absolute value of complex viscosity from oscillatory shear (closed squares) and oscillatory squeeze (open stars) flow, as well as DWS (solid line)

2.3.4 Scaling behaviour of the specific viscosity η_{sp} dependence on alginate concentration

The specific viscosity η_{sp} is defined as $\eta_{sp} = (\eta_0 - \eta_s)/\eta_s$, where η_0 and η_s are the zero-shear viscosity and solvent viscosity, respectively, and has been determined from steady shear measurements. The concentration dependence of the specific viscosity η_{sp} for alginate in aqueous salt free system is shown in Fig. 2.5. We distinguish three regimes according to the different power law dependence in concentration $\eta_{sp} \sim c^n$ with *n* being the scaling exponent.

At dilute alginate concentrations (c< 0.2 wt.%), we observe a power law dependence $\eta_{sp} \sim c^{0.6\pm0.1}$ which is consistent with that expected for salt free polyelectrolytes in the semi-dilute, unentangled regime. For 0.2 wt.% < c < 1 wt.%, $\eta_{sp} \sim c^{1.6\pm0.1}$ and corresponds to the behaviour of salt free polyelectrolytes in the semi-

dilute, entangled regime. At higher concentrations (1 wt.% < c < 7 wt.%), we found $\eta_{sp} \sim c^{3.4\pm0.1}$, this exponent is slightly lower than the prediction for entangled solutions of neutral polymers in good solvent and polyelectrolytes in the high salt limit where $\eta_{sp} \sim c^{3.75}$ [21]. Similar exponents have been obtained in all three concentration regimes in other studies on aqueous alginate solutions [117,118]

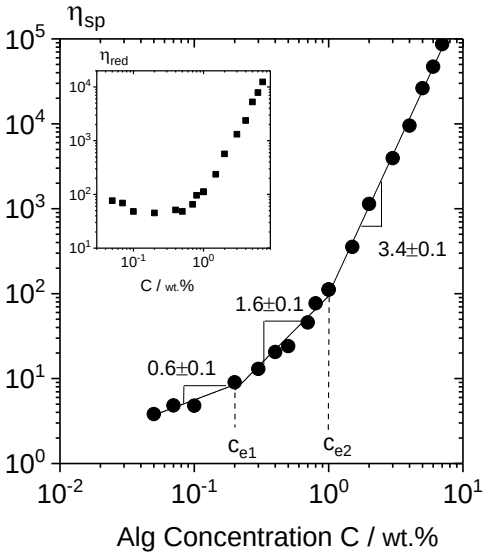

Figure 2.5 - Specific viscosity as a function of alginate concentration in salt free solutions at 20°C. Error bars are smaller than the size of the symbols. Inset shows the reduced viscosity as a function of alginate concentration

Two critical concentrations are thus assigned to the two changes of slope displayed in Fig. 2.5, namely, c_{e1} and c_{e2}. Here c_{e1} is the concentration separating the semi-dilute unentangled and the semi-dilute entangled regime for salt free polyelectrolytes, whereas c_{e2} marks the transition from this entangled regime for salt free systems to the entangled regime for polyelectrolytes in the high salt limit which is similar to that of neutral polymers in good solvents. Indeed, in this highly concentrated regime, the presence of free ions in the solution screens the electrostatic interactions strongly and the behavior of the solution changes from a salt-free polyelectrolyte system to a polyelectrolyte in the high salt limit when polymer concentration is increased and their behaviour then is similar to neutral polymers in good solvent. We found $c_{e1} = 0.2$ wt.%, corresponding to a minimum in the reduced viscosity dependence on concentration (inset of Fig.2.5) [21,118] and $c_{e2} = 1$ wt.%. In the rest of the study, we will focus on the third concentration regime, because the high viscosity values in this

regime are required for bioprinting applications. More specifically, we will investigate the effect of alginate concentration on different rheological parameters in three different solvents: Milli-Q water, PBS and DMEM.

2.3.5 Effect of alginate concentration on η_{sp}, G_0 and T_R in salt free, PBS and DMEM solutions

Variations of η_{sp}, G_0 and T_R as a function of alginate concentration in the entangled regime for the three different solvents are shown in Fig. 2.6a, 2.6b and 2.6c, respectively. The specific viscosity η_{sp} has been determined from steady shear measurements, G_0 and T_R from DWS microrheology as described above. The main advantage of the DWS technique is that it covers a very broad frequency range from low ~10 rad.s^{-1} to high frequency up to 10^6 rad.s^{-1} and thus allows for a determination of both parameters directly from the measured G' and G'' data.

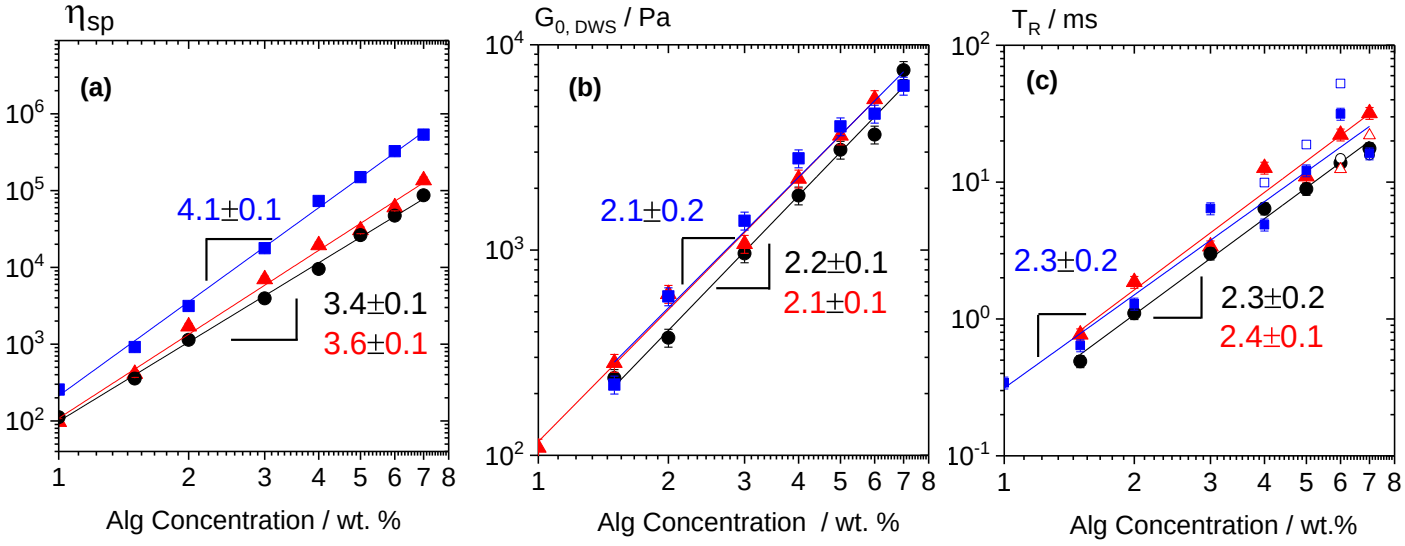

Figure 2.6 - Variation of the specific viscosity (**a)**, plateau modulus (**b)**, and relaxation time (**c)** as a function of alginate concentration in water (black), PBS (red) and DMEM (blue) at 20°C. For (**a)** and (**c)** error bars are as large as the size of the symbols

As already mentioned, for alginate in aqueous salt free solution the specific viscosity scales as $\eta_{sp} \sim c^{3.4\pm0.1}$ with a scaling exponent approaching the one expected

for neutral polymers in good solvent. For alginate in PBS, we found a slightly higher exponent $\eta_{sp} \sim c^{3.6\pm0.1}$ which is in very good agreement with theoretical predictions for polyelectrolytes in the high salt limit and neutral polymers in good solvent. However, for alginate in DMEM, an even stronger concentration dependence is found, $\eta_{sp} \sim c^{4.1\pm0.1}$, approaching the scaling behavior expected for neutral polymers in Θ solvent, $\eta_{sp} \sim c^{4.7}$. Other differences between salt free, PBS and DMEM solutions reside in the absolute values of η_{sp}. Compared to salt free solutions, η_{sp} increased by a factor ~2 for solutions in PBS, and by a factor of ~7 for solutions in DMEM. This difference in solvent quality might be related to the formation of polyelectrolyte complexes in DMEM solutions. DMEM contains many amino acids and these might interact with carboxylic groups from alginate to form polyelectrolyte complexes leading to stiffer gels and higher absolute values of the viscosity as compared to solutions in water or PBS. The presence of such interactions between alginate and amino acids have been proved by Di Cocco et al. [145] performing ^{1}H-NMR measurements. Variation of the plateau modulus G_0 with alginate concentration in the different solvents is shown in Fig. 2.6b. Within experimental error, the three scaling exponent values found for this parameter agree very well and coincide with theoretical predictions for neutral polymers in good as well as in Θ solvent ($G_0 \sim c^{2.3}$). For the relaxation time T_R dependence on concentration (Fig. 2.6c), no significant difference is observed among the solvents with $T_R \sim c^{2.3-2.4}$. For alginate in DMEM, the scaling exponent for T_R similar as for η_{sp} and G_0 agrees well with predictions for neutral polymers in Θ solvent. Whereas for salt free and PBS systems the exponent deviates from the prediction for neutral polymers in good solvent ($T_R \sim c^{1.6}$) as it has been obtained for η_{sp} and G_0. Similar unexpected T_R scaling has already been observed for hyaluronic acid [101] and alginate solutions [118]. One may attribute this deviation to the formation of aggregates or large supramolecular structures on the order of 100 nm at these high alginate concentrations, as it has already been observed for other polysaccharides [146]. It should be noted that relaxation time values obtained from rotational rheometry (open symbols) deviate slightly from those obtained from DWS (closed symbols) (Fig. 2.6c). This may be due to the inaccuracy of rotational rheology data in the frequency range 30 rad.s^{-1} < ω < 100 rad.s^{-1} which corresponds to the upper frequency limit accessible by this technique.

2.3.6 Effect of temperature on η_{sp}, G_0 and T_R.

Increasing the temperature from 20 to 60°C decreases η_{sp} and G_0 by approximately a factor of 2 and this corresponds to a strong increase in chain mobility. Fig. 2.7 shows modulus data for a 4 wt.% alginate aqueous salt free solution obtained from DWS measurements at three different temperatures 20, 37, and 60 °C. The terminal zone and the Maxwell relaxation frequency ω_R are strongly shifted towards higher frequencies, i.e. the relaxation time T_R decreases as expected.

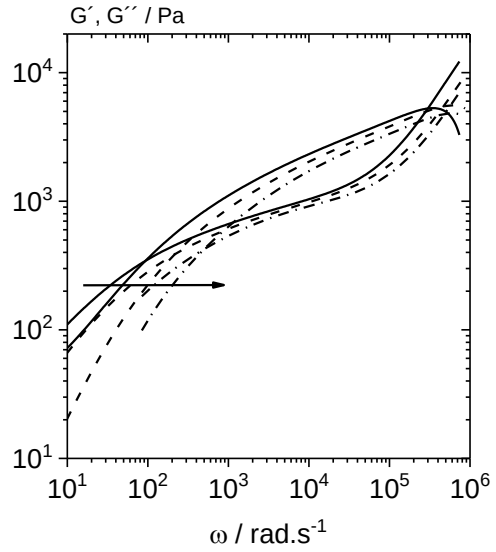

Figure 2.7 - Dynamic shear moduli G′ and G″ of a 4 wt.% alginate salt free aqueous solution as a function of frequency obtained from DWS measurements at 20 °C (solid line), 37 °C (dashed line) and 60 °C (dash-dotted line)

The activation energy E_A required for the relaxation of the system can be calculated from the slope of the semilogarithmic plot of T_R versus of 1/T. We found an activation energy of 34 kJ/mol, which is in the same range as reported for other polysaccharides [101,147].

Finally, the scaling exponents describing the concentration dependence of η_{sp}, T_R and G_0 are summarized in Table 2.2. The scaling exponents obtained at 37°C are essentially the same as those obtained at 20°C indicating no substantial change of polymer structure or conformation in this temperature range.

Table 2.2 - Concentration dependence of η_{sp}, T_R and G_0 at 20°C and 37°C for alginate dissolved in salt free water, PBS and DMEM solvents.

	20°C			37°C		
	η_{sp}	G_0	T_R	η_{sp}	G_0	T_R
Alginate in **salt free**	$c^{3.4\pm0.1}$	$c^{2.2\pm0.1}$	$c^{2.3\pm0.2}$	$c^{3.4\pm0.1}$	$c^{2.2\pm0.1}$	$c^{2.3\pm0.2}$
Alginate in **PBS**	$c^{3.6\pm0.1}$	$c^{2.1\pm0.1}$	$c^{2.4\pm0.1}$	$c^{3.7\pm0.2}$	$c^{2.2\pm0.2}$	$c^{2.1\pm0.1}$
Alginate in **DMEM**	$c^{4.1\pm0.1}$	$c^{2.1\pm0.2}$	$c^{2.3\pm0.2}$	$c^{4.3\pm0.2}$	$c^{2.1\pm0.2}$	$c^{2.5\pm0.1}$

2.3.7 Persistence length l_p in different solvents

Fig. 2.8 shows the variation of l_p as a function of alginate concentration in aqueous salt free, PBS and DMEM solutions as determined from ω_0 (Eq. 2.2). Within experimental error l_p is almost independent of alginate concentration for each solvent with an average value of l_p = 15.4±0.6, 15.8±2.5, 12.2±1.5 nm in aqueous salt free, PBS and DMEM solution, respectively. The slightly lower l_p value observed in DMEM solution indicates an increase in chain flexibility which also argues for a different polymer conformation in this solvent as compared to water and PBS solutions. Similar l_p values were obtained in previous studies based on intrinsic viscosity [126] or size-exclusion chromatography [129] measurements for dilute aqueous alginate solutions in salt free solutions and in presence of NaCl.

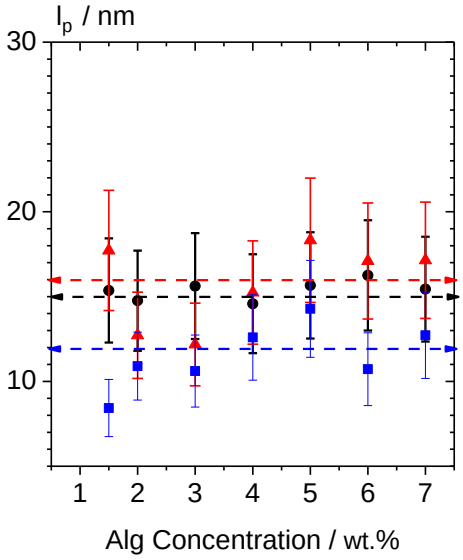

Figure 2.8 - Variation of the persistence length l_p as a function of alginate concentration in aqueous salt free (black circles), PBS (red triangles) and DMEM (blue squares) solutions obtained from the crossover frequency of the $\omega^{5/9}$ and $\omega^{3/4}$ scaling regime obtained from DWS

The fact that the persistence length does not depend on the polysaccharide concentration in this high concentrated regime is in good agreement with the variation predicted by the Odijk-Skolnick-Fixman (OSF) theory [148,149]. In this theory, for polyelectrolytes, the total persistence length is defined as $l_{p,T} = l_{p,0} + l_{p,e}$ where $l_{p,0}$ is the intrinsic persistence length due to the rigidity of the uncharged chain and $l_{p,e}$ the electrostatic persistence length contribution arising from the repulsion between adjacent ionic sites. With increasing polymer concentration and/or ionic strength, $l_{p,0}$ keeps constant whereas $l_{p,e}$ decreases. The relation $l_{p,e} = 1/(4\kappa^2 l_B)$ holds when the structural charge parameter ξ >1. This parameter is defined as the ratio of the Bjerrum length l_B (0.713 nm in water) and the distance a between two adjacent ionic sites. For sodium alginate *a* = 0.5 nm and, hence, ξ=1.4 which means that counterions condense. The Debye-Hückel screening length κ^{-1} is related to the ion concentration, i.e. to the ionic force *I* through $\kappa^{-1} = (4\pi l_B I)^{-1/2}$. For a monovalent 1:1 electrolyte, *I* is identified with the free ion concentration $c_f = \frac{c}{\xi} + 2c_s$, where c is the polymer concentration and c_s is the excess salt concentration, thus we obtain $\kappa^2 = 4\pi l_B c_f$.

Fig. 2.9 shows the variation of the total persistence length $l_{p,T}$ measured experimentally using DWS and the variation predicted by the OSF theory $l_{p,OSF}$ as a

function of the concentration of free monovalent ions in an aqueous salt free system. For the OSF calculation, we approximate $l_{p,T} \approx l_{p,0}$ = 15.5 nm for the solution with the highest polysaccharide concentration (7 wt.%); as for this sample, $l_{p,e} = 0.16\,\mathrm{nm}$ is negligibly small.

We observe that $l_{p,T}$ is almost independent of ionic strength throughout the experimental range investigated here, consistent with the small contribution of $l_{p,e}$ decrease (<0.75 nm) in this concentration range as predicted by the OSF theory. The inset in Fig. 2.9 emphasizes this result.

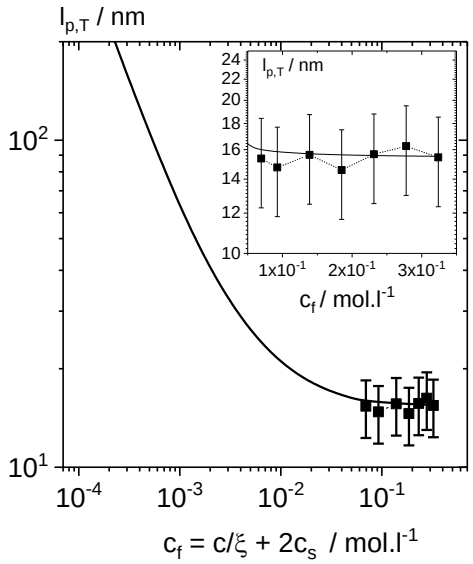

Figure 2.9 - Variation of the total persistence length $l_{p,T}$ measured (closed squares) and calculated from OSF theory (solid line) as a function of the concentration of free monovalent ions c_f in an aqueous alginate solution. Inset: close up of the experimentally accessed concentration range

Next, we have investigated the variation of l_p as a function of temperature (20, 37 and 60°C) for a 4 wt.% alginate sample in aqueous salt free, PBS and DMEM solutions (Fig. 2.10). In all cases, l_p is independent of temperature within experimental error, and alginate chains dissolved in DMEM are slightly more flexible compared to the solutions in PBS and de-ionized water at all investigated temperatures.

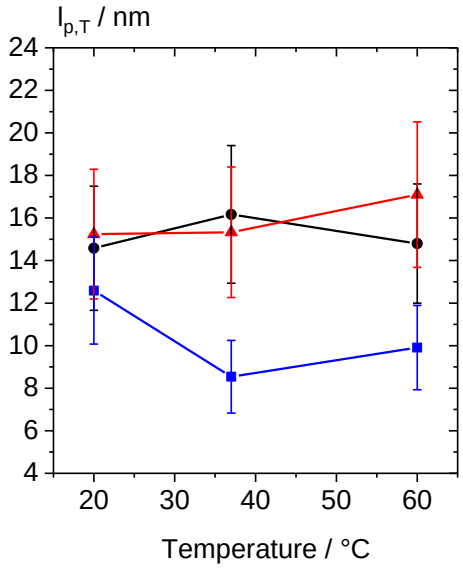

Figure 2.10 - Variation of the persistence length l_p as a function of temperature in aqueous salt free (black circles), PBS (red triangles) and DMEM (blue squares) solutions

This indicates that the chain conformation seems not to change in this temperature range as already indicated by the temperature dependence of the G_0, T_R and η_{sp} data.

2.4 Conclusions

In this work, we have used mechanical rheometry in combination with DWS and MPT optical microrheology to characterize linear viscoelastic properties of alginate in aqueous salt free systems and for the first time also in PBS as well as in DMEM solutions in a frequency range from 10^{-1} to 10^{6} rad.s^{-1} and on a micrometer length scale. At concentrations higher than 1wt.%, relevant for bioprinting, alginate solutions in salt free water and PBS exhibit scaling exponents for the concentration dependence of the specific viscosity η_{sp} and the plateau modulus G_0 that agree well with theoretical predictions for neutral polymers in good solvent. For the terminal relaxation time T_R, a slightly stronger concentration dependence is observed compared to theoretical predictions, presumably due to the formation of aggregates in this high alginate concentration regime.

For alginate dissolved in DMEM, all scaling exponents for η_{sp}, G_0 and T_R agree with predictions for neutral polymers in theta solvents, i.e. the investigated solvents

provide clearly different solvent quality. The distinctly different solvent quality of DMEM might be due to the formation of polyelectrolyte complexes in this solvent, due to interactions between alginate and amino acids present only in DMEM. This result is supported by lower persistence length values for DMEM solutions as determined directly from high frequency rheological measurements for the first time. Whether this difference in the chain flexibility due to solvent quality affects the cell adhesion or not has to be addressed in future research. Additionally, the scaling exponents for η_{sp} , G_0 and T_R do not change with temperature (20°C < T < 60°C). This is also true for the observed l_p values. These findings suggest that alginate chain conformation seems not to change with temperature. This result indicates that it is possible to vary the bioink temperature during the printing process without any change of the polymer conformation. Finally, MPT results clearly reveal a homogeneous structure of alginate solutions down to the 200 nm length scale in the concentration range investigated here.

Publication II

3 The influence of rheological and wetting properties of hydrogel-based bio-inks on extrusion-based bioprinting (EBB)

Full title: The influence of rheological and wetting properties of hydrogel-based bio-inks on extrusion-based bioprinting (EBB)

Authors: Bruna Regina Maciel, Kubilay Baki, Claude Oelschlaeger and Norbert Willenbacher

Status: published

Maciel, B.R., Baki, K., Oelschlaeger, C. and Willenbacher, N. (2022), The Influence of Rheological and Wetting Properties of Hydrogel-based Bio-Inks on Extrusion-based Bioprinting. *Chemie Ingenieur Technik*, 94: 393-401. https://doi.org/10.1002/cite.202100139

Abstract

We investigate wall slip and flow behavior of alginate as well as gelatin based hydrogels with respect to the impact of these rheological and wetting properties on extrusion based bioprinting (EBB). Capillary rheometry and printing tests indicate that slip is negligible at high stresses relevant for EBB, i.e. well above the hydrogels yield stress. On the contrary, rotational rheometry performed at low shear stresses revealed that alginate hydrogels present much stronger slip than gelatin gels, irrespective of crosslinker and polymer concentration. This result is presumably due to the formation of a heterogeneous microstructure for alginate gels and has an unfavorable impact on the printing quality with the production of large fluctuations in line width and higher line spread ratio.

3.1 Introduction

Bioprinting enables the deposition of living cells at specific positions in the printed scaffold, forming three dimensional constructs that mimic the human tissue micro-environment [25,34]. This 3D configuration enhances cell proliferation similarly to the one of the living tissue, which may not be the case for most 2D cell culture methods [80,150]. The most commonly employed techniques for bioprinting are the extrusion-based bioprinting (EBB), material jetting or inkjet bioprinting as well as vat polymerization (VP) [25]. Although material jetting and vat polymerization bioprinting both offer higher printing resolution (<100 μm) in comparison to EBB, low viscosity materials are required for inkjet bioprinting (3-30mPas) and nozzle clogging is a recurrent issue [151,152]. Moreover, VP bioprinting struggles with the limited choice of photo-curable biomaterials and use of single bio-resin [151]. EBB, on the other hand, is widely used due to its versatility, affordability and facility to operate [27]. EBB allows a broad range of bioinks viscosity (30– 10^7 mPa s) to be printed, as well as a higher throughput rate in comparison to the other techniques [25]. During the pneumatic EBB process, a mixture of living cells and a carrier material is extruded through a nozzle controlled by an external pressure. This mixture is the so called bioink. Biocompatible polymeric hydrogels are often used as cell carrier materials [153,154]. Due to their high water content, hydrogels are prone to wall slip under flow [155,156]. Slip behavior occurs when a thin liquid layer is formed between the wall and the hydrogel, apparently invalidating the often tacitly assumed no-slip assumption. Slip flow can be controlled by employing wall materials with different wettability properties [33,157,158]. Precision nozzles made from stainless steel are widely used for bioprinting [159,160]. Nevertheless, nozzles made of polymers, such as polytetrafluoroethylene (PTFE) and polypropylene (PP) are also found on the market. The flow behavior through the nozzle during bioprinting was studied for shear thinning materials considering that the no-slip condition is valid [159,161–163]. The effect of wall slip on nozzle flow and printing behavior of biopolymer solutions has also been investigated [164,165]. These studies, however, rely on a narrow range of shear rate controlled rheological measurements not

taking into account that the slip velocity generally strongly depends on the applied stress [166].

In this study we discuss the phenomenon of wall slip on EBB quality using two different types of bioinks, namely alginate- and gelatin-based hydrogels. First, we performed rotational rheometry experiments employing parallel-plate geometries made of different materials, *i.e.* with different surface energy values, namely PTFE, polypropylene and stainless steel. In this case, we determined the wall slip velocity under controlled shear stress conditions similar as in an EBB experiment. The accessible absolute stress values, however, are lower than typically applied during printing. Additionally, we used rotational rheometry to determine the yield stress and the elastic shear modulus of the hydrogels. Then, capillary rheometry was used to study the flow behavior under high shear conditions similar to those of EBB. In this case only stainless steel capillaries were used. Finally, we performed 3D printing experiments with nozzles made of different materials. We systematically determined the line resolution, shape fidelity and stability of multi-layered constructs post-printing. The results help to understand how wall slip, yield stress and elastic shear modulus of bioinks are related to the printing quality and will promote the development of tailor-made bioprinting strategies.

3.2 Materials and Methods

3.2.1 Sample preparation

Sodium alginate (alginic acid sodium salt from brown algae, BioReagent) and poly(vinyl alcohol) (PVA, Mowiol ® 4-98) were purchased from Sigma- Aldrich Chemie GmBH (Taufkirchen, Germany). Gelatin extra pure, gold, 180 Bloom, calcium chloride ($CaCl_2$) >98% dehydrated and calcium sulfate ($CaSO_4$) >98% dihydrate were purchased from Carl Roth (Karlsruhe, Germany). D-Glucono-1,5-lacton (GDL) >99% was purchased from Alfa Aesar (Thermo Fischer, Karlsruhe, Germany). Calcium carbonate ($CaCO_3$, Ulmer Weiss 15H) was purchased from Eduard Merkle GmbH (Blaubeuren-Altental, Germany). Alginate, $CaCl_2$, $CaSO_4$ and GDL solutions were prepared stirring the powder with Milli-Q water at room temperature until they appeared limpid and homogeneous. Gelatin and PVA solutions were prepared using the same procedure,

but stirring occurred at 40°C and 90°C, respectively. $CaCO_3$ suspension was prepared stirring the powder with Milli-Q water. Alginate samples A and B were prepared by mixing alginate solution with the salt solution. GDL was added to sample B in order to dissolve $CaCO_3$. Sample C was composed of only gelatin solution and sample D of gelatin mixed with PVA solution. The table below shows the composition details and final weight concentrations of the different ingredients for the investigated bioink systems:

Table 3.1 - Composition of alginate and gelatin-based samples.

	Alginate-based		**Gelatin-based**	
	A	**B**	**C**	**D**
Polymer	1.3% Alginate	1.3% Alginate	4% Gelatin	8% Gelatin + 2% PVA
Crosslinker	0.17% $CaSO_4$	0.13% $CaCl_2$ + 0.04% $CaCO_3$ + 0.04% GDL	-	-

3.2.2 Rotational rheometry

A rotational rheometer (Rheoscope I, Thermo Haake, Karlsruhe, Germany), equipped with a stainless steel plate-plate measuring cell (diameter 20 mm, roughness R_z = 2.1±0.3µm) was used to perform steady as well as small amplitude oscillatory shear experiments at 20 °C. The storage modulus *G'* of gels is typically independent of the applied frequency of shear deformation. Here this plateau value of *G'*, also called shear modulus G_0, was determined as the value of the storage modulus *G´* at an angular frequency of 1 rad.s^{-1}. Plates of different materials, namely polytetrafluoroethylene (PTFE, R_z = 3.2±0.3µm), polypropylene (PP, R_z = 1.9±0.5µm) and sand paper P320 (R_z = 59±16µm) were also attached to the plate-plate fixture. Laser scanning microscopy

(VK-X100 Keyence, Neu-Isenburg, Germany) was used to assess the roughness of the disk plates. Crosslinked hydrogels are solid-like materials at rest and a critical stress, generally termed apparent yield stress, has to be exceeded to enable flow [167]. Pronounced slip behavior often limits rheological characterization of hydrogels. Accordingly, plate fixtures with increased roughness are often used in rotational rheometry [168,169]. Here, yield stress determination was done based on creep tests employing the attached sand paper disk. The shear stress was stepwise increased from 1 to 1000 Pa. The yield stress was determined using the two-tangent method where deformation was plotted as a function of shear stress using logarithmic scales. Then, one tangent is fitted to the data in the low shear, elastic response regime while the second tangent is fitted to the plastic deformation region. The value extracted from the crossover of the two tangents is the yield stress [170]. Similar stress ramps were also applied to assess the slip behavior with the smooth plate-plate fixtures. Video recordings were performed using an objective borescope and a Digital Microscope VHX-950F Keyence (Neu-Isenburg, Germany) in order to visualize the deformation of the sample rim.

3.2.3 Capillary rheometry

High shear viscosity data were determined at 20°C using a self-assembled piston-driven capillary rheometer. The samples were forced to flow through stainless steel capillaries with different diameter (0.5 mm - 1.5mm) and lengths (30 – 90 mm) at controlled volumetric flow rates corresponding to constant shear rate values using a piston of 20 mm diameter. The resulting extrusion pressure was recorded using a pressure transducer (0 - 50 bar, Dynisco Europe GmbH, Heilbronn, Germany).

3.2.4 3D printing of hydrogels

The alginate and gelatin-based hydrogels were stained with blue ink (Pelikan, Berlin, Germany) for better visibility and printed on microscope glass slides using a pressure-controlled Voxel 8 Developer’s Kit 3D printer (Voxel 8 Inc., Harvard, USA). 3CC cartridges (Nordson EFD, Feldkirchen, Germany) and straight needles of different materials, namely stainless steel, PTFE and PP (250µm outlet diameter and 18 mm

length, VIEWEG, Germany), were used to extrude the hydrogels in a log pile pattern. The print head velocity was kept at 600 mm/min for all samples. The 3D constructs were imaged using a Digital Microscope VHX-950F (Keyence, Neu-Isenburg, Germany) and image analysis was performed with the software Image Processing System (Visiometrics iPS).

3.3 Results and Discussion

3.3.1 Rotational rheometry: low shear stress

Slip stress visualization and slip velocity determination

The slip behavior of alginate and gelatin-based hydrogels can be visually observed in the video snapshots in Fig.3.1. For sample B, an alginate-based hydrogel (Fig.3.1-a), no movement of the PTFE upper plate was observed for shear stress values lower than 15 Pa. Above this value, the upper plate starts moving and only a thin layer close to the plate is sheared whereas the rest of the sample remains intact (Fig.3.1-b). Similar pronounced wall slip behavior was observed for alginate samples A and B in contact with steel and PP plates. For gelatin-based gels C and D only slight slip was detected, *e. g.* for sample C (Fig.3.1-c), the stainless steel plate only starts moving at shear stress values above 167 Pa and deformation takes place in the upper half layer of the gel with only little slip (Fig.3.1-d). Similar minor slip behavior was observed when PTFE and PP plates were used. The shear stress at which the onset of slip can be visually observed is the so-called critical slip stress τ_S [157].

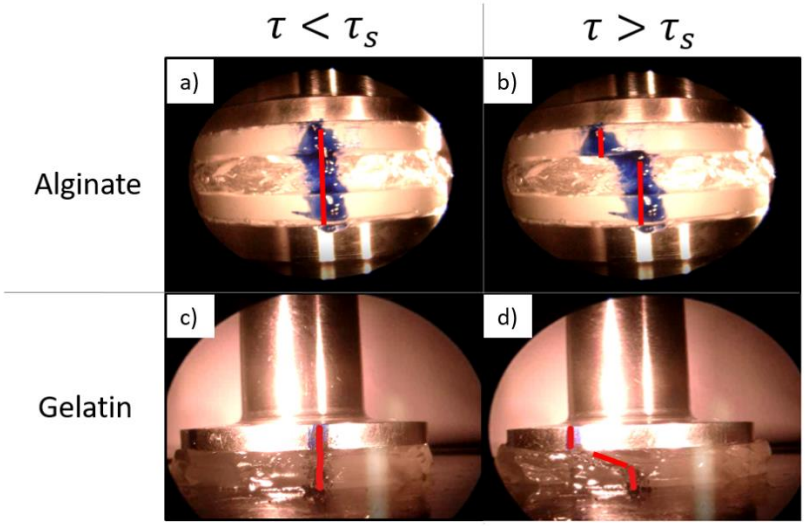

Figure 3.1 - Video snapshots of alginate-based sample B, at $\tau<\tau_S$ (a) and $\tau>\tau_S$ (b) and gelatin-based sample C, at $\tau<\tau_S$ (c) and $\tau>\tau_S$ (d) during shear stress ramp measurement with plate-plate rheometer.

Note that this critical stress τ_s for both types of material is well below the yield stress of the gels obtained with particularly rough plates. This will be discussed below in section 3.3.3. Moreover, slip even occurs below τ_s although it is not visually observable. Therefore, we adapted the approach developed by Yoshimura *et al.* to determine the slip velocity under flow by varying the gap height in a plate-plate rheometer [166,171]. In the experiments performed here, the samples deform elastically instead of exhibiting a steady shear flow. Accordingly, instead of obtaining the slip velocity from the slope of shear rate $\dot{\gamma}$ as a function of reciprocal gap height, the following relation is used:

$$\gamma_{app} = \frac{2V_s t_c}{h} + \gamma \qquad (3.1)$$

where γ_{app} is the apparent elastic deformation of the hydrogel including slip and γ is the true elastic deformation, t_c is a characteristic time constant, h is the gap height and V_s the slip velocity. The characteristic time constant t_c was considered 1 s for all samples at all shear stresses applied. Slip velocity data obtained for samples B and C are summarized in Fig. 3.2. Starting at the same low value $V_s \approx 3.10^{-3}\, mm.s^{-1}$ slip strongly increases with increasing shear stress for both samples. The slope of this

increase in the semi-log plot of $V_s\ vs.\tau$, however, is much more pronounced for the alginate than for the gelatin sample, whereas the critical stress τ_s at which slip starts to be visually accessible is much higher in the latter case.

For shear stresses higher than the slip stress τ_s, the slip velocity at the rim of the rotating plate is given by:

$$V_s = 2n\pi r \qquad (3.2)$$

where *n* is the plate rotational velocity and *r* is the plate radius [157]. This approach is justified by the video recordings discussed above. The onset corresponding data are also shown in Fig.3.2. Visual observability of slip corresponds to a slip velocity value $V_s \approx 0.5\ mm.s^{-1}$. For alginate this happens at a much lower stress value than for the gelatin sample, as already pointed out above. Moreover, the increase of V_s with τ is much more pronounced for alginate than for the gelatin gel. For both materials a pronounced kink in the $V_s\ vs.\tau$ curves shows up around τ_s and for both materials the upper limit at which V_s can be determined using a plate-plate rotational rheometer is set by sample spillage which occurs at significantly lower stresses for the alginate than for the gelatin sample.

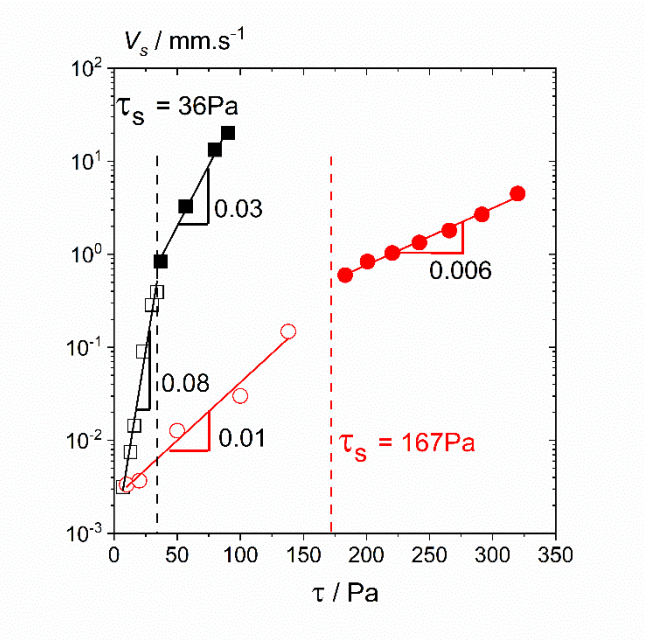

Figure 3.2 - Slip velocity V_s as a function of shear stress τ for alginate-based sample B (squares) and gelatin-based sample C (circles) determined with stainless steel plate-plate fixture. Open symbols refer to data obtained using a modified Yoshimura *et al.* approach based on a variation of gap height (Eq. 3.1). Closed symbols refer to data directly calculated from the rotation of the upper plate (Eq. 3.2).

Effect of plate-plate materials on slip stress τ_S

Slip stress τ_S values for samples A-D loaded on different plate-plate geometry materials can be seen in Fig. 3.3. Overall, samples on stainless steel plates present higher slip stress than on PTFE and PP, except for gelatin sample C. Here the slip stress for steel is almost the same as the one for PP. PTFE plates present in general the lowest slip stress value, except for gelatin sample D where the values for PP and PTFE plates are very similar. This result indicates larger wall slip effects occurring using PTFE plates compared to steel plates. The higher adhesion or friction of the hydrogels to stainless steel can be explained by its higher surface energy (~43mJ/m², [172]) compared to PP and PTFE, which present a surface energy of ~33mJ/m² and ~31.5mJ/m² [173], respectively.

Another observation is that, independent of crosslinker type and sample composition, alginate-based hydrogels are more susceptible to slip compared to gelatin-based gels. For the alginate samples, slip stress τ_S values are below 40 Pa, whereas

for gelatin-based hydrogels τ_S is always larger than 100 Pa. A possible explanation for the difference in wall slip performance might be the distinct chemical composition of alginate (polysaccharide) and gelatin (protein) hydrogels. In an earlier study on food hydrogels, whey protein isolate gels were found to have a higher surface friction than gels containing polysaccharides [174], therefore leading to less slip.

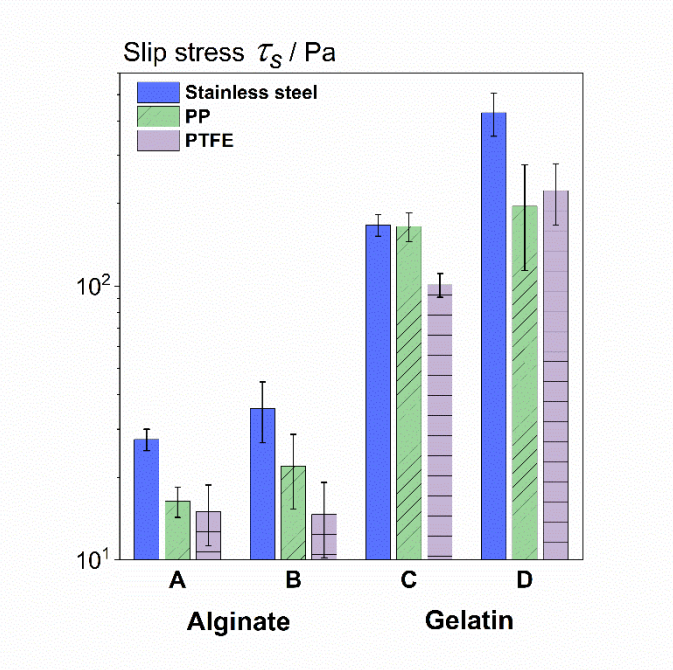

Figure 3.3 - Slip stress τ_S for samples A-D measured with stainless steel plate (blank bars), PP (diagonally patterned bars) and PTFE (horizontally patterned bars).

Effect of sample composition and plate-plate materials on slip velocity V_S

The slip velocity V_S for $\tau > \tau_S$ strongly increases with τ for all samples, as shown in Fig. 3.4. Both alginate samples A and B share similar dependence of V_S on τ, despite the fact that sample A was crosslinked with $CaSO_4$ and sample B with a mixture of $CaCO_3$ and $CaCl_2$. The same is observed for gelatin samples C and D, even though sample D has a higher polymer concentration than sample C. No clear trend in the V_S among steel, PP and PTFE plates is observed for samples A-D. Similar results (not

shown) were obtained for $\tau<\tau_S$. Overall, slip velocities found for alginate gels are much higher than those found for gelatin samples.

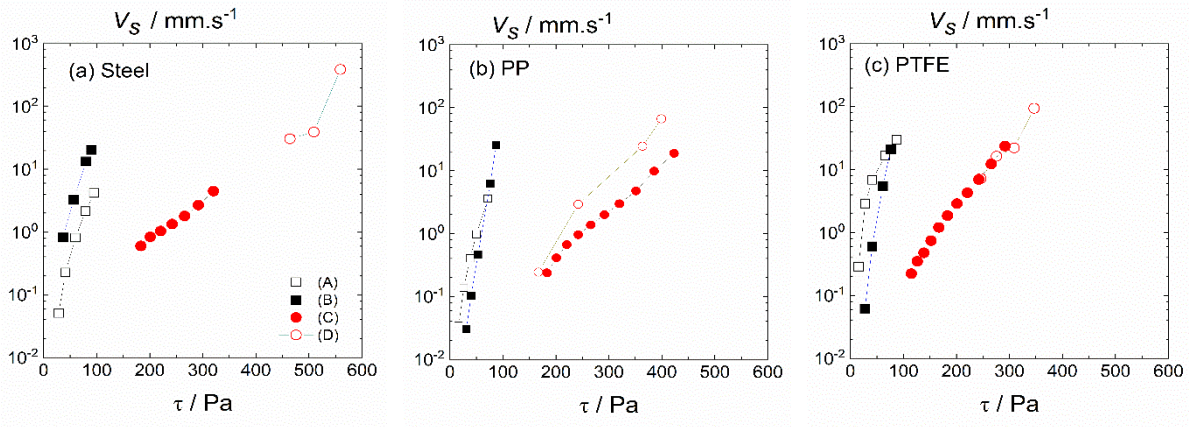

Figure 3.4 - Slip velocity V_S of alginate-based samples A and B and gelatin-based samples C and D as a function of τ for $\tau>\tau_S$, measured using steel (a), PP (b) and PTFE (c) plate-plate geometries.

3.3.2 Capillary rheometry: high shear stress

Capillary rheometry allows us to investigate flow behavior at higher shear rate values, in a range relevant for the 3D printing process (10^3 – 10^5 s^{-1}). Three capillary nozzles of different diameter *d* and length *L*, but same ratio *L/d*=30, were used to extrude the alginate hydrogel at shear rates >4.10^2 s^{-1}, with corresponding shear stresses τ > 2.10^2 Pa. As can be seen from Fig. 3.5, the flow behavior of sample B is nozzle size independent, suggesting that slip is negligible at such high shear stress values. Similar results were found for the other samples. In other words, despite the pronounced slip observed at low stress, we can safely neglect wall slip effects at shear stresses relevant during EBB for the alginate and gelatin gels investigated here.

Fig. 3.6 displays the viscosity of alginate sample B and of gelatin sample C as a function of shear rate. Notably, the samples show pronounced shear thinning and essentially equal viscosity values η in the broad shear rate range covered by combining rotational and capillary rheometry.

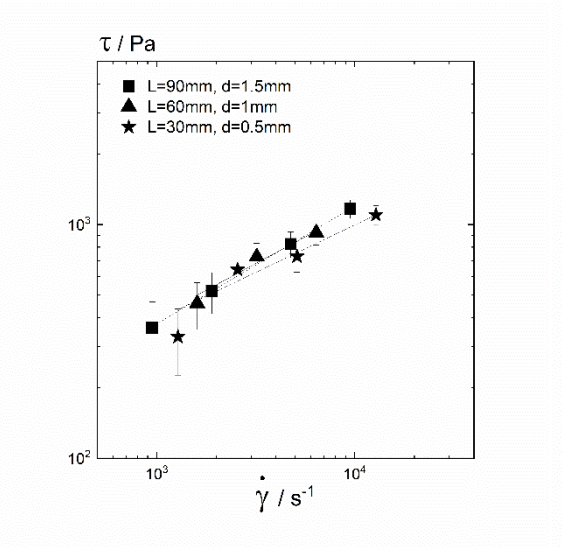

Figure 3.5 - Flow behavior of alginate-based sample B measured with a capillary rheometer. Shear stress as a function of shear rate for different stainless steel nozzle sizes.

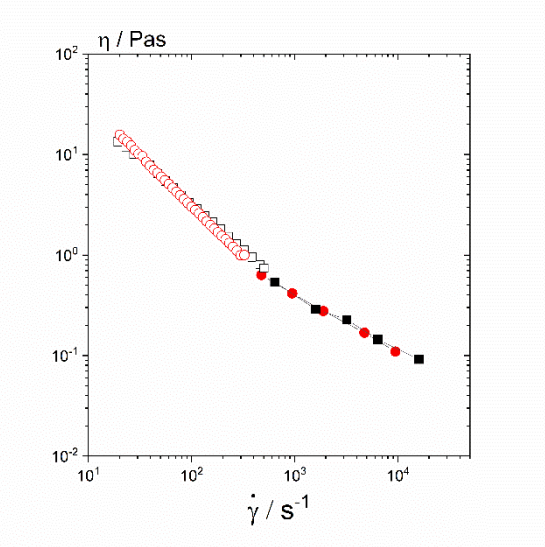

Figure 3.6 - Viscosity η as a function of shear rate for alginate-based sample B (squares) and gelatin-based sample C (circles) as obtained from rotational rheometry with rough plates (open symbols) and capillary rheometry (closed symbols).

3.3.3 Yield stress τ_y determination and comparison with slip stress τ_s

Fig. 3.7 shows the yield stress τ_y values measured with rough plates for samples A-D in comparison to the critical slip stress τ_s measured with smooth stainless steel plates. In all cases, $\tau_y > \tau_s$. Alginate gels, however, present a larger ratio τ_y/τ_s in comparison to gelatin gels, emphasizing the strong slip of polysaccharide gels.

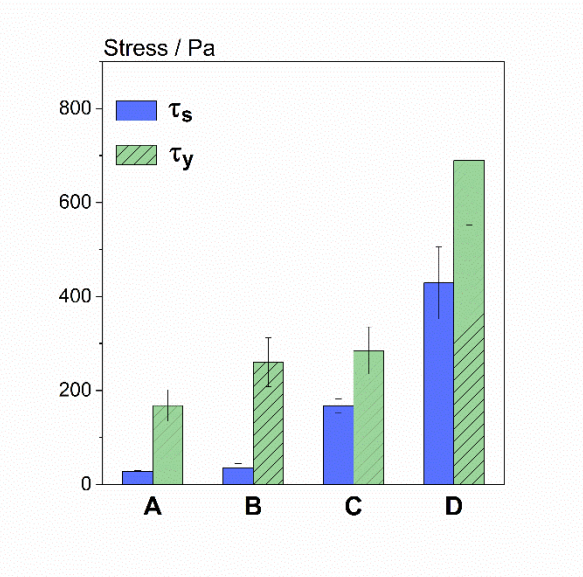

Figure 3.7 - Slip stress τ_s (blank columns) with steel plate and yield stress τ_y (patterned columns) for samples A-D.

Samples B and C show similar yield stress (Fig.3.7) and identical flow behavior (Fig.3.6). However, they present contrasting slip performance at low stresses, as previously discussed. In addition, slip is not significant for both gel types at high shear stress or high shear rate.

3.3.4 3D printing experiments

Next we compare the printing quality accessible with alginate and gelatin samples B and C, respectively, both exhibiting similar rheological properties and no slip at high stress relevant for printing. These two samples were 3D printed using needles of different materials. The lowest pressure necessary for printing continuous lines without interruptions or defects was found to be 0.17MPa for alginate-based sample B and, surprisingly, only 0.1MPa for gelatin-based sample C. These pressure values correspond to wall shear stress values of 598 Pa and 359 Pa, respectively. The wall shear stress τ_w is given by equation (3.3):

$$\tau_w = \frac{\Delta P.r}{2L} \qquad (3.3)$$

Where ΔP corresponds to the pressure difference and r and L are the needle radius and length, respectively.

Overall, the use of different needle materials does not affect the printing quality of the constructs substantially (Fig. 3.8). This indicates that the no-slip boundary condition is valid not only for the stainless steel nozzle as already confirmed by capillary rheometry (Fig.3.5), but also for the nozzles made from lower surface energy polymer materials. This is further confirmed by the analysis of the printed lines. In order to evaluate filament formation, the spreading ratio of the lines was calculated as the line width divided by the nozzle outlet diameter. The spreading ratio values for alginate-based sample B lines printed with steel, PP and PTFE needles are 5.1±1.2, 5±1 and 4.6±1.2, respectively, whereas gelatin-based sample C shows spreading ratio values of 3.9±0.5 for steel needles and 4.3±0.5 for both PP and PTFE needles.

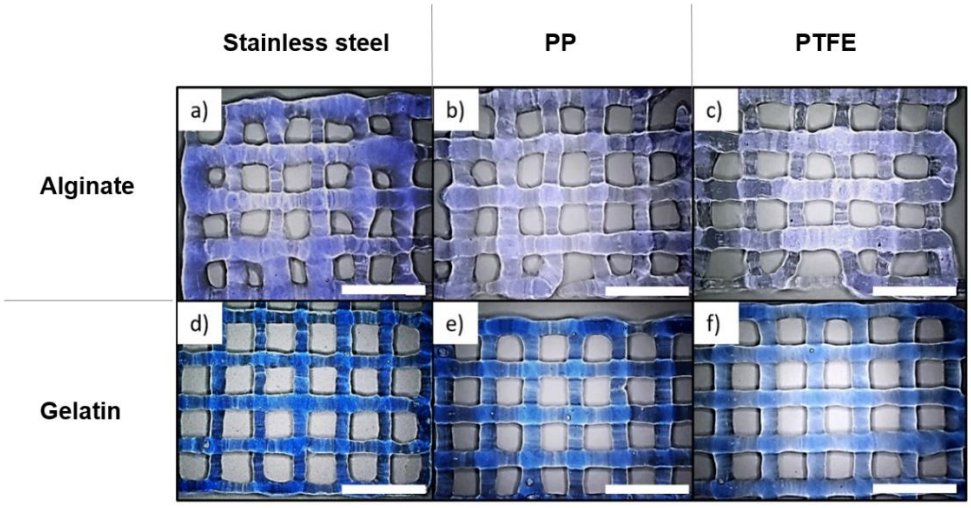

Figure 3.8 - 3D printed constructs. Upper row represents alginate-based sample B printed at 0.17 MPa and bottom row gelatin-based sample C printed at 0.1 MPa. Hydrogels were printed with stainless steel nozzle, a) and d), PP nozzle, b) and e), as well as PTFE nozzle, c) and f). Outlet diameter of all nozzles is 250μm. Scale bar: 5mm.

The pronounced slip effect observed at low shear stresses ($\tau < \tau_y$) is attributed to the different wetting behavior of the gels on different materials and thus may have an effect on the spreading of the first printed layer using different substrates. Lee *et al.* investigated the effect of printing platforms with varying surface energy on the line width of the printed constructs [175]. They found that hydrophobic substrates yielded thinner

printed lines in comparison to hydrophilic printing platforms. We did not follow up on this aspect here.

The pronounced slip behavior of the alginate-based samples for $\tau < \tau_y$ is unexpected considering that these samples contain essentially just a trace amount of polymer. Wall slip typically occurs in highly filled, dense suspensions [169]. Slip here may be interpreted as an indication of hydrogel phase separation and/or formation of structural micro-heterogeneities. The alginate gels may be treated as suspensions of micro-gel particles in a low viscosity aqueous polymer solution. The printed lines of the alginate sample B are irregular and non-uniform in comparison to the ones printed from gelatin sample C, as shown in Fig. 3.8. This effect is more evident in Fig. 3.9, where the variation of line width is plotted as a function of the position *x* along a printed strut.

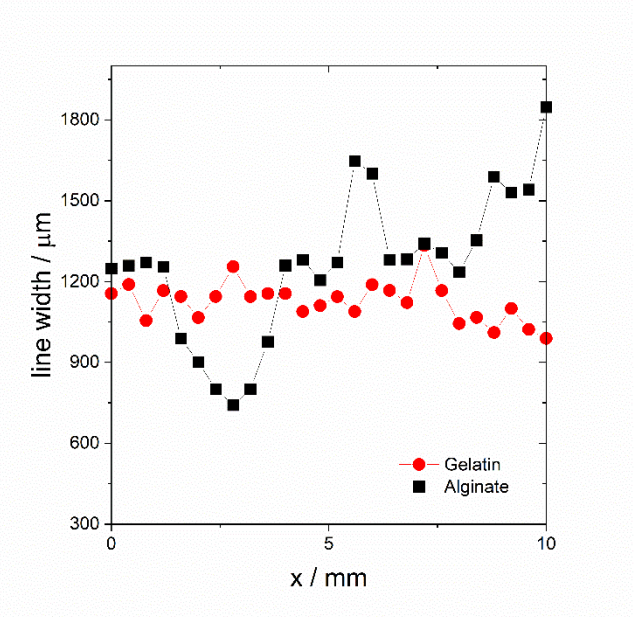

Figure 3.9 - Filament width as a function of the position along a printed filament for alginate-based sample B (squares) and gelatin-based sample C (circles).

The pronounced fluctuations in printed filament width observed for sample B as well as the need of a higher pressure to print continuous lines in comparison to sample C could be interpreted as a consequence of the hydrogel micro-heterogeneity suggested by the pronounced low-stress slip behavior found for the alginate gels. The characterization of such micro-heterogeneities in cell carrier hydrogels will be addressed in detail in a subsequent study.

In several previous studies the yield stress of bioinks is correlated to printing quality [30,32,47,47]. In order to investigate the effect of yield stress on printing quality for the hydrogels investigated here, 20-layer objects were printed using a stainless-steel nozzle (Fig. 3.10). Printing of multi-layered constructs from sample A was not possible due to its lack of elasticity and low yield stress. Table 3.2 summarizes slip stress, rheological parameters as well as printing pressure of hydrogels B-D.

Table 3.2 - Slip stress, yield stress, elastic modulus G_0, minimum printing pressure and corresponding wall shear stress for samples B-D.

	Slip stress / Pa	**Yield stress / Pa**	**G_0 / Pa**	**Pressure / MPa**	**Wall shear stress/ Pa**
Sample B	36±9	260±52	1900±380	0.17	598
Sample C	167±15	280±50	285±40	0.10	359
Sample D	429±77	690±138	1550±310	0.24	837

Samples B and C exhibit similar yield stress, while that of sample D is almost three times higher. This seems to have an effect on the top surface geometrical accuracy of the printed constructs (Fig.3.10 a-c). Sample D shows lower line spread ratio (Table 3.3), i.e. superior shape fidelity in comparison to samples B and C, presumably due to the higher yield stress. The poor top surface fidelity of sample B can be attributed to the inhomogeneous filament formation and higher spread ratio.

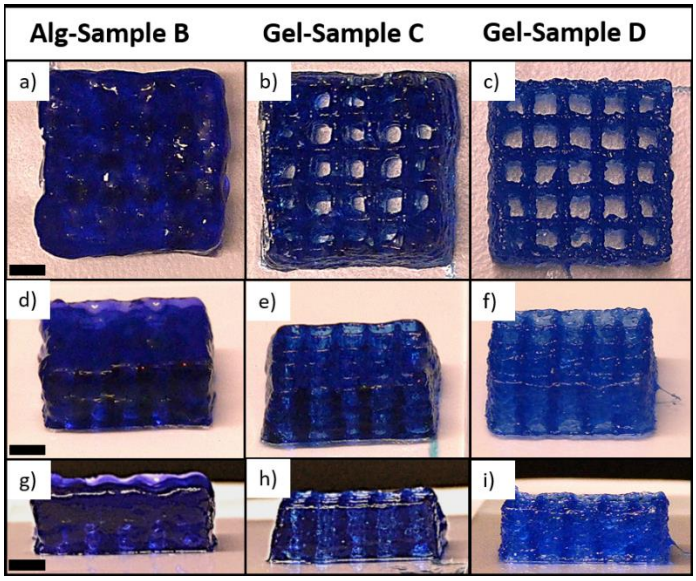

Figure 3.10 - 3D printed 20-layer log-pile constructs, total area ~15x15mm², height ~5mm. a), d) and g) refer to alginate-based sample B; b), e) and h) represent gelatin-based sample C; c), f) and i) gelatin-based sample D. Scale bar: 3mm

Samples B and D show a better layer stacking quality in comparison to sample C (Fig. 3.10 d-i). Possibly due to their higher elastic modulus values ($G_0 > 10^3$ Pa) in comparison to gel C ($G_0 \sim 285$ Pa), a more pronounced filament merging is observed for sample C, yielding a smaller top surface length in comparison to the bottom length of the 3D construct (Table 3.3). The low elasticity of this hydrogel and hence its poor resistance against gravitational sagging seems to cause layer collapse, resulting in multilayered constructs with lower height.

Table 3.3 - Printability parameters for samples B-D.

	Line spread ratio	**Top surface length / mm**	**Log pile height / mm**	**Layer height / µm**
Model	1	15	5	250
Sample B	5.1±1.2	15.6±1.5	5.9±0.2	295±10
Sample C	3.9±0.5	13.8±0.6	5.2±0.1	260±4
Sample D	3.3±0.6	15.3±0.5	5.4±0.1	270±7

In this study, a high elastic modulus G_0 yields a better layer stacking quality (samples B and D) while a higher yield stress is related to an improved filament formation and shape fidelity (sample D). This is in line with an earlier study using collagen hydrogels as printing ink reporting high printing quality for G_0 > 1000 Pa [68]. Besides, gel elasticity has to be adjusted to regulate matrix stiffness and cell proliferation [153]. Extremely high yield stresses, however, can lead to difficulties incorporating living cells or may cause nozzle clogging [32,68]. Lee *et al.* suggested a maximum yield stress value of 1000 Pa for collagen-based hydrogels allowing for extrusion through a nozzle of 400 µm diameter [68]. It should be noted that sample D (τ_y ~ 690 Pa) needs a higher extrusion pressure for continuous filament printing in comparison to samples B and C (τ_y < 300 Pa) (Table 3.2). A higher yield stress, and therefore higher printing pressure, results in a higher shear stress (Eq.3.3) experienced by the living cells while passing through the needle. This can lead to cell damage and low cell viability after printing [48,111].

3.4 Conclusion

In this work, we thoroughly investigated wall slip, flow behavior and elasticity of alginate as well as gelatin-based hydrogels with respect to the impact of these rheological and wetting properties on extrusion based bioprinting (EBB). At stresses below the yield stress τ_y, rotational rheometry revealed that alginate-based hydrogels presented stronger slip than gelatin samples, irrespective of crosslinker and polymer concentration. Slip at low stresses is more pronounced on PP and PTFE plates than on stainless steel plates for all samples. Capillary rheometry and printing tests using nozzles made from different materials (stainless steel, PP and PTFE) confirm that slip is negligible at stresses $\tau > \tau_y$ relevant for EBB. The strong slip at low stresses observed for the alginate gels, however, is indicative of a heterogeneous microstructure, presumably comprising a dense suspension of microgel particles in a low viscosity polymer solution. This seems to show up in the printing results when comparing an alginate gel and a gelatin sample with similar yield stress and viscosity. The presumably heterogeneous alginate sample requires a higher extrusion pressure for printing

uninterrupted lines and even more importantly exhibits strong fluctuations in line width and a higher line spread ratio. This striking observation demands further systematic investigations regarding the relevance of ink heterogeneity for printing quality and also cell viability. Finally, our EBB experiments confirmed that a higher yield stress of the bioink requires a higher extrusion pressure but improves the shape fidelity of multilayered 3D constructs, while increasing gel elasticity enhanced layer stacking quality.

Publication III

4 Targeted Micro-Phase Separation – a Generic Design Concept to Control the Elasticity of Extrudable Hydrogels

Full title: Targeted Micro-Phase Separation – a Generic Design Concept to Control the Elasticity of Extrudable Hydrogels

Authors: Bruna Regina Maciel, Ke Wang, Marc Müller, Claude Oelschlaeger and Norbert Willenbacher

Status: published

B. R. Maciel, K. Wang, M. Müller, C. Oelschlaeger, N. Willenbacher. Targeted Micro-Phase Separation – a Generic Design Concept to Control the Elasticity of Extrudable Hydrogels. *Materials & Design* (2023), 227, 111803

https://doi.org/10.1016/j.matdes.2023.111803

Abstract

Hydrogels are ubiquitous in nature and technology. Controlling their mechanical properties and under-standing their complex microstructure is critical e.g. for 3D bioprinting or tissue engineering applications. Here a generic design concept for tuning the elasticity of extrudable gels at given polymer or particle concentration is presented. Targeted micro-phase separation leading to micro-heterogeneities (1-100µm) yields high gel strength allowing for extrusion of uniform filaments with high shape accuracy as long as the heterogeneity length scale is small compared to the extruded filament diameter (>500µm). Micro-mechanical and structural heterogeneity was enhanced in alginate hydrogels by accelerating crosslinking kinetics, corresponding to gel elasticity variation of more than two orders of magnitude (17 Pa to 2300 Pa), enabling filament extrusion (1046 µm) with high shape fidelity. Introducing poly(vinylalcohol) into gelatin gels resulted in more heterogeneous materials with a 2-fold increase in elasticity (951 Pa to 1993 Pa) and thinner filaments (908 µm to 590 µm). Higher ionic strength in

Laponite-based hydrogels induced nanoparticle aggregation, leading to higher elasticity (857 Pa to 2316 Pa) enabling smooth filament extrusion. Eliminating the often tacitly assumed hydrogel uniformity on the microscale provides additional degrees of freedom to achieve high gel strength without increasing polymer, particle or crosslinker concentration.

4.1 Introduction

Gels are ubiquitous in nature and technology. Hydrogels essentially consist of polymeric networks that retain expressive amount of water [176]. Extensive hydrogel research reports major advances in cell encapsulation [177,178], contact lenses fabrication, drug delivery, wound healing, tissue engineering [179–181], biosensing technologies [182], agricultural applications [183,184], personal care products [76], food products [77], treatment of textile effluent [185], as well as dewatering and separation membranes [78,186].

Mechanical strength is an important design feature for all kinds of hydrogels. This property is directly related to texture perception in food gels [77,187], sensory and organoleptic properties of cosmetics [188], mechanical robustness of filtration membranes [78] and stability of adsorbent gels [189]. In addition, varying degrees of mechanical stiffness in biopolymer gels were found to influence the extra-cellular matrix synthesis of chondrocytes [190], and the differentiation of mesenchymal stem cells [79]. More specifically, mechanical strength can dictate injectability of hydrogels for therapeutic procedures and 3D bioprinting [191,192]. Extrudable hydrogels are a desired class of materials for 3D bioprinting applications, such as cardiac and skin tissue engineering, wound dressing as well as drug screening models [193]. Hydrogels consisting of biopolymers, i.e alginate [79] and gelatin [194], as well as nanoparticles, namely Laponite [195], are often employed as injectable materials. Injectability is characterized by the pressure required for flow as well as extrusion uniformity [196]. Therefore, the viscoelastic properties of both polymeric and particulate networks strongly dictate extrusion success.

The viscoelastic properties of polymeric gels strongly depend on the density of physical and/or chemical crosslinks, on polymer concentration, and hence the mesh size of the polymer network. For hydrogels these parameters are related to the swelling ratio which is controlled, e.g. by solvent quality, pH or ionic strength. Accordingly, various theoretical models have been derived to describe the gel elasticity, taking into account entropic as well as enthalpic contributions to the free energy. Most prominent, different types of polymer networks exhibit different scaling of the shear modulus $G_0 \sim c^{\alpha}$ with polymer concentration. All these models developed to describe the elasticity of (bio)polymer gels and networks have in common that they assume a uniform, homogenous sample composition on length scales larger than the individual molecules or filaments. Besides, commonly applied strategies for enhancing hydrogel elasticity involve increase in polymer/particle concentration, addition of reinforcement, such as particles or fibers, or chemical crosslinkers to polymer matrix as well as polymer matrix manipulation [39,197].

Here a new concept for tailoring the strength of typical extrudable polymeric and particulate hydrogels is presented, which abandons the assumption of uniformity. Targeted introduction of micro-heterogeneities can be used to tailor the mechanical strength of gels in a wide range which is decisive for the performance of such materials in injection, extrusion or 3D printing processes. This work was motivated by earlier investigations on commercial polymeric thickener solutions, which revealed that the thickening efficiency drastically increased for systems showing a heterogeneous structure on a mesoscopic length scale (1-10µm) including predominately viscous and elastic regions. A certain shear modulus level was achieved at an almost ten times lower polymer concentration when compared with other thickeners with similar chemical composition but uniform structure on the mesoscopic scale [91]. Rubinstein proposes that nonlinear elasticity of polymer networks is generated by single polymer chain non-affine deformations and Basu et. al reports on how such deformations in a polyacrylamide gel are caused by network crosslinking inhomogeneity (length scale ~ 200nm) [198,199]. Evidences of mechanical strength control through micro-structural heterogeneity are found by Bansil et al. [200] which, performing particle-tracking

microrheology, found first indications that the elasticity of gastric mucus is related to its heterogeneity in a length scale 500nm - 4μm.

Even in hard sphere suspensions the micro-phase separation into fluid regions of low particle concentration and small densely packed crystals at the entropy driven fluid-crystal phase transition results in a dramatic increase in viscosity and the formation of gel-like viscoelastic response [201]. Flocculated suspensions with their fractal particle network structure often exhibit high shear moduli even at low particle concentration [59]. Capillary suspensions (ternary fluid/fluid/solid systems) with their heterogeneous particle network typically exhibit shear moduli at least one order of magnitude higher than the corresponding binary suspensions [202]. In addition, Laponite nanoclay suspensions constitute thixotropic gels in the presence of electrolyte due to the formation of micro-meter sized nanoparticle aggregates (length scale < 5μm) [203]. However, in Laponite phase diagrams, Laponite gels and glasses are addressed as uniform states and there is no indication in literature of phase separation for Laponite concentration >1wt% and salt concentration lower than 20mM [204].

In this study, four different strategies for inducing micro-phase separation in extrudable hydrogels are presented, namely variation of crosslinking kinetics in a polysaccharide hydrogel, crosslinking of one polymer in a two-polymer mixture, variation of ionic strength in a nanosilicate hydrogel and formation of polysaccharide/nanosilicate composites. At a given polymer/nanoparticle and crosslink density, the hydrogels elastic modulus increases with increasing degree of micro-phase separation. An improved filament at constant extrusion pressure is observed as a direct effect of elasticity enhancement. The self-assembly of heterogeneous, micro-cellular structures results in a superior specific strength of the materials. In analogy to the well-known concepts in construction and engineering mechanics, we term this “statistical micro-scaffolding”.

In this study, Multiple Particle Tracking (MPT) microrheology is employed to investigate microstructural changes and characterize micro-heterogeneity of the hydrogels in the hydrated state on a length scale 0.1-100 μm. Voronoi triangulation and image overlay techniques help direct visualization of spatial micro-heterogeneities formed inside the hydrogels, as demonstrated with the recently introduced Micro-Rheo-Mapping MRM tool [205]. This MPT technique is particularly suitable to visualize and

characterize microscale heterogeneities in highly swollen gels. Unlike other microscopy techniques, MPT takes advantage of strong variations in local viscoelastic properties that often occur even if the local variation of the polymer or particle concentration is too small to generate enough contrast. Classical rotational rheometry as well as uniaxial compression tests were conducted to determine bulk elasticity. 3D printing is employed for injectability and extrusion quality evaluation. A correlation between micro-heterogeneities and their characteristics, such as size and degree of phase separation, and the macro elasticity of hydrogels is stablished, as well as the effects on the extrusion quality, demonstrating that targeted micro-phase separation is a generic design concept to control hydrogels elasticity and hence their injectability, extrudability or 3D printability.

4.2 Materials and Methods

4.2.1 Sample preparation

Sodium alginate (alginic acid sodium salt from brown algae for biochemistry, M_w= 300-350 kg/mol), gelatin extra pure (gold, 180 Bloom), calcium chloride ($CaCl_2$) >98% dehydrated and calcium sulfate ($CaSO_4$) >98% dihydrate were purchased from Carl Roth (Karlsruhe, Germany). Poly(vinyl alcohol) (PVA, Mowiol ® 4-98, Mw ~ 27000 g/mol) was purchased from Sigma- Aldrich Chemie GmbH (Taufkirchen, Germany). Dulbecco's Modified Eagle's Medium (DMEM w: 4.5 g/L Glucose, w: L-Glutamine, w: Sodium pyruvate, w/o: Phenol red, w: 3.7 g/L $NaHCO_3$) was purchased from PAN Biotech (Aidenbach, Germany). D-Glucono-1.5-lacton (GDL) >99% was purchased from Alfa Aesar (Thermo Fisher Scientific, Karlsruhe, Germany). Calcium carbonate ($CaCO_3$, Ulmer Weiss 15H) was purchased from Eduard Merkle GmbH (Blaubeuren-Altental, Germany). Laponite-XLG XR was purchased from BYK-Chemie GmBH (Wesel, Germany).

Salt and polymer solutions were prepared the following way: $CaCl_2$, $CaSO_4$, GDL solutions were prepared stirring the powder with ultrapure Milli-Q water at room temperature and approximately 100 rpm for ten minutes. Using the same procedure, alginate solutions were prepared (with longer stirring time of two hours) for systems I and II.a), but DMEM was used as solvent for system IV (see Table 4.1). DMEM is

frequently employed as solvent in hydrogels used for cell culture as it provides nutrients and physiological conditions for the living cells (salt concentration: 0.2g/L $CaCl_2$, 0.4g/L KCl and 6.4g/L NaCl). Gelatin and PVA solutions were obtained using the same procedure as for alginate solutions, but stirring occurred using DMEM at 40°C and ultrapure water at 90°C, respectively. The $CaCO_3$ suspension was produced stirring the powder with ultrapure water.

Polymer hydrogels were prepared the following way: Alginate hydrogels were made ready by mixing alginate solution with the $CaCl_2$ solution, $CaCO_3$ suspension and GDL in order to solubilize $CaCO_3$ for ten minutes at 100 rpm (system I, see Table 4.1). The molar ratio $CaCO_3$:GDL was always kept 2:1. Two-polymer hydrogels were prepared by mixing PVA with the second polymer solution (gelatin or alginate followed by salt $CaSO_4$) for ten minutes at 100 rpm (system II, see Table 4.1). Hydrogels containing nanoparticle were produced the following way: Laponite nanoparticles were dispersed in ultrapure water with a planetary mixer (Speedmixer, Hauschild GmbH & Co KG, Hamm, Germany) for 10 minutes at 2500rpm. Laponite hydrogels were prepared by mixing Laponite suspensions with salt solutions for 3 minutes at 2500rpm using the planetary mixer (system III, see Table 4.1) and Laponite composites were prepared by mixing alginate solution with the Laponite suspension for 10 minutes at 2500 rpm (system IV, see Table 4.1). All samples in system III presented a pH value of 10, except for 3 wt% Laponite + 3mM $Al_2(SO4)_3$ with pH=7.6. All samples in system IV presented a pH value of 9.5.

Considering the well-known phenomenon of Laponite aging, all measurements were conducted 24 hours after sample preparation for all systems investigated here. Table 4.1 shows the composition details and final weight concentrations of the different ingredients for the investigated systems.

Table 4.1 - Detailed composition of hydrogel systems I-IV.

System	I	II				III	IV
		a		b			
Polymer	1.2% alginate	1.2% alginate	PVA (0-2.8%)	8% gelatin	PVA (0-4%)	-	alginate (0-2%)
Solvent	H_2O	H_2O	H_2O	DMEM	H_2O	-	DMEM
Salt	0.16% ($CaCl_2$ +$CaCO_3$) + GDL	0.16% $CaSO_4$		-		4mM NaCl 15mM (NaCl+KCl) 4mM $CaCl_2$ 3mM $Al_2(SO_4)_3$	-
Nanoparticle	-	-		-		3% Laponite	5% Laponite

4.2.2 Macrorheology: rotational rheometry and uniaxial compression

A rotational rheometer (Rheoscope I, Thermo Fisher Scientific, Karlsruhe, Germany), equipped with a stainless-steel plate-plate measuring cell (diameter 20 mm, gap distance 2 mm) was used to perform small amplitude oscillatory shear experiments at 20°C. Sandpaper was attached to the parallel plates in order to avoid slip. For all gels, frequency sweeps, covering the frequency range from 0.1 to 100 rad.s^{-1}, were performed at a stress amplitude sufficiently small to provide a linear material response. In oscillatory shear, a sinusoidal stress $\tau(t)$ is applied $\tau(t) = \tau_A.\sin\omega t$, where τ_A is the amplitude and ω the angular frequency. The linear response of the strain is given by $\gamma(t) = \gamma_A.\sin(\omega t + \delta)$, where δ is the phase shift angle. The shear stress $\tau(t)$ is proportional to the strain amplitude γ_A and can be represented as $\tau(t) = \gamma_A.(G'(\omega)(\sin(\omega t) + G''(\omega)(\cos(\omega t))$. $G'(\omega)$ is defined as the storage modulus and

$G''(\omega)$ as the loss modulus. The storage and loss modulus are the real and imaginary parts of the complex modulus $G^*(\omega) = G'(\omega) + iG''(\omega)$. The storage modulus represents the storage of elastic energy while the loss modulus indicates the viscous dissipation during strain cycle [59]. For polymer networks, the storage modulus *G'* is almost independent of frequency. Therefore, the bulk shear modulus G_0 is deduced from the value of *G'* at frequency ω = 1 rad.s^{-1}. The plateau modulus G_0 is a key structural parameter for entangled solutions and networks, it is related to the crosslinking density or mesh size of the entanglement network.

Uniaxial unconfined compression tests were performed at 20°C using the commercial tensile testing machine Texture Analyzer TA.XTplus (Stable Micro System, UK) equipped with a 5 kg load cell. Tests were performed on cylindrically shaped gels of 5 mm height and 10 mm diameter. Samples were compressed with a plate (5 cm x 5 cm) at a compression speed of 0.1 mm/s. Young's modulus *E* was determined as the slope of the linear stress-strain curve in the strain region < 40%.

4.2.3 Microrheology: Multiple-particle tracking (MPT)

A detailed scheme of the MPT setup used in this study is described in Kowalczyk et al. [91] It is based on an inverted fluorescence widefield microscope (Axio Observer D1, Carl Zeiss) equipped with a Fluar 100x objective (numerical aperture 1.3, 100x magnification, oil immersion lens, Carl Zeiss). Green fluorescent carboxyl-functionalized polystyrene microspheres of 0.2 µm diameter with density 1.06 g/cm³ and refractive index 1.59 at 589 nm were used as tracer particles (Bangs Laboratories, USA).

The investigated samples including the tracer particles were placed between a microscope glass slide and a coverslip. The microscope was focused roughly halfway into the sample, i.e. at a distance of 20-40 µm away from the surface, to minimize wall effects. 2D images (field of view 127 x 127 µm, frame rate 50 frames/sec) of the fluorescent particles were recorded using a sCMOS camera Zyla X (Andor Technology). Movies of the fluctuating microspheres were analyzed using a custom MPT routine incorporated into the software Image Processing System (Visiometrics iPS). Particle tracking and calculation of mean square displacement (MSD), as well as the statistical

analysis of the trajectories was done using a self-written Matlab® program based on the widely used Crocker and Grier tracking algorithm [91]. Tracer particles were added prior to gelation, to ensure a homogeneous distribution of the tracer particles within the sample. The local viscoelastic modulus *G*(ω)* around a sphere as a function of the frequency *ω* can be determined from Eq. 4.1 [92]:

$$G^*(\omega) = \frac{k_b T}{\pi a i\omega \left\langle \Delta\tilde{r}^2(i\omega) \right\rangle} = G'(\omega) + iG''(\omega) \quad (4.1)$$

with a being the tracer particle radius, k_B the Boltzmann constant, T the temperature and $\langle \Delta\tilde{r}^2(i\omega) \rangle$ the Mean Square Displacement (MSD) of the tracer particles.

Tracers trapped in an elastic network exhibit a time-independent MSD directly related to the apparent local shear modulus (Eq.4.2) of this region:

$$G_{0,MPT} = \frac{2k_B T}{3\pi a \Delta r^2} \quad (4.2)$$

Tracers freely diffusing in a viscous environment exhibit a linearly increasing MSD and the apparent viscosity η_{MPT} of the surrounding fluid is determined using Eq. 4.3 obtained from the Stokes-Einstein relation, and the relation $\langle \Delta r^2(\tau) \rangle = 4D\tau$, where D is the diffusion coefficient related to the MSD $\langle \Delta r^2(\tau) \rangle$ as a function of the lag time τ [93]:

$$\eta_{MPT} = \frac{k_B T}{6\pi a D} \quad (4.3)$$

In this study we investigate heterogeneous systems. MPT allows for the evaluation of heterogeneity in terms of the non-Gaussian parameter *α (alfa)*. Details on the non-Gaussian parameter, which describes the deviation of the MSD values from a Gaussian distribution, are given in the Supplementary Information (Table S1).

4.2.4 Hydrogel extrusion

A pressure-controlled Voxel 8 Developer's Kit 3D printer (Voxel 8 Inc., Harvard, USA), 3CC cartridges (Nordson EFD, Feldkirchen, Germany) and straight needles of

stainless steel, (150 µm outlet diameter, VIEWEG, Germany), were used to extrude the hydrogels in log pile pattern (self-written G-Code). The print head velocity was kept at 600 mm/min for all samples and the extrusion pressure was system dependent, varying from 0.03MPa to 0.4MPa. The extruded constructs were imaged using a Digital Microscope VHX-950F (Keyence, Neu-Isenburg, Germany) and image analysis was performed with the software Image Processing System (Visiometrics iPS).

4.2.5 Statistical analysis

Data are expressed as mean ± SD. Comparisons between two experimental groups were performed using two-tailed t tests with $N \geq 3$ for all groups. Differences were statistically significant for $P < 0.05$.

4.3 Results and Discussion

This investigation employs four different hydrogel systems, each one presenting a different mechanism of inducing phase separation (Table 4.2) on the length scale 1 – 100 µm. MPT microrheology technique is used to characterize these heterogeneities and their effect on bulk elasticity is discussed.

Table 4.2 - Composition and micro-heterogeneity control mechanisms of the systems investigated.

System	I	IIa	IIb	III	IV
Material	Alginate + Ca^{2+} salts	Alginate + PVA	Gelatin + PVA	Laponite + salt	Laponite + alginate
	Variation of crosslinking kinetics		Demixing of micro-	Nanoparticle cluster	Nanoparticle/ polymer

Micro-phase separation mechanism	by varying salt solubility	by adding second polymer	phases triggered via thermal crosslinking of one polymer	formation via variation of ionic strength	cluster formation via addition of polymer

4.3.1 System I – Varying crosslinking kinetics in alginate/calcium salt hydrogels

Physically crosslinked hydrogels are formed when calcium ions interact with alginate guluronate blocks, originating the so-called egg-box model structure [206]. The ionic crosslinking kinetics in alginate gels is determined by the calcium salt solubility in water and therefore by the diffusion rate of the Ca^{2+} ions in the system.

Two Ca^{2+}-salts with very different solubility were used, $CaCl_2$ (solubility of 745 mg/mL at 20 °C), which delivers instantaneous crosslinking and $CaCO_3$ (solubility of 0.02 mg/mL at 20 °C) [207], with a crosslinking time >10 minutes. Alginate (1.2 wt%) as well as the total salt (0.16 wt%) concentrations are kept constant, while the $CaCl_2$:$CaCO_3$ weight ratio is varied.

The heterogeneous microstructure shows up in a broad variation in absolute values and time dependence of the individual MSDs for all gels in this concentration series (as shown in Fig. S1). The ensemble of MSDs is arbitrarily classified in two main populations, as shown exemplarily in Fig.4.1A for $CaCl_2$:$CaCO_3$ ratio 1:1. MSDs with slope < 0.5 (black population in Fig.4.1A) correspond to tracer particles trapped in predominantly elastic regions. Predominantly viscous regions are characterized by tracer particles diffusing freely in the surrounding fluid, corresponding to MSDs with slope > 0.5 (green population in Fig.4.1A).

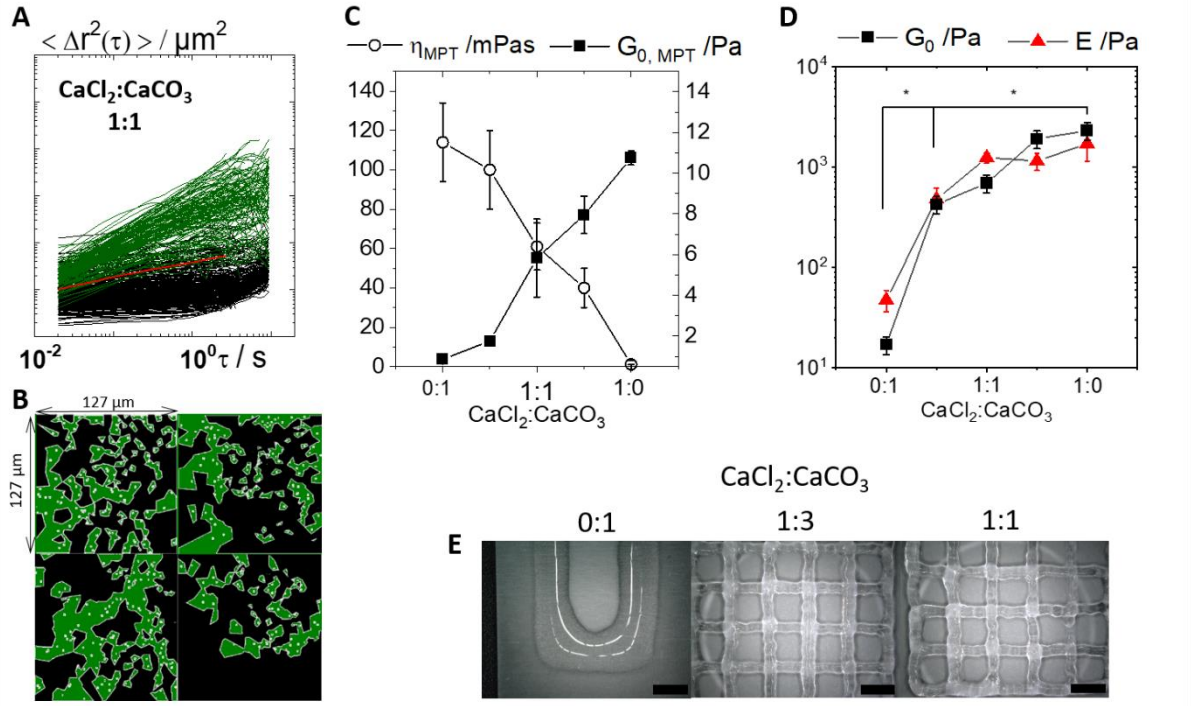

Figure 4.1 - Micro-heterogeneities and rheological characterization of System I. (**A**) Mean square displacement as a function of lag time τ for 1.2 wt% alginate with $CaCl_2$:$CaCO_3$ ratio 1:1. Green and black indicating viscous and elastic MSDs, respectively, and red ensemble average of MSDs. (**B**) Corresponding Voronoi plot as obtained from MPT measurements with tracer particles of diameter 0.2 µm. Four videos were analyzed and one representative MSD diagram is presented. (**C**) Apparent local viscosity η_{MPT} and apparent local elasticity $G_{0,MPT}$ as obtained by MPT measurements and (**D**) bulk shear modulus *G0* and Young's modulus *E* as obtained by shear rheometry and compression tests, respectively, as a function of $CaCl_2$:$CaCO_3$ ratio in 1.2 wt% alginate hydrogel (* indicates P<0.05). (**E**) Extruded alginate hydrogels with $CaCl_2$:$CaCO_3$ ratio 0:1, 1:3 and 1:1. Scale bar = 3mm.

Voronoi triangulation has been used to visualize the heterogeneity of the samples [91], where the black and green areas represent elastic and viscous regions, respectively (see Figure 4.1B for $CaCl_2$:$CaCO_3$ ratio 1:1). Size of the viscous inclusions was estimated by means of Feret's statistical diameter using the public domain processing software ImageJ [208]. Viscous inclusions of size typically 10-20 µm and characteristic viscous area fraction of 10-40% are found (Fig.4.1B).

Increasing the amount of $CaCl_2$ leads to a more pronounced phase separation. This is indicated by the decrease of apparent local viscosity in the viscous regions (green areas in Figure 4.1B) from 115 mPas (corresponding to the viscosity of ~ 1 wt% alginate) to 1mPas (corresponding to the viscosity of water), and on the other side by the increase in the apparent local shear modulus $G_{0,MPT}$ in the elastic regions (black areas in Fig.4.1B) from ~1 to 11Pa (Fig.4.1C). In an alginate hydrogel formed by adding only $CaCO_3$, the slow crosslinking process forms weakly crosslinked regions that coexist with uncrosslinked polymer solution. By partially substituting $CaCO_3$ for $CaCl_2$, the elastic regions become stronger crosslinked as more polymer takes part in this process. The polymer concentration decreases in the uncrosslinked inclusions, hence the viscosity also decreases. This clearly shows that the degree of phase separation and heterogeneity increases with higher fraction of fast crosslinker.

$CaCl_2$ high solubility and therefore high diffusion rate of calcium ions forms dense crosslinked zones that coexist with weak bonding sites or even uncrosslinked polymer as well as salt solution pools [209]. Because of the low solubility of $CaCO_3$, GDL is responsible for the slow dissolution of Ca^{2+} in the system. As the further diffusion rate of ions after the initial binding is also responsible for the degree of heterogeneity [210], a slower crosslinking process leads to weaker micro phase separation, delivering more homogeneous hydrogels [206,211].

The more pronounced micro-phase separation leads to a strong increase of two orders of magnitude in the bulk shear modulus G_0 from 17 to 2300 Pa and in the Young's modulus E from 48 to 1700 Pa (Fig.4.1D). This stunning increment in the bulk elasticity at constant polymer and salt concentration is a consequence of the more pronounced micro-phase separation when the crosslinking process is accelerated due to the addition of a highly water-soluble salt. The bulk elastic modulus values found are much higher than the apparent local elasticity $G_{0,MPT}$. This might be due to densely crosslinked areas which are inaccessible to the tracer particles and therefore do not contribute to $G_{0,MPT}$ [212].

To our knowledge, microscopic dynamics and structure in alginate hydrogels have only been characterized in terms of dynamic light scattering (DLS) [209], revealing the presence of different relaxation modes and these dynamics were associated to the

formation of a hierarchy of crosslinks with different lifetimes indicating a complex structure without, however, providing any spatial information about micro-heterogeneity. This study presents, for the first time, spatial characterization of viscous inclusions in hydrated alginate gels as well as local viscoelastic properties of the micro-phases.

The increase in gel elasticity with a higher fraction of the fast crosslinker ($CaCl_2$) shows improved extrusion results already at $CaCl_2$:$CaCO_3$ ratios 1:3 and 1:1 (Fig.4.1E). Gel with only $CaCO_3$ salt does not have enough cohesive strength for extrusion, thus the filament spreads and does not retain shape. The higher elastic gels due to increased micro-heterogeneity, on the other side, were successfully extruded in continuous and uniform filaments of width 1046±170 µm at 0.17MPa. These results clearly demonstrate that the heterogeneous structure and the degree of phase separation are decisive parameters for controlling the bulk elasticity and extrudability of alginate hydrogels.

4.3.2 System II – Crosslinking of one polymer in a two-polymer mixture

Turning to polymer composites, system II comprises mixtures of alginate/PVA and gelatin/PVA where only alginate and gelatin are crosslinked and PVA remains as solution in the hydrogel.

System II.a) – Variation of alginate crosslinking kinetics by the addition of PVA

As already discussed in the previous section, the addition of Ca^{2+} ions to alginate generates a hydrogel with certain degree of micro-heterogeneity. Adding PVA to a 1.2 wt% alginate solution prior to the addition of 0.16 wt% $CaSO_4$ (solubility of 2.41 mg/mL at 20°C) [207], however, leads to significant modifications of the microstructure (Fig.4.2A-B). Both viscous and elastic phases are present in all systems, but with a distinct disparity in tracer mobility between these regions for the sample without PVA.

When increasing the amount of PVA to 2.8 wt% and keeping the alginate and $CaSO_4$ concentrations constant, the viscosity η_{MPT} within the viscous regions increases from 138 mPas (corresponding to the viscosity of ~ 1 wt% alginate) to 307 mPas (mixed solution of alginate and PVA). Viscous inclusions typically 10 µm in size are found in all samples (Fig.4.2C-D). In presence of PVA, the hydrogel evolves into a more

homogeneous material as fewer viscous inclusions are formed and the average percentage of viscous area is reduced from 12±1% to 3±1%.

The microstructural changes observed in system II.a) can be explained by the interaction of alginate and PVA via hydrogen bonding of hydroxyl groups before addition of $CaSO_4$. Studies with XRD (x-ray diffraction) have shown that, as the quantity of alginate in a PVA/alginate blend nanofibers is increased, the intensity of the diffraction peak of PVA becomes lower and broader [213,214]. The reduction of the crystallinity of the electrospun PVA/alginate nanofibers can probably be attributed to the hydrogen-bonding interaction between alginate and PVA macromolecules. Besides, FTIR (Fourier-transform infrared spectroscopy) results have shown that, with the addition of alginate, the intensity of absorption peaks of PVA decrease, and some peaks disappear, suggesting an interaction between PVA and alginate [213,214]. It was also observed that the bands of hydroxyl stretching become much broader with adding alginate, which supports the idea that hydrogen bonding could be formed between alginate and PVA hydroxyl groups. Moreover, the fact that PVA molecular chain contains highly polar functional groups (hydroxyl) facilitates intermolecular interaction in the form of hydrogen bonding between PVA and alginate, resulting in a denser system [215].

On account of this, alginate crosslinking with Ca^{2+} ions is delayed and a more homogeneous hydrogel with lower degree of micro-phase separation is formed when PVA is introduced. As discussed previously, a slower crosslinking kinetics produces more homogeneous alginate hydrogels.

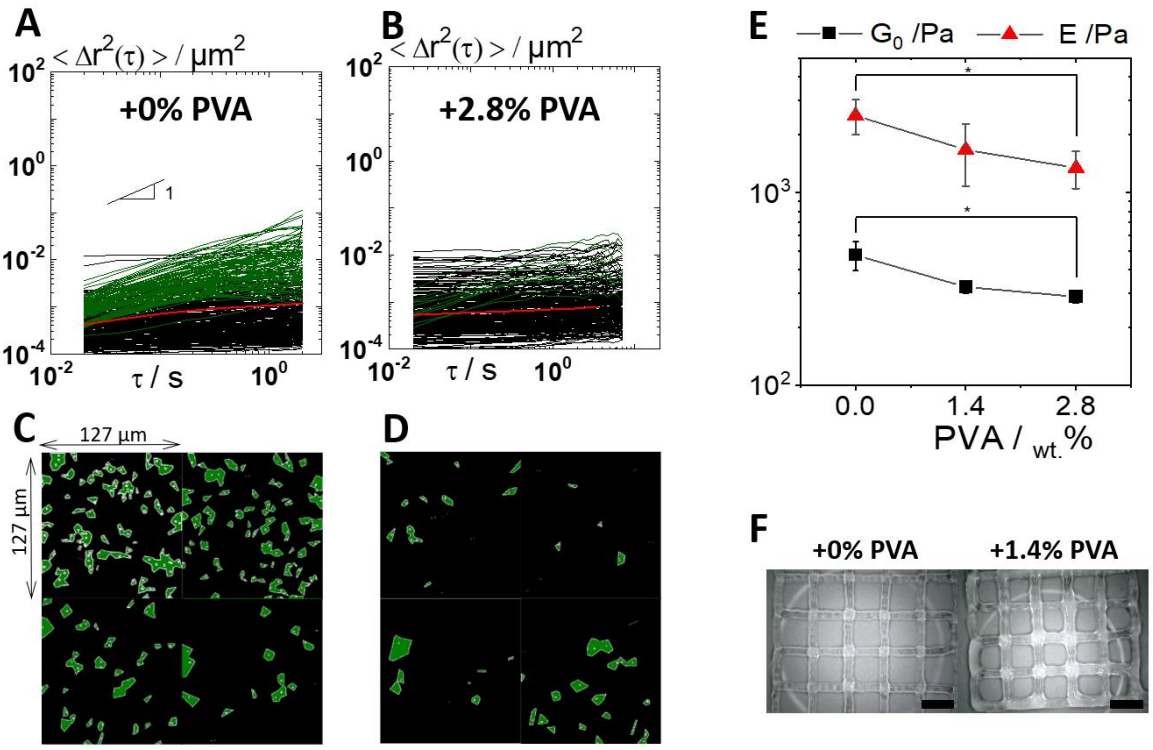

Figure 4.2 - Micro-heterogeneities and rheological characterization of System II.a). (**A**)-(**B**) Mean square displacement as a function of lag time τ for 1.2 wt% alginate and 1.2 wt% alginate + 2.8 wt% PVA. Green indicating viscous MSD, black elastic MSD and red ensemble average of MSDs. (**C**)-(**D**) Corresponding Voronoi plots as obtained from MPT measurements with tracer particles of diameter 0.2µm. Viscous area fraction decreases in the alginate hydrogel as more PVA is present. For each concentration, four videos were analyzed and one representative MSD diagram is presented. (**E**) Bulk shear modulus G_0 as obtained by shear rheometry and Young's modulus E as obtained by compression tests as a function of PVA concentration in 1.2 wt% alginate + 0.16 wt% $CaSO_4$ hydrogel (* indicates $P<0.05$). (**F**) Extruded alginate hydrogels with 0% and 1.4%PVA. Scale bar = 3mm.

As a result of a lower micro-phase separation degree, a decrease in the macro-elasticity is observed (Fig.4.2E). Both G_0 and E drop almost by a factor of 2 in presence of PVA. This is consistent with what was already observed for pure alginate gels, again a more heterogeneous microstructure leads to higher bulk elasticity at constant polymer concentration. The concentration of the polymer that actively participates in the crosslinking process and contributes to the elasticity, i.e. alginate, is kept constant while only PVA concentration is increased. An aqueous 2.8 wt% PVA solution, however,

presents a viscosity lower than 4mPas, which clearly excludes any PVA entanglement contribution to the hydrogel elasticity. The change in micro-heterogeneity is the only source for the observed change in the gel's bulk elasticity.

The elasticity decrease in gels with PVA directly affects extrusion quality (Fig.4.2F). With the addition of 1.4% PVA to alginate gel, filament width increased from 676±90 µm to 857±171 µm when extruded at 0.17MPa.

System II.b) Demixing of gelatin/PVA micro-phases via thermal crosslinking of gelatin matrix

PVA is now incorporated into gelatin, which forms a physically crosslinked hydrogel via thermal gelation. Gelatin concentration is kept constant (8 wt%) while PVA solution concentration is increased from 0 to 4 wt%. Overlay plots created from 500 subsequent images taken from MPT video sequences (Fig.4.3A-B) clearly reveal that a heterogeneous micro-structure results from the addition of PVA to gelatin [83].

A uniform particle distribution occurs in pure gelatin sample (Fig.4.3A), while inclusions depleted of tracer particles are found in the samples with PVA (Fig.4.3B). The size of these inclusions increases from 7.5±3 µm at 2 wt% PVA content (Figure S2) to 15±10 µm at 4 wt% PVA (Fig.4.3B). At the same time, the area fraction of these inclusions in the hydrogel increased from 12% to 28%. All tracers are embedded in an elastic gel-like environment provided by the gelatin gel (Fig.4.3C).

In order to characterize the void spaces, tracer particles were directly injected into the inclusions with a syringe (Fig.4.3D). As shown exemplarily in Fig.4.3E for sample 8 wt% gelatin + 4 wt% PVA, the tracer particles diffuse freely, indicating that these inclusions are presumably formed of aqueous PVA solution that demixed from the gelatin gel during the thermal crosslinking process. Samples with 2 wt% and 4 wt% PVA presented local apparent viscosity η_{MPT} in these pore shaped inclusions of 23mPas and 35mPas, respectively, corresponding to the viscosity of approximately 6 wt% and 7 wt% PVA.

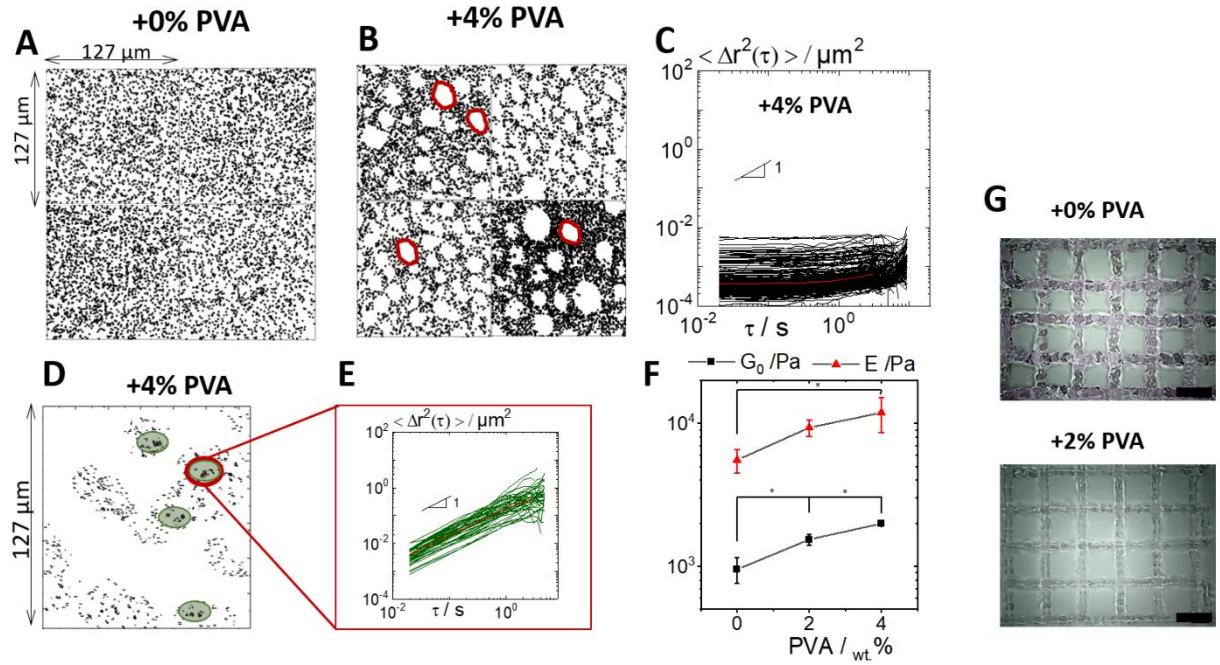

Figure 4.3 - Micro-heterogeneities and rheological characterization of System II.b). **(A)-(B)** Overlay plots for 8 wt% gelatin and 8 wt% gelatin + 4%$_{wt.}$PVA (four videos were analyzed for each concentration), some viscous inclusions are indicated in red, (**C**) representative MSDs of elastic trajectories as a function of lag time for 8 wt% gelatin + 4 wt% PVA, (**D**) overlay plot for tracer particles directly injected in viscous inclusions (green area), (**E**) representative MSDs of viscous trajectories for sample with 4 wt% PVA, as obtained by MPT measurements and (**F**) bulk shear modulus G_0 as obtained by shear rheometry and Young's modulus E as obtained by compression tests as a function of PVA concentration in 8 wt% gelatin hydrogel (* indicates $P<0.05$). (**G**) Extruded gelatin hydrogels with 0% and 2% PVA. Scale bar = 3mm.

This higher PVA content in the pores is a result of micro-phases demixing. Liquid-liquid as well as solid-liquid separation depend strongly on the concentration of the components and on the environmental stimuli, such as temperature or pH [216,217]. Crosslinking of one polymer in a mixture can induce micro-phase separation, as only one component is sensitive to the environmental stimuli or crosslinking reaction and the whole mixture becomes unstable. This method can be employed for producing controlled micro-structured materials based on the kinetics of demixing [217].

In our study, gelatin and PVA (as well as tracer particles) were well mixed in the aqueous solution at 40°C. By lowering the temperature, gelatin begins to thermally

crosslink and the demixing process of gelatin network and PVA solution is triggered. By the time room temperature is reached (20°C) further phase separation is ceased. At this point, the gelatin elastic network is stabilized along with the tracer particles, which were arrested in the elastic phase during demixing, and PVA is found dispersed in discrete pore shaped viscous inclusions.

The micro-heterogeneities formed due to the addition of PVA to the system lead to an increase in the bulk elasticity of a factor of 2 for both G_0 and E (Fig.4.3F)), even though the amount of polymer actively participating in the crosslinking process and therefore network formation, i.e. gelatin, is kept constant at 8 wt%. A 4 wt% aqueous PVA solution presents a viscosity ≈5 mPas, clearly excluding entanglement effects on the hydrogel overall elasticity. The micro-phases separation resulted in the formation of elastic regions with higher gelatin crosslinking density than in the pure gelatin gel and of viscous inclusions consisting of PVA with a higher viscosity in comparison to the mixture before demixing. This micro-phase demixing phenomenon is responsible for the increase in the overall hydrogel bulk elasticity.

Improved extruded filaments are obtained for the hydrogel with 2% PVA (590±76 µm line width) in comparison to pure gelatin (908±118 µm line width) at a constant extrusion pressure of 0.4MPa (Fig.4.3G). The extrusion of thinner filaments, i.e. less spreading at the same pressure value is directly related to the higher elasticity at constant gelatin concentration.

4.3.3 System III – Varying ionic strength in Laponite hydrogels

Clay suspensions exhibit complex phase behavior depending on clay concentration, pH and ionic strength. For Laponite suspensions this has been extensively discussed e.g. in Ruzicka & Zaccarelli [204]. At pH < 11, Laponite platelets are negatively charged on their faces, but positively charged at the edges. In the absence of salt, an extended electrical double layer is formed around the particles in suspension and repulsive forces dominate. Addition of electrolyte to Laponite suspensions induces a contraction of the electrical double layer and attractive forces become relevant [96,218], leading to modifications in the microstructure.

For system III investigated here, Laponite suspensions ionic strength $I = 0.5\sum_{i=1}^{n} c_i z_i^2$, where c_i is ion concentration and z_i is the ion charge, was varied by the addition of salts with increasing concentration or cation valence. Tracer particles were homogeneously distributed in a salt free 3 wt% Laponite suspension, as shown in Fig.4.4A. By adding 4 mM monovalent salt NaCl to 3 wt% Laponite suspension, almost no changes occur (data not shown). By increasing the concentration of monovalent salt from 4 to 15 mM however, large white areas where no tracer particles are present appear (Fig.4.4B). Similar changes in the microstructure occur when divalent and trivalent cation salts, $CaCl_2$ and $Al_2(SO_4)_3$ respectively, are incorporated into 3 wt% Laponite suspension (Fig.4.4C-D).

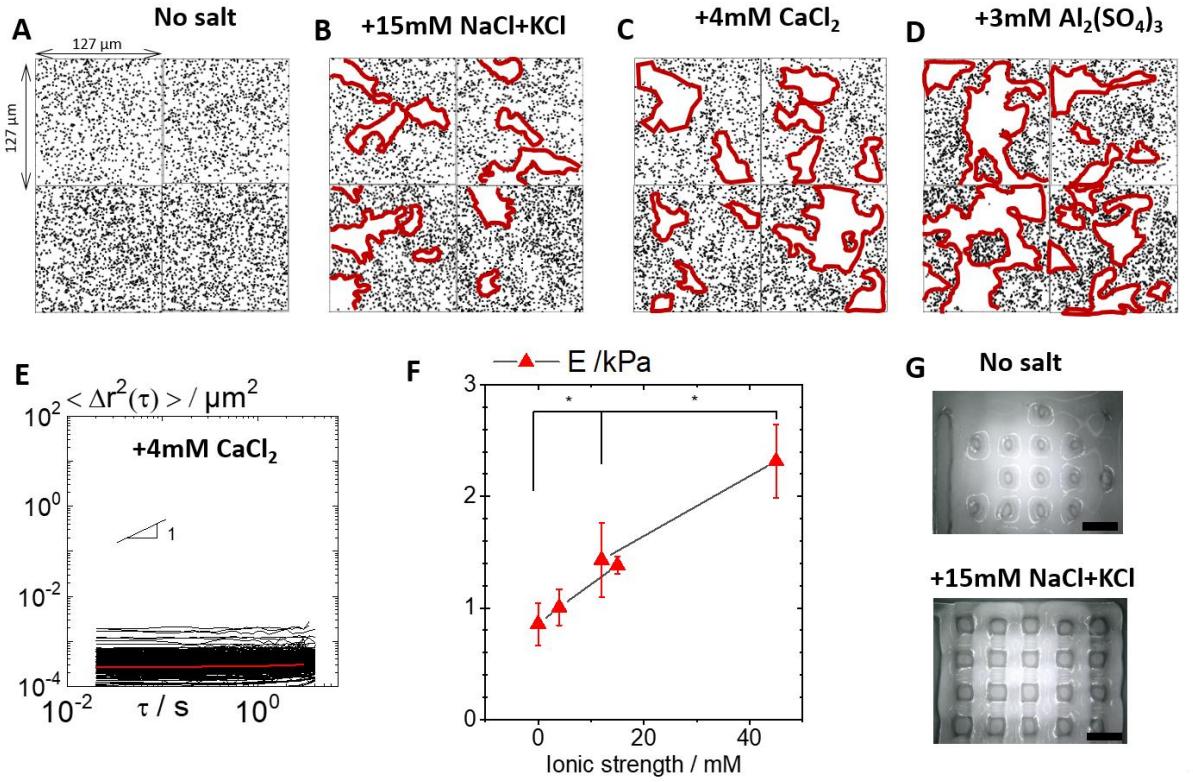

Figure 4.4 - Micro-heterogeneities and mechanical characterization of System III. **(A)-(D)** Overlay plots for pure 3 wt% Laponite XLG hydrogel and 3 wt% Laponite XLG hydrogel in the presence of salt with increasing ionic strength, clusters are indicated in red and (**E**) representative MSDs of elastic trajectories for 3 wt% Laponite + 4mM $CaCl_2$, as obtained by MPT measurements. For each formulation, four videos were analyzed and one representative MSD diagram is presented. (**F**) Young's modulus *E* as obtained

by compression tests and ionic strength values for pure 3 wt% Laponite hydrogel and 3 wt% Laponite hydrogel in the presence of salt with increasing ionic strength (* indicates $P<0.05$). All samples in system III presented a pH value of 10, except for 3 wt% Laponite + 3mM $Al_2(SO4)_3$ with pH=7.6. (**G**) Extruded laponite hydrogels without salt and with 15mM NaCl+KCl. Scale bar = 3mm.

Densely packed areas inaccessible for the 200nm tracer particles are formed at ionic strength $\geq$ 15mM and/or when multivalent ions are added. This is due to short-range attraction among particles resulting from van der Waals interactions and different charge densities on the rims and faces of Laponite platelets [218,219]. The length scale of the inaccessible areas was found to be 20-100 µm and the average inaccessible area fraction in the hydrogel increased from 17±5% (15 mM NaCl+KCl) to 37±22% (3mM $Al_2(SO_4)_3$) by increasing the salt cation valence. Such heterogeneous microstructures in Laponite suspensions have been suspected earlier based on dynamic light scattering and active micro rheology experiments [218]. Here, the size and shape of microstructure were visualized for the first time enabled by overlay plots of image series taken from MPT video sequences [83].

The tracer particles embedded in 3% Laponite gels sense only elastic microenvironment, as indicated by time independent MSDs exemplarily shown in Figure 4.4E for 3wt% Laponite + 4mM $CaCl_2$. Similar results were obtained for all other systems investigated in this series (Fig. S3).

The increase in the ionic strength to values I > 10 mM accompanied by an enhanced micro-phases separation leads to a drastic growth in the bulk elasticity of the hydrogel at constant nanoclay concentration (Fig.4.4F). For $3_{wt.}$% Laponite with no salt, E increase from 860 Pa to 2315 Pa with the addition of 3mM of trivalent salt. Changes in the macroelasticity of Laponite hydrogels when increasing ionic strength were reported in the literature and associated to aggregate formation based on DLS and small-angle X-ray scattering (SAXS) experiments [220,221]. In our investigation, it was shown for the first time that a micro-phase separation on a length scale 10-100µm is related to the strong increase in bulk elasticity upon increasing ionic strength.

Pure Laponite hydrogel did not form filaments when extruded, as the gel was not strong enough to retain shape (Fig.4.4G). The addition of 0.15mM of monovalent salt increased gel elasticity and allowed uniform extrusion of 1324±137 µm wide filaments at 0.03 MPa without increasing nanoparticle concentration.

4.3.4 System IV – Cluster formation in Laponite/alginate composites

Microstructural alterations in Laponite based hydrogels may occur not only upon variation of ionic strength but also by adding polymers. Micro-heterogeneities were formed and tracer particles were no longer found homogeneously distributed when 1 wt% alginate in DMEM was added to a 5 wt% Laponite hydrogel (Fig.4.5A-B). Densely packed regions typically 20-40 µm in diameter and depleted of tracer particles are found presumably consisting of mixed Laponite alginate aggregates.

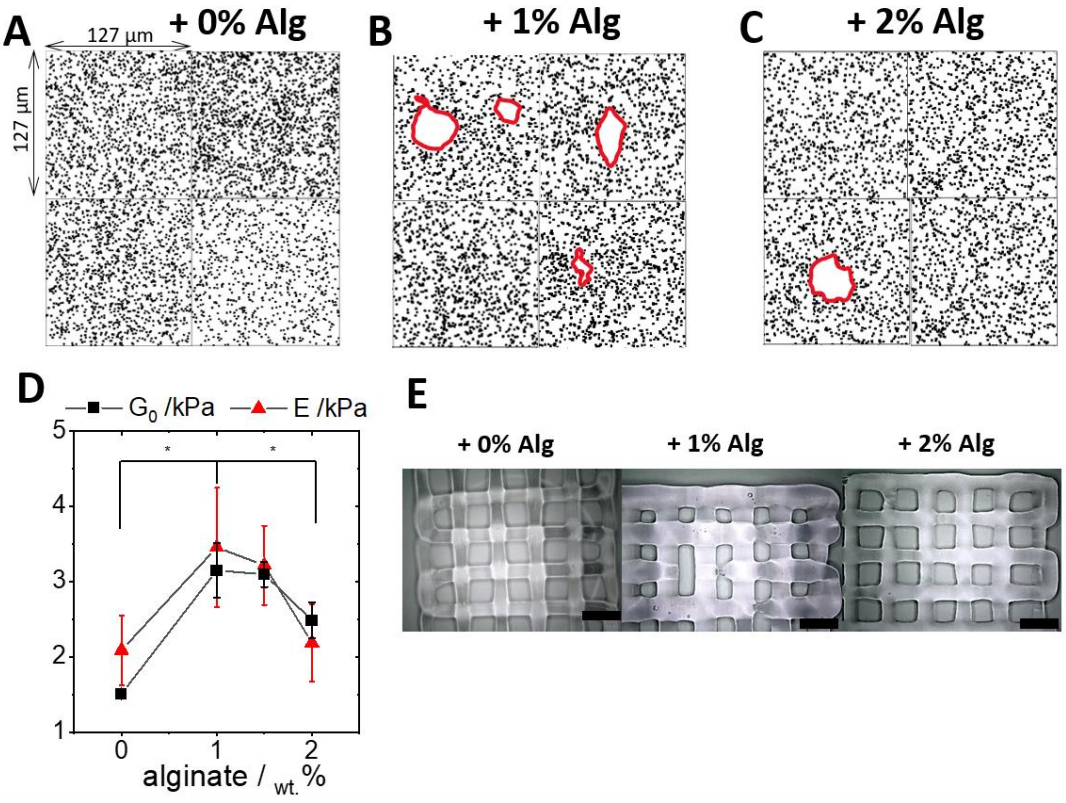

Figure 4.5 - Micro-heterogeneities and mechanical characterization of System IV**. (A-C**): Overlay plots for pure 5 wt% Laponite XLG hydrogel and 5 wt% Laponite XLG hydrogel with alginate, clusters are indicated in red (four videos were analyzed for each

concentration) and (**D**) bulk shear modulus G_0 and Young's modulus E as obtained by shear rheometry and compression tests, respectively, as a function of alginate concentration in 5 wt% Laponite in DMEM hydrogel (* indicates $P<0.05$). All samples in system IV presented a pH value of 9.5. (**E**) Extruded Laponite hydrogels with 0%, 1% and 2% alginate. Scale bar = 3mm.

By further increasing alginate concentration up to 2 wt% (Fig.4.5C) and keeping Laponite concentration constant, the frequency of clusters decreases and the hydrogel becomes more homogeneous again. When Laponite particles interact with polymer chains dissolved in solvent containing electroctrolyte, such as DMEM, compact clusters of nanoclay and polymer are formed [221,222]. However, when increasing the amount of alginate but keeping electrolyte concentration constant, hydrogen bonding as well as electrostatic interactions between Laponite particles and alginate chains hinder nanoparticle cluster formation, thus leading to a more homogeneous hydrogel [223]. Similar to system III, MSD of all tracers in system IV are time independent (data not shown).

The formation of micro-heterogeneities upon addition of 1wt% alginate is accompanied by a sharp rise in the bulk elasticity, followed by gradual decline in G_0 and E as the fraction of dense aggregates decreases when the alginate concentration is further increased (Fig.4.5D). It should be noted that alginate is not crosslinked in the system, so it does not contribute to the elasticity by creating an elastic polymeric network but by inducing aggregate formation and micro-phase separation with Laponite in the presence of electrolyte. The non-monotonic variation of bulk elasticity can be directly related to the degree of micro-heterogeneity in this sample series. This further confirms the hypothesis that targeted micro-phase separation is a powerful tool to control bulk elasticity of composite gels. It is worth noting that in Systems I and IV, G_0 and E show very similar values, while in System II, $E > G_0$. For ideal uniform, isotropic bodies, $E=3G_0$. However, the systems investigated here are not ideal uniform and isotropic, so this relation may vary depending on the structural features of the micro-heterogeneities. Besides, these differences in G_0 and E might be explained by the diverse deformation processes polymer chains undergo depending on the hydrogel loading mode. The different microstructural deformations in a hydrogel under shear and under compression might result in different macro mechanical properties. Knapp describes distinct G_0 and

E values for collagen hydrogels due to distinct reactions of collagen fibrils upon deformation by shear and by compression [224].

The increase in elasticity in system IV via addition of 1wt% alginate solution to Laponite gels did not improve filament extrusion (Fig.4.5E). The amount and size of the nanoclay/polymer clusters might impair filament uniformity and continuous extrusion. This effect was not studied here, and further investigations will be performed to characterize impact of micro-heterogeneity characteristics on 3D printing performance in more detail. The further decrease in elasticity with addition of 2wt% alginate to Laponite produced continuous filaments of 1253±186 µm width at 0.4MPa in comparison to 789±40 µm for pure Laponite at 0.07MPa.

Even though no improvement in the extrusion quality was observed with the addition of alginate to Laponite, the hydrogel remained injectable with continuous filament extrusion. Nanoclay/polymer composites are of interest for biomedical application where the presence of both polymeric and particulate materials influence cell behavior.

4.3.5 Statistical micro-scaffolding design concept

It is demonstrated that targeted micro-phase separation is a generic design concept to control the elasticity of extrudable hydrogels. Several strategies are presented for introducing micro-heterogeneities in a hydrogel matrix via micro-phase separation which resulted in an increase in gel elasticity at a given polymer or particle concentration. The increase in gel strength happens regardless of the heterogeneity state of matter. These micro-heterogeneities can appear as viscous inclusions in the gel matrix, as demonstrated in System I, with inclusions formed of uncrosslinked alginate and salt solutions, and in System II, where inclusions of PVA solution phase separated from the gelatin gel during thermal crosslinking. Strategies where solid micro-heterogeneities were formed are presented in System III, with nanoparticle aggregates and in System IV with aggregates constituted of Laponite and alginate.

This novel design concept, does not require polymer chain modification, reinforcement or chemical crosslinker addition to increase hydrogel strength. The concept was applied to a broad variety of different hydrogel systems, showing that this

generic approach can be widely employed for designing polymer and particulate hydrogels, even a transfer to organogels seems to be straightforward. The specific strategy for inducing micro-heterogeneities depends on the system composition, as demonstrated in this study. Different material compositions will have particular requirements for triggering micro-phase separation in order to reach a micro-heterogeneity intensity relevant for strength enhancement. Polymer or particle concentration might also dictate the characteristic features of achievable micro-heterogeneities. Thorough understanding of how the hydrogel components interact with each other is the basis for a targeted and efficient micro-phase separation leading to an increase in elasticity. If these specific boundary conditions are known, a transfer of the design concept to other systems not investigated here should be straight forward.

Regarding the thermodynamics of micro-phase separation, the process is determined by the interfacial free-energy, which is mainly influenced by the interfacial area [225]. Micro-phase separation has been reported to occur in hydrogels when thermo-sensitive polymer segments become hydrophobic at temperatures higher than the critic temperature $T > T_c$ and separate from hydrophilic segments, which have more affinity with water molecules. These thermo-sensitive segments which became hydrophobic form local micellization, shrinking while separating from the hydrophilic phase. This local shrinkage and overall deswelling results in increase in the bulk hydrogel elasticity. The hydrogel obeys the rubber elasticity rule, as the thermoresponsive segments are hydrophilic when $T < T_C$ and the swelling is more pronounced. When $T > T_C$, the local shrinkage due to micro-phase separation causes the increase of the elastic modulus. As reported for a PNIPAm/PDMA (poly(N-isopropylacrylamide)/poly(N,N-dimethylacrylamide)) hydrogel, a further increase in temperature enhances the degree of micro-phase separation and the elasticity is increased significantly due to shrinkage of the thermoresponsive PNIPAm segments [225]. In this case, however, the length scale (<100nm) and the underlying physical mechanism of phase separation are different from the systems investigated here.

For the extrudable hydrogels studied here, micro-heterogeneity formation and the corresponding elasticity increase improved dispensing or extrusion quality at constant printing conditions. The increase in elasticity enabled extrusion of uniform filaments with

high shape fidelity in systems I and III, while thinner lines could be printed in system II. An elasticity enhancement via conventional ways, such as increasing the crosslink density or adding reinforcement fillers usually leads to an increase in the extrusion pressure necessary for printing uniform filaments. Finally, the length scale of the introduced heterogeneities was kept small (1-100 µm) compared to the extrude filament diameter (>500 µm). This is mandatory to ensure high printing quality in terms of filament uniformity and shape fidelity.

The statistical micro-scaffolding design concept is relevant to hydrogel design applications such as 3D bioprinting, tissue engineering, wound dressing or drug screening, where extrudability is desired or required but high compressive or shear stresses could be detrimental. Furthermore, this design concept may have implications for various applications where both mechanical strength and heterogeneity of the hydrogel are important, e.g. in texture, sensory and organoleptic properties perception, mechanical robustness of filtration and adsorbent gels, or in the differentiation of stem cells embedded in hydrogels with varying degrees of stiffness.

4.4 Conclusion

A new generic design rule is presented, that allows the mechanical strength of polymeric and particulate extrudable gels to be adjusted based on the formation of heterogeneities on the length scale 1-100µm. This concept abandons the assumption of uniform sample composition tacitly assumed in essentially all theories referring to the viscoelastic behavior of gels, and offers additional degrees of freedom for enhancing mechanical gel strength without increasing polymer / particle concentration or average crosslink density. In this study, different polymeric and particulate model systems were used to demonstrate the feasibility of the strategy and the impact on extrudability.

Micro-mechanical and structural heterogeneity was enhanced in alginate hydrogels by accelerating crosslinking kinetics, generating higher elastic materials (17 Pa to 2300 Pa) with substantially improved filament extrudability and shape fidelity (1046±170 µm wide filaments). Adding PVA prevented alginate crosslinking and produced softer (475 Pa to 289 Pa), more homogeneous hydrogels, with larger extruded

filament width. Introducing PVA into gelatin gels resulted in more heterogeneous materials with higher elasticity (951 Pa to 1993 Pa) and therefore thinner extruded lines (908±118 μm to 590±76 μm) due to micro-phase separation. Higher ionic strength in Laponite-based hydrogels induced nanoparticle aggregation, producing materials of higher elasticity (857 Pa to 2316 Pa) and superior extrusion quality (1324±137 μm wide filaments). Further addition of alginate prevented cluster formation due to nanoparticle-polysaccharide interactions, resulting in more homogeneous, softer materials with larger filament spreading (789±40 μm to 1253±186 μm).

These findings provide deeper insight into complex hydrogel micro-structures in the hydrated state and expand our capabilities to control bulk mechanical gel properties. With the design concept developed in this study, increase in gel elasticity and improvement in filament extrusion are possible maintaining constant extrusion conditions. The length scale of the heterogeneity, however, was kept much smaller (1-100 μm) than the extrude filament diameter (>500 μm) in order to ensure uniform, interruption-free extrusion. Further investigations should be carried on the impact of micro-heterogeneity size, type and volume fraction on the shape fidelity and uniformity of extruded hydrogel filaments and how this depends on specific system properties.

In addition, this design model may have implications in several applications in which hydrogel mechanical strength as well as heterogeneity are relevant, namely food and cosmetic gels, as well as hydrogels used for tissue engineering and bioprinting.

Triggered self-assembly into a "statistical microcellular" structure is a generic design strategy that can be used to tune the elasticity of gels over a wide range. Following the well-known design scheme from engineering mechanics, it is referred to here as the statistical micro-scaffolding concept.

Publication IV

5 Targeted micro-heterogeneity in bioinks allow for 3D printing of complex constructs with excellent resolution and high cell viability

Full title: Targeted micro-heterogeneity in bioinks allow for 3D printing of complex constructs with improved resolution and cell viability.

Authors: Bruna Regina Maciel, Alisa Grimm, Claude Oelschlaeger, Ute Schepers and Norbert Willenbacher

Status: Published.

B. R. Maciel, A. Grimm, C. Oelschlaeger, U. Schepers, N. Willenbacher. Targeted micro-heterogeneity in bioinks allow for 3D printing of complex constructs with improved resolution and cell viability. *Biofabrication* (2023) 15, 045013

https://doi.org/10.1088/1758-5090/acee22

Abstract

3D bioprinting is an evolving versatile technique for biomedical applications. Ideal bioinks have complex micro-environment that mimic human tissue, allow for good printing quality and provide high cell viability after printing. Here we present two strategies for enhancing gelatin-based bioinks heterogeneity on a 1-100µm length scale resulting in superior printing quality and high cell viability. A thorough spatial and micro-mechanical characterization of swollen hydrogel heterogeneity was done using Multiple Particle Tracking microrheology. When poly(vinyl alcohol) is added to homogeneous gelatin gels, viscous inclusions are formed due to micro-phase separation. This phenomenon leads to pronounced slip and superior printing quality of complex 3D constructs as well as high HepG2 and NHDF cell viability due to reduced shear damage during extrusion. Similar printability and cell viability results are obtained with gelatin/nanoclay composites. The formation of polymer/nanoclay clusters reduces the critical stress of gel fracture, which facilitates extrusion, thus enhancing printing quality and cell viability. Targeted introduction of micro-heterogeneities in bioinks through

micro-phase separation is an effective technique for high resolution 3D printing of complex constructs with high cell viability. The size of the heterogeneities, however, has to be substantially smaller than the desired feature size in order to achieve good printing quality.

5.1 Introduction

3D bioprinting offers a vast array of possibilities for biomedical applications. In this versatile biofabrication process, living cells can be deposited in specific positions in a 3D construct with desired geometry. In comparison to other methods, extrusion based bioprinting (EBB) is the most used technique due to low cost, ease of use and a broader range of hydrogel materials available to be used as bioink [25]. Hydrogels for tissue engineering applications often consist of mixtures of biopolymers such as gelatin, alginate, chitosan or gellan gum with synthetic polymers, poly(vinyl alcohol) (PVA), polyacrylate hydrogels or poly(ethylene glycol) (PEG) for instance, in order to improve mechanical properties or biocompatibility [154,226,227]. More specifically, mixtures of gelatin with PVA have been described as promising composites for cell culture scaffolds [228,229] and tissue regeneration [230]. Many of these composite materials and hydrogels have been valued for their low stiffness and large pore size, which is a key requisite for tissue engineering. However, many other applications such as hydrogel drug delivery or bone reconstruction require much more constrained mechanical properties. A method to enhance these properties is nanoparticle reinforcement [42,231]. Nanosilicate composites, such as mixtures of biopolymers with Laponite® clay nanoparticles, have been widely investigated for tissue engineering constructs due to its biocompatibility and degradation in nontoxic products [41,195,232,233].

One crucial requirement for EBB is finding bioink materials that allow for high printing quality, i.e. high resolution and good mechanical stability of the printed construct while providing high biocompatibility and cell viability despite significant shear stresses that may be present during bioprinting [234,235]. 3D printing of complex structures has been described using the FRESH technology with collagen bio-inks and support materials that can be melted away [45] or using the NICE technique to print GelMA, kappa-carrageena and nanosilicates by increasing the printing temperature to 37°C [46].

However, there is a lack of bioink materials that allow room temperature printing of self-standing structures with high cell viability.

Another important aspect in the search for bioink materials is the need of more complex and heterogeneous engineered hydrogel composites in order to mimic the native human tissue microenvironment [53,80,234,236]. Moreover, a lack of control over micro-heterogeneity formation in hydrogels and shortage of adequate methods for characterizing microstructural heterogeneity in the hydrated state is also a challenge to be overcome. Limitations on the use of currently available imaging methods for hydrogel microstructure characterization have been reported in the literature [57,73,82]. Sample processing such as drying and coating with conductive material which is normally required for scanning electron microscopy (SEM), or the need of a contrast agent as in X-ray microtomography (μCT), leads to difficulties in resolution, limited depth penetration, artefact production or even destruction of the original 3D hydrogel microstructure, generating inaccurate results. Multiple Particle Tracking (MPT) technique, a micro-rheology method, is an effective tool for microstructural and local flow behavior characterization, especially in cases where other microscopy methods fail. This technique has been employed for viscoelastic and microstructural characterization of food emulsions and gels [237]. To our knowledge so far, there are a few published data on visualization of biocompatible hydrogels micro-heterogeneities using MPT [73,74,238,239].

In this study, we present two strategies for inducing micro-heterogeneity formation in gelatin based bioinks for EBB. The first strategy is the addition of a polymer solution (PVA) to a homogeneous gelatin hydrogel and the second is the incorporation of clay nanoparticles (Laponite) into gelatin gels. The multiple particle tracking (MPT) technique was employed to get new insight into the microstructural and micromechanical properties of hydrogels in the hydrated state. Heterogeneity formation via different mechanisms of micro-phase separation on the length scale 1-100 μm was characterized and its impact on the bulk elasticity, printability and cell viability was carefully analyzed. Finally, moderately heterogeneous hydrogels allowed 3D printing of self-standing complex constructs at room temperature without a support bath and provided high cell viability after 7 days of cell culture.

5.2 Experimental Section

5.2.1 Hydrogel preparation

Gelatin extra pure (gold, 180 Bloom) was purchased from Carl Roth (Karlsruhe, Germany). Poly(vinyl alcohol) (PVA, Mowiol ® 4-98, M_w ~ 27000 g/mol) was purchased from Sigma- Aldrich Chemie GmbH (Taufkirchen, Germany). Dulbecco's Modified Eagle's Medium (DMEM w: 4.5 g/L Glucose, w: L-Glutamine, w: Sodium pyruvate, w/o: Phenol red, w: 3.7 g/L $NaHCO_3$) was purchased from PAN Biotech (Aidenbach, Germany). Laponite-XLG XR was purchased from BYK-Chemie GmBH (Wesel, Germany). Gelatin and PVA solutions were obtained stirring the powder with DMEM at 40°C and ultrapure water at 90°C, respectively, at approximately 100 rpm for ten minutes. Two-polymer hydrogels were prepared by mixing the PVA solution with the gelatin solution at desired concentrations with the ratio gelatin solution:PVA solution 8:2 for ten minutes at 100 rpm. Hydrogels containing nanoparticle were produced the following way: Laponite XLG nanoparticles were dispersed in ultrapure water with a planetary mixer (Speedmixer, Hauschild GmbH & Co KG, Hamm, Germany) for 10 minutes at 2500 rpm. Laponite composites were prepared by mixing gelatin solution with the Laponite suspension with the ratio gelatin solution:Laponite suspension 8:2 for 10 minutes at 2500 rpm. Gelatin/Laponite mixtures presented pH value of 8.

All measurements were conducted 24 hours after sample preparation for all systems investigated here. Table 5.1 shows the composition details and final weight concentrations of the different ingredients for the investigated systems:

Table 5.1 – Detailed composition of the gelatin-based hydrogels

Hydrogel	Gelatin	PVA	Laponite
6G	6%	-	-
6G2P	6%	2%	-
6G4P	6%	4%	-
6G0.2L	6%	-	0.2%
6G0.4L	6%	-	0.4%
8G2P	8%	2%	-
8G4P	8%	4%	-

5.2.2 Macrorheology

Rotational rheometry: A rotational rheometer (Rheoscope I, Thermo Fisher Scientific, Karlsruhe, Germany), equipped with a stainless-steel plate-plate measuring cell (diameter 20 mm, gap distance 2 mm) was used to perform small amplitude oscillatory shear experiments at 20°C. Sandpaper was attached to the parallel plates in order to avoid slip. For all gels, frequency sweeps, covering the frequency range from 0.1 to 100 rad/s, were performed at a stress amplitude sufficiently small to provide a linear material response. These modulus curves confirmed that the storage modulus *G'* was essentially frequency independent and its value at frequency ω= 1 rad.s^{-1} was determined as the bulk shear modulus G_0 of the investigated gel. Shear stress ramps were applied to assess the slip behavior with smooth plate-plate fixtures (diameter 25 mm). The shear stress was stepwise increased from 1 to 1000 Pa and normal force values varied from 0N to 2N. Video recordings were performed using a high-speed camera (MikroCam II 3.1MP, Bresser, Ghede, Germany) in order to visualize the deformation of the sample rim. Slip velocity v_s at the rim of the plate was determined using Equation 5.1, where n is the plate rotational velocity and r is the plate diameter.

$$v_s = 2n\pi r \qquad (5.1)$$

Capillary rheometry: High shear viscosity data were determined at 20°C using a self-assembled piston-driven capillary rheometer. The samples were forced to flow through a stainless steel capillary with 0.5mm diameter and 80mm length at controlled volumetric flow rates corresponding to constant shear rate values using a piston of 20 mm diameter. The resulting extrusion pressure was recorded using a pressure transducer (0 - 50 bar, Dynisco Europe GmbH, Heilbronn, Germany).

Uniaxial compression tests: Uniaxial unconfined compression tests were performed at 20°C using the commercial tensile testing machine Texture Analyzer TA.XTplus (Stable Micro System, UK) equipped with a 5 kg load cell. Tests were performed on cylindrically shaped gels of 5 mm height and 10 mm diameter. Samples

were compressed with a plate (5 cm x 5 cm) at a compression speed of 0.1 mm/s. Young's modulus E was determined as the slope of the linear stress-strain curve in the strain region < 40%.

5.2.3 Microrheology

Multiple particle tracking (MPT): A detailed scheme of the MPT setup used in this study is described in [91]. It is based on an inverted fluorescence widefield microscope (Axio Observer D1, Carl Zeiss) equipped with a Fluar 100x objective (numerical aperture 1.3, 100x magnification, oil immersion lens, Carl Zeiss). Green fluorescent carboxyl-functionalized polystyrene microspheres of 0.2 µm diameter with density 1.06 g/cm³ and refractive index 1.59 at 589 nm were used as tracer particles (Bangs Laboratories, USA). The investigated samples including the tracer particles were placed between a microscope glass slide and a coverslip. The microscope was focused roughly halfway into the sample, i.e. at a distance of 20-40 µm away from the surface, to minimize wall effects. 2D images (field of view 127 x 127 µm, frame rate 50 frames/sec) of the fluorescent particles were recorded using a sCMOS camera Zyla X (Andor Technology). Movies of the fluctuating microspheres were analyzed using a custom MPT routine incorporated into the software Image Processing System (Visiometrics iPS) [240,241]. Particle tracking and calculation of mean square displacement (MSD), as well as the statistical analysis of the trajectories was done using a self-written Matlab® program based on the widely used Crocker and Grier tracking algorithm [91,242]. Tracer particles were added prior to gelation, to ensure a homogeneous distribution of the tracer particles within the sample. The local viscoelastic modulus *G*(ω)* around a sphere as a function of the frequency *ω* can be determined from Equation 5.2 [92]:

$$G^*(\omega) = \frac{k_B T}{\pi a i \omega \langle \Delta \tilde{r}^2(i\omega) \rangle} = G'(\omega) + iG''(\omega) \qquad (5.2)$$

with a being the tracer particle radius, k_B the Boltzmann constant, *T* the temperature and $\langle \Delta \tilde{r}^2(i\omega) \rangle$ the Mean Square Displacement (MSD) of the tracer particles.

Tracers trapped in an elastic network exhibit a time-independent MSD directly related to the apparent local shear modulus of this region:

$$G_{0,MPT} = \frac{2k_BT}{3\pi a\Delta r^2} \quad (5.3)$$

Tracers freely diffusing in a viscous environment exhibit a linearly increasing MSD and the apparent viscosity η_{MPT} of the surrounding fluid is determined using Equation 5.4 obtained from the Stokes-Einstein relation [243], and the relation $\langle \Delta r^2(\tau) \rangle = 4D\tau$, where *D* is the diffusion coefficient related to the MSD $\langle \Delta r^2(\tau) \rangle$ as a function of the lag time τ [93]:

$$\eta_{MPT} = \frac{k_BT}{6\pi aD} \quad (5.4)$$

5.2.4 Printing quality evaluation with extrusion based 3D printing

The gelatin-based hydrogels were printed on microscope glass slides using a pressure-controlled Voxel 8 Developer's Kit 3D printer (Voxel 8 Inc., Harvard, USA). 3CC cartridges (Nordson EFD, Feldkirchen, Germany) and straight needles of stainless steel, (0.15 mm outlet diameter and 12mm length, VIEWEG, Germany), were used to extrude the hydrogels in log pile pattern (self-written G-Code) and in ear shape construct (Human Right Ear model by col98 available in https://www.thingiverse.com/thing:1697869) with pressure values varying from 0.3 to 0.4 MPa. The print head velocity was kept at 600 mm/min for all samples. The 3D constructs were imaged using a Digital Microscope VHX-950F (Keyence, Neu-Isenburg, Germany) and image analysis of printing quality was performed with the software Image Processing System (Visiometrics iPS).

5.2.5 Cell encapsulation and 3D bioprinting

Human Hepatocellular Carcinoma (HepG2) and Normal Human Dermal Fibroblasts (NHDF) cells were detached from their respective cell culture flasks with trypsin-EDTA 0.25 % and suspended in DMEM (high glucose). The gelatin-based gels

were liquefied by heating to 37 °C. Then, 950 µl of sample was gently mixed with 50 µl of cell suspension (either HepG2 or NHDF) so that the bioink contained a final cell concentration of 2,5 x 10^6 cells/ml. Controls (200 µl) were taken prior to printing and the cell-laden gelatin-based bioink was placed in a syringe and allowed to thermally gelate for 30 min - 1 h at 20°C. The extrusion based 3D bioprinter BioSpot BP (Biofluidix GmbH, Freiburg, Germany) was used for bioprinting at 20°C. Bioinks were 3D printed in log pile shapes with 4 layers on adhesive slides with 250 µm straight needles of stainless steel at an extrusion rate of 0.015-0.02 mm/s and a printing speed of 5 mm/s. 3D printed constructs were enzymatically crosslinked with 10wt.% (for gels evaluated on day 1) and 20wt.% (for gels evaluated on day 7) transglutaminase (100U/g, kindly provided by Ajinomoto, Co., Kawasaki, Japan). The enzyme dispersion was prepared by stirring the powder with ultra-pure water at 50°C for 10 minutes. The enzyme dispersion was dripped on top of the printed constructs and left for 1 hour before washing with $DPBS^{-/-}$ (Dulbecco's Phosphate Buffered Saline, without calcium and magnesium). 3D printed constructs were covered with 10 ml DMEM in a petri dish and furthered cultivated at 37°C and 5%CO_2. DMEM, $DPBS^{-/-}$ and trypsin-EDTA used in this section were purchased from Gibco® Life Technologies, Carlsbad, USA.

5.2.6 Live/Dead staining

Post printing cell viability was assessed for HepG2 cells at day 1 and NHDF cells at days 1 and 7. The supernatant cell medium was removed and the cell-laden hydrogel constructs were stained with Calcein-AM (4 µg/ml, Life Technologies, Carlsbad, USA) and propidium iodide (20 µg/ml, Sigma-Aldrich, Taufkirchen, Germany). After 30 minutes of incubation, the staining solution was removed, the constructs were washed twice with DPBS and then covered with cell culture medium. Z-stack images were recorded for evaluation using the confocal microscope Leica Stellaris 5 (Leica Microsystems GmbH, Wetzlar, Germany). At least three parallel images were analyzed and HepG2 cell viability was determined by the fraction of viable cells over the total cell count and NHDF cell viability was determined by the fraction of detected live cell area over the total cell area with the software ImageJ.

5.2.7 Statistical analysis

Data are depicted as mean ± SD with N ≥ 3 for all groups. Comparisons between different data sets were performed using one-way ANOVA with Bonferroni correction. Differences were statistically significant for $p < 0.05$.

5.3 Results

5.3.1 Micro-heterogeneity characterization

We present two strategies for inducing micro-heterogeneity in gelatin hydrogels: addition of a second polymer and addition of nanoparticles. Measuring the particle distribution and particle trajectories in the bioink via MPT using fluorescent carboxyl-functionalized polystyrene microspheres allows for the microrheology by imaging technologies. Overlay images created from 500 images taken from MPT video sequences show that pure gelatin is a homogeneous hydrogel, with tracer particles uniformly dispersed in the 6G sample (Figure 5.1A). By adding a second polymer (PVA), a heterogeneous micro-structure in the form of discrete pore-like inclusions appears, corresponding to the white areas (some are green colored) in Figure 5.1B-C containing no tracer particles. The detected mean square displacements (MSDs) are time independent, indicating that all tracers are embedded in the elastic matrix environment provided by the gelatin gel for all compositions with local elasticity $G_{0,MPT}$ in the range of 10-25 Pa (Figure 5.1F shows MSD example for sample 6G2P). In order to characterize the void spaces of the gels with PVA, tracer particles were directly injected into the inclusions with a syringe (Figure 5.1G). The MSDs vary linearly with time, as shown exemplarily for sample 6G2P in Figure 5.1H indicating that the tracer particles are diffusing freely in the surrounding material. These inclusions are presumably formed of aqueous PVA solution. When gelatin thermal gelation occurs, PVA in solution demixes from the elastic matrix forming the beads-free, pore-like viscous inclusions while the tracer particles are arrested and remain in the gelatin elastic region. Liquid-liquid and solid-liquid separation normally depend on environmental stimuli, such as temperature or pH [216,217]. In our study, liquid gelatin and PVA solutions were well mixed with the tracer particles at 40°C. By decreasing the temperature, micro-phase demixing is

triggered and ceases (together with gelatin physical thermal crosslinking) when room temperature (20°C) is reached. By increasing PVA concentration from 2 to 4wt.%, size of the pores increases from 5±2 μm to 28±11 μm and local viscosity η_{MPT} in the pores from 6±4 mPas to 30±4 mPas (corresponding to PVA concentrations of ~5 and ~6.5wt%, respectively), as obtained by MPT measurements. At the same time, the fraction of viscous area in the elastic hydrogel increases from 2±1% to 24±5%, suggesting that more PVA demixed from gelatin.

Turning to the second strategy, the addition of nanosilicate particles (Laponite-XLG XR), induces formation of densely packed micro-heterogeneities depleted of tracer beads and presumably constituted of polymer and nanoparticles aggregates (Figure 5.1 D-E). Gelatin and Laponite interact electrostatically, especially in the presence of electrolyte, such as the salts present in the aqueous solvent DMEM, leading to micro-phase separation and aggregate formation [221,244]. By increasing Laponite concentration from 0.2 to 0.4wt.%, agglomerate size increases from 34±14 μm to 82±32 μm and the fraction of micro-heterogeneities in the gel increases from 4±3 to 26±15%, indicating that micro-phase separation was enhanced. Micro-heterogeneities characteristics for all samples are summarized in Table 5.2. Note, these micro-heterogeneities characteristics are valid for the gel preparation method described here. Other preparation methods might result in micro-heterogeneities with different features.

Table 5.2 – Size, viscosity and fraction of micro-heterogeneities in samples 6G2P, 6G4P, 6G0.2L and 6G0.4L.

Sample	**Size / μm**	**Viscosity (η_{MPT}) / mPas**	**Fraction in the gel / %**
6G2P	5±2	6±4	2±1
6G4P	28±11	30±4	24±5
6G0.2L	34±14	-	4±3
6G0.4L	82±32	-	26±15

Similar to the system with PVA, MSD of all tracers dispersed in the gelatin/Laponite matrix are time independent with 10 Pa < $G_{0,MPT}$ < 25 Pa (data not shown).

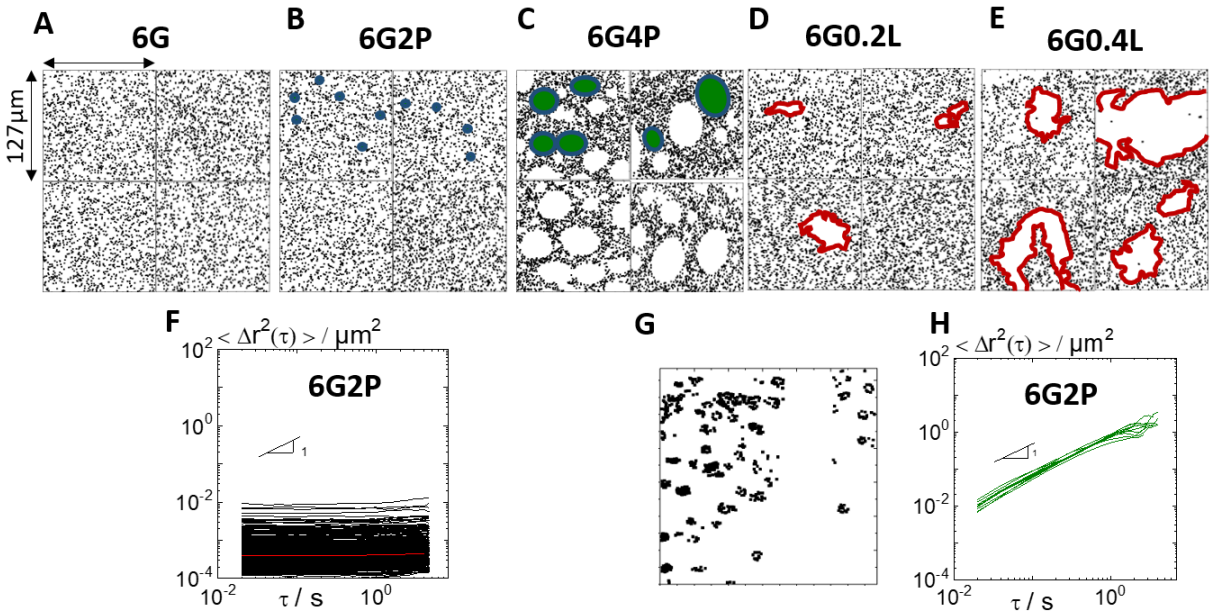

Figure 5.1 - (A)-(E) Overlay plots for samples 6G, 6G2P, 6G4P, 6G0.2L and 6G0.4L (four videos were analyzed for each concentration), some viscous inclusions are indicated in green and polymer/nanoparticle clusters are indicated in red, (F) representative MSDs of elastic trajectories as a function of lag time for sample 6G2P, (G) overlay plot for tracer particles directly injected in viscous inclusions, (H) representative MSDs of viscous trajectories for sample with 6G2P, as obtained by MPT measurements.

5.3.2 Macrorheological characterization: slip, shear-induced fracture and elasticity

PVA demixing from gelatin matrix leads to formation of a liquid phase that can potentially act as a lubrication layer for the hydrogel during extrusion. Based on this hypothesis, experiments were performed with the rotational rheometer in order to evaluate the slip behavior of the samples. The onset of slip is characterized by the critical shear stress τ_S necessary for the upper plate to rotate while the hydrogel remains intact. From the video snapshots, liquid is released when compressing gels including PVA (see Figure 5.2A). This liquid phase is also responsible for the sample to slide away from parallel plate geometry at high shear stresses even before it breaks (Figure 5.2B). This pronounced slip behavior is not observed for the pure gelatin gel and the gelatin/Laponite composites (6G, 6G0.2L and 6G0.4L), in which no liquid spillage takes place during compression (Figure 5.2F). The lack of lubrication leads to eventual gel

fracture at high shear stresses (Figure 5.2G). Video recordings of these experiments are found in the supplementary material (V1 and V2).

The critical slip stress values for gels 6G, 6G0.2L and 6G0.4L were very similar, τ_s ≈1000 Pa (Figure 5.2C). Gels with PVA, on the other hand, start slipping at much lower shear stresses due to lubrication layer (τ_s ≈500Pa for sample 6G2P and τ_s ≈250Pa for sample 6G4P). For shear stresses higher than the slip stress, the apparent slip velocity was determined at the rim of the rotating plate (Equation 5.1). Again, pronounced slip behavior is observed for samples with PVA as the slip velocity for these gels is approximately 2 orders of magnitude higher than for pure gelatin and mixed gelatin/Laponite gels when compared at a given shear stress (Figure 5.2D). This slip phenomenon for samples 6G2P and 6G4P is expected to play a crucial role during EBB as well. This shows up directly in the flow curves obtained from capillary rheometry. In this technique samples are extruded through a capillary using a piston, mimicking the EBB process. Apparent viscosity curves for gelatin and mixed gelatin/Laponite gels (samples 6G, 6G0.2L and 6G0.4L) shown in Figure 5.2E are very similar, showing that Laponite aggregates do not affect gel apparent flow behavior. For samples with PVA, however, a drop in viscosity is observed in the whole shear rate range investigated, which is associated with the pronounced slip behavior.

The brittle behavior observed in pure gelatin gels is even more pronounced when Laponite is introduced. Samples 6G0.2L and 6G0.4L break at lower shear stress $\tau_B \leq 3$ kPa in comparison to sample 6G, $\tau_B \approx 5$ kPa (Figure 5.2H). Uniaxial compression tests also show a pronounced drop in the Young's modulus E for gels with Laponite in comparison to pure gelatin and samples with PVA (Figure 5.2I). This is presumably due to the polymer/nanoclay agglomerates acting as stress concentration spots in the hydrogel. These highly stressed regions can lead to localized yielding and plastic deformation of the material [245]. Load-bearing particulate aggregates undergo non-affine deformation that induces buckling and accelerated material failure [246]. The brittle characteristic of mixed gelatin/Laponite gels under compression is expected to affect its performance in EBB as well.

Gelatin is usually functionalized, allowing for a chemical crosslinking to a stable scaffold for tissue engineering. The functionalization and the rate of crosslinks within the

gelatin hydrogels influences the pore size and the mechanical properties. Tuning of crosslinking density and mechanical properties is of great relevance for growth and differentiation of living cells in gelatin hydrogels [247]. An increase in shear elastic modulus G_0 was observed for both strategies of micro-heterogeneity formation presented in this study, despite the absence of gelatin functionalization (Figure 5.2J). Even though PVA is not crosslinked and remains in solution, hence not directly contributing to the elasticity, G_0 increases from 475 Pa (sample 6G) to 927 Pa (sample 6G4P). For comparison, a gelatin concentration, i.e. amount of physically crosslinked polymer, of 8wt.% is required to obtain a modulus G_0 =1000 Pa in a uniform gel (Figure S1). A densely crosslinked polymer network can impair nutrient diffusion and cell proliferation [153], aside from enhancing cell damage while printing due to higher viscosity and thus higher shear stresses [248]. The addition of PVA increases elasticity in a comparable way without further addition of crosslinked polymer and at the same time induces a porous configuration. Similarly, an investigation conducted with alginate based hydrogels shows that a gel with lower alginate content but enhanced heterogeneity exhibits elasticity equivalent to a more homogeneous gel with higher polymer content (Figure S2).

In addition, the gelatin/Laponite interaction and aggregate formation leads to an increase in G_0 from 475 Pa (sample 6G) to 630 Pa (sample 6G0.4L). This elasticity enhancement at small shear deformations due to micro-heterogeneities generated in gelatin gels is expected to show positive effects on the mechanical stability of 3D printed constructs.

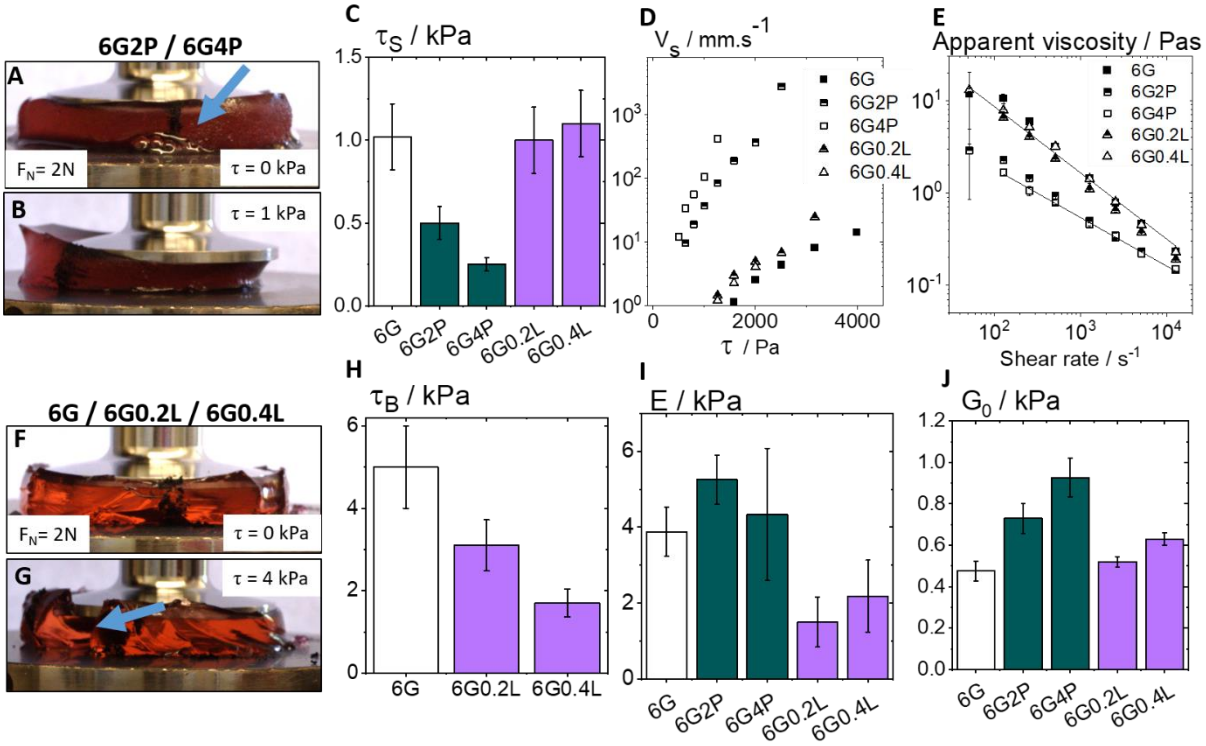

Figure 5.2 – (A-B),(F-G) Video snapshots during shear stress ramp measurements with a plate-plate rheometer, for full videos see Suppl. Mat. V1-2, a constant normal force F_N = 2N was applied during all stress ramp experiments, (A) liquid coming out of gel at rest indicated by the arrow and (B) sample sliding away at acritical stress of 1 kPa, characteristic behavior of samples 6G2P and 6G4P, (F) no liquid coming out under compression at rest and (G) hydrogel fracture at a critical stress τ_B = 4 kPa indicated by the arrow, this behavior is characteristic of samples 6G, 6G0.2L and 6G0.4L; (C) slip stress, (D) slip velocity and (H) fracture stress as obtained by shear stress ramp measurements with a plate-plate rheometer at a normal force of 2N; (E) Apparent viscosity determined by capillary rheometry; (I) Young's modulus E determined by compression tests; (J) Bulk shear modulus G_0 determined by shear rheometry.

5.3.3 EBB: printing quality evaluation

The printing quality of the hydrogels was evaluated in 3 steps: 2D log pile geometry (2 printed layers), 3D log pile (5mm high and 15mm length) and complex construct (human ear shape, 7mm high and 3cm length), without supporting material.

All gels show decent filament quality when 2D constructs are printed (Figure 5.3A-E). Hydrogels including only a small fraction of viscous droplets or dense particle clusters (6G2P and 6G0.2L, see Tab. 5.2), however, display distinctly improved line quality, with thinner (line width < 0.6 mm, Figure 5.3F) and more uniform lines than pure gelatin (6G, line width ~1 mm) and gels with more pronounced heterogeneity (6G4P and

6G0.4L, line width > 0.75 mm). Note, the higher shear modulus of the heterogeneous hydrogels does not necessarily lead to a decrease in line width, which is observed for homogeneous pure gelatin gels (Figure S1). This suggests that the slip or gel fracture phenomena described above may also contribute to the print quality of such gels, likewise the proportion and magnitude of heterogeneities could play a role in the uniformity of the printed lines.

When more layers are added and 3D constructs are printed, the disparity in printing quality becomes more relevant. Finer printed lines obtained from gels 6G2P and 6G0.2L form 3D constructs with superior top surface geometrical accuracy. This superior printability with moderately heterogeneous gels appears to be essential for complex constructs 3D printing, as good resolution and excellent shape fidelity were achieved with gels 6G2P and 6G0.2L when printing a human ear geometry. The human ear 3D model is a complex object with a rounded shape which displays more details than the simpler grid geometry (Figure 5.3G). Self-standing ear helix overhangs of approximately 58° were successfully printed 4mm above the glass slide with sample 6G2P (Figure 5.3H). Moreover, all the printed constructs display mechanical stability provided by the high elastic shear modulus, and they do not collapse when positioned upright (see Figure 5.3I for sample 6G2P). The pure gelatin gel 6G and also the mixed gels with pronounced heterogeneity 6G4P and 6G0.4L did not provide good resolution for complex shaped constructs and failed in terms of shape fidelity.

The presence of viscous pore-like inclusions in 6G2P gel enhances slip behavior while polymer-nanoclay aggregates in 6G0.2L gel promote brittle failure and lead to gel fracture at lower stresses than pure gelatin. Regardless of whether the micro-heterogeneities are viscous or solid, both of these phenomena facilitate extrusion, allowing the fabrication of complex 3D constructs with excellent printing quality. However, this is not observed for samples 6G4P and 6G0.4L, in which the micro-heterogeneities are larger and their fraction is higher (> 20%). While targeted introduction of micro-phase separation is shown to significantly improve extrusion in comparison to the homogeneous gel, the size and amount of the micro-heterogeneities has to be limited for successful high quality printing. For uniform filament extrusion, the micro-heterogeneity dimensions should be considerably smaller than the printed feature

size, namely the nozzle diameter. As a rule of thumb, particle aggregates should be 10 times smaller than the nozzle size to avoid clogging [249] or filament interruptions in case of freely flowing viscous inclusions. For the systems studied here, a 150 µm diameter nozzle was employed and positive results were obtained for gels with small inclusion size (5±2µm for sample 6G2P) as well as with larger micro-heterogeneities (34±14µm for sample 6G0.2L) that, however, are scarcely present (4±3% of the total hydrogel area). On the other hand, larger viscous inclusions or aggregates (>28 µm) amounting to more than 24% of hydrogel fraction (samples 6G4P and 6G0.4L) impair filament uniformity. Similarly, for alginate based hydrogels, several small viscous inclusions (up to 12±6µm) which amount to 18% of the hydrogel volume allow for uniform filament printing in 2D (Figure S2), while few large micro-heterogeneities that reach 100 µm in size disrupt filament uniformity.

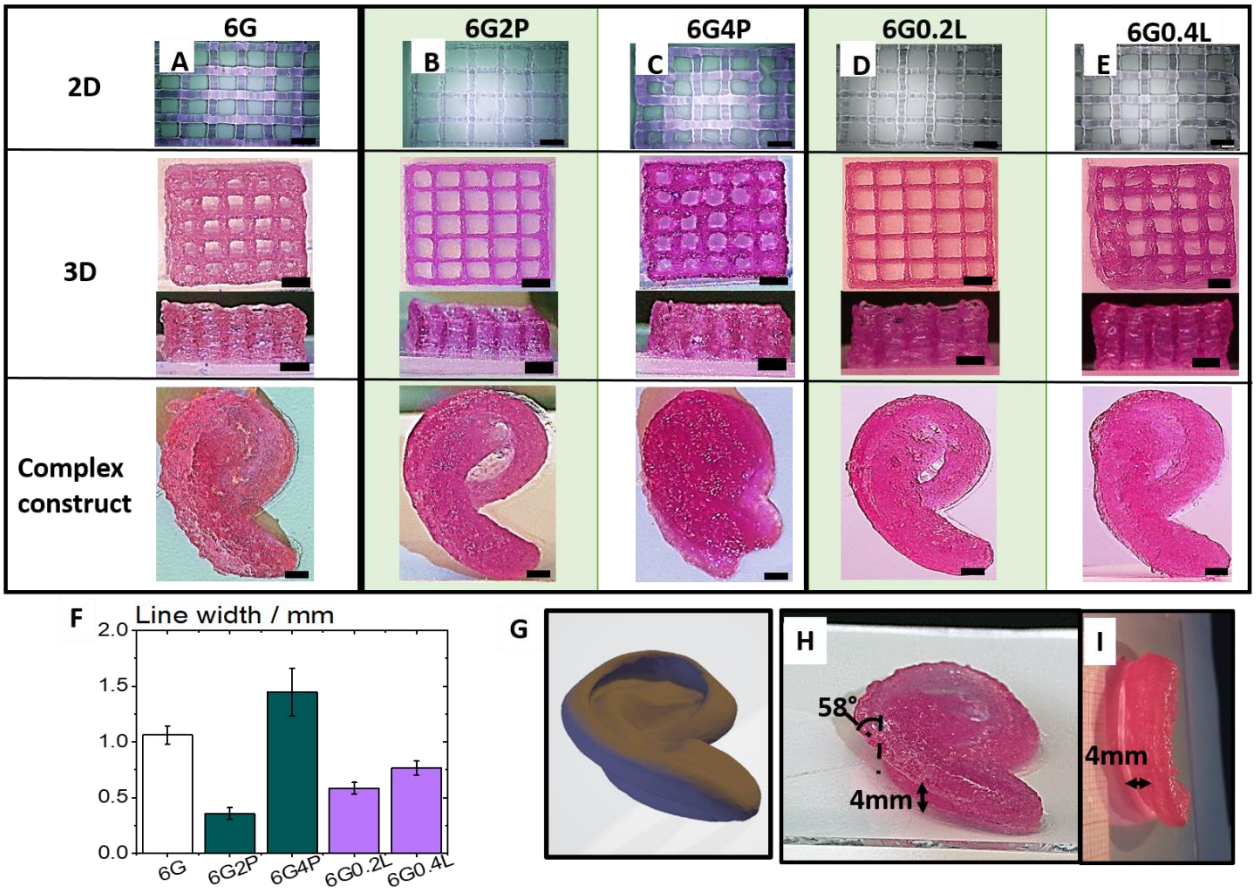

Figure 5.3 – 2D log-pile, 3D log-pile (top and side view) and human ear shape complex constructs (top view) printed with (A) 6G, (B) 6G2P, (C) 6G4P, (D) 6G0.2L and

(E) 6G0.4L samples. Scale bar: 3mm. (F) Line width determined from 2D construct; (G) human ear 3D model; (H) self-standing ear helix overhang of 58° printed 4mm above the glass slide with sample 6G2P; (I) unsupported printed ear positioned upright. All printing experiments were performed using a straight nozzle with 0.15 mm diameter.

5.3.4 3D bioprinting: cell viability

Bioprinting experiments were performed with human hepatocarcinoma HepG2 cells embedded in the 6wt.% and 8wt.% gelatin based hydrogels to evaluate the impact of the 3D printing process on the cell viability. Log pile structures of four layers were printed at 20°C. Live/dead assay (Figure 5.4A-G) reveals high cell viability at day 1 for hydrogels with PVA (>50% for 8% and >65% for 6% gelatin compositions) (Figure 5.4D), while viability was considerably lower for homogeneous pure gelatin hydrogels (<35% for both 6G and 8G samples). The slip induced by the viscous PVA inclusions leads to a dominating plug flow and the contribution of shear deformation to gel transport during extrusion is low. This presumably protects the cells, causing less damage and improving viability.

Similarly, printing with hydrogel composites including Laponite (6G0.2L and 6G0.4L) resulted in higher cell viability >65% (Figure 5.4H-K). This suggests that the brittle behavior caused by the nanoclay aggregates, which facilitates extrusion, also mitigates cell damage during printing and actually increases cell viability. Cell viability values after printing were normalized with the non-printed control. It is worth noting that Laponite agglomerates present in 0.2L and 0.4L gels interact with propidium iodide used to stain non-viable cells, corresponding to the non-cell like red shapes in the images. The presence of these large agglomerates was excluded from the evaluation by normalizing the cell viability with the controls.

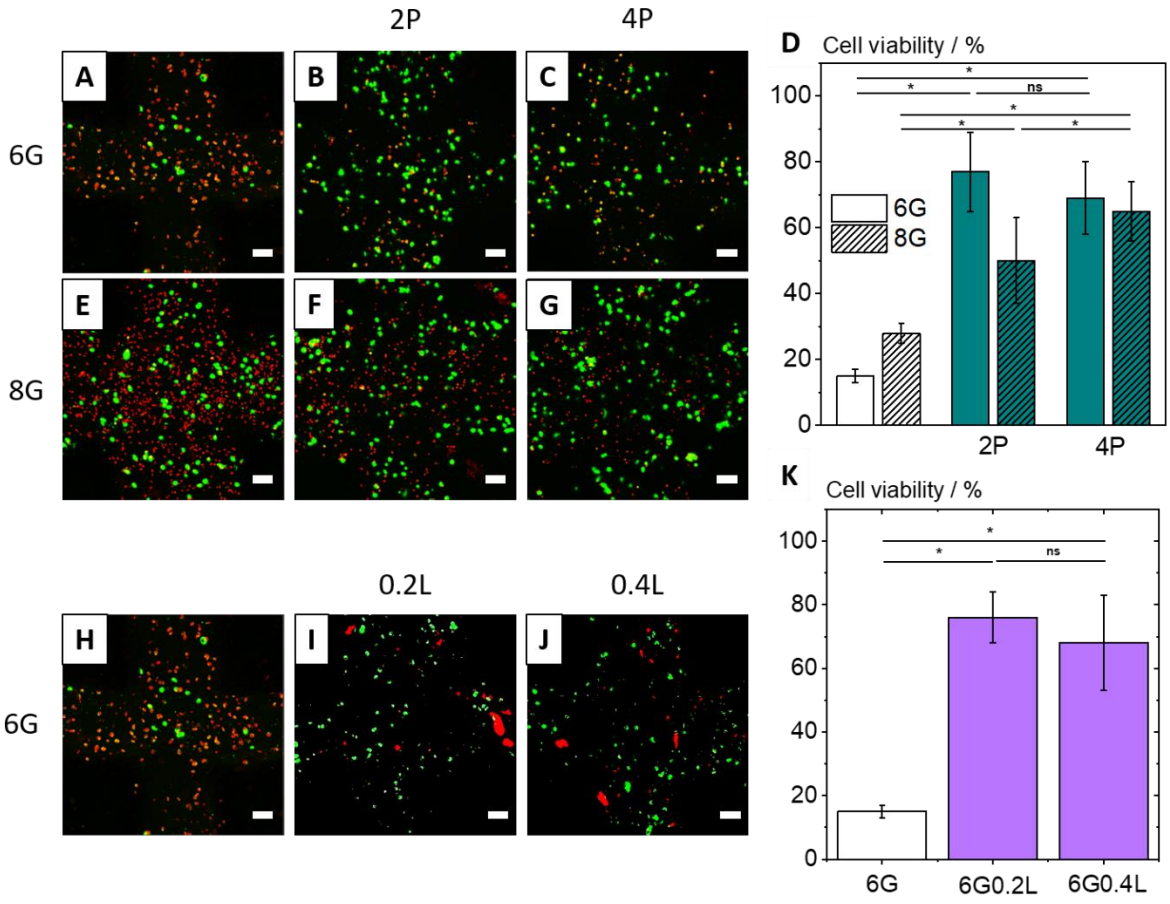

Figure 5.4 – Live/dead staining of HepG2 cells embedded in samples (A)-(C) 6G, 6G2P, 6G4P, (E)-(G) 8G, 8G2P, 8G4P and samples (H)-(J) 6G, 6G0.2L, 6G0.4L followed by confocal microscopy. Live cells were stained with calcein-AM (green) and damaged cells with propidium iodide (red). Scale bar: 100μm. (D);(K) Cell viability as determined by the fraction of viable cells over the total cell count. Data is present as mean ± SD and * indicates $p<0.05$.

Normal human dermal fibroblasts NHDF cells were embedded in the homogeneous sample 6G and in the weakly heterogeneous samples 6G2P and 6G0.2L, which provided excellent printability and higher viability with HepG2 cells. Hydrogels were printed in log pile geometries of 4 layers and cell viability was analyzed on day 1 (Figure 5.5A-C) to evaluate direct 3D printing impact and on day 7 of cell culture (Figure 5.5E-G). On day 1, hydrogel 6G showed cell viability <80%, while gels 6G2P and 6G0.2L presented an improved viability >85% (Figure 5.5D). On day 7, cells exhibited elongation with similar morphology in all gels. NHDF cells were more concentrated on the rim of the hydrogel and viability was >90% for all samples. Extensive research over the last

decades has established that gelatin-based gels provide good environment for cell proliferation [250,251]. However, much less is known about mechanisms of micro-heterogeneity formation and how to control it in such gels. In this study, we developed two different gelatin-based bioinks with tailored micro-heterogeneity which allow for fabrication of complex 3D constructs with excellent printability and provide cell viability significantly higher than in uniform gelatin gels right after printing as well as after 7 days of cell culture.

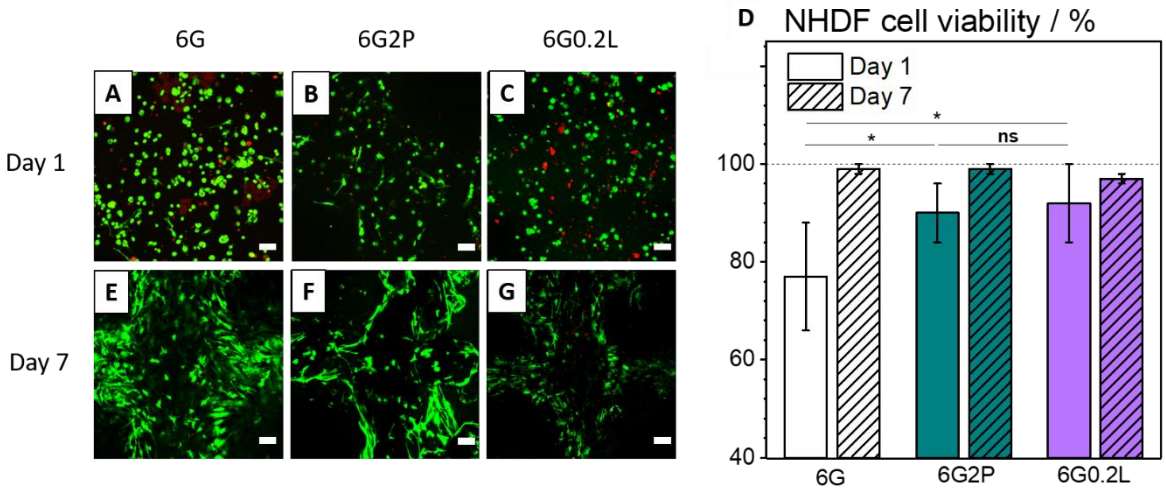

Figure 5.5 - Live/dead staining of NHDF cells embedded in samples 6G, 6G2P, 6G0.2L post-printing at (A)-(C) day 1 and (E)-(G) day 7 followed by confocal microscopy. Live cells were stained with calcein-AM (green) and damaged cells with propidium iodide (red). Scale bar: 100µm. (D) Cell viability as determined by the fraction of detected live cell area over the total cell area. Data is present as mean ± SD and * indicates $p<0.05$.

5.4 Conclusion

Targeted micro-phase separation generates highly elastic bioinks with a complex micro-structure. Here we investigated non-functionalized gelatin-based gels and characterized the introduced microheterogeneities with respect to their size, shape, volume fraction, and local mechanical properties using MPT microrheology. Generally, micro-heterogeneity formation in hydrogels leads to an increase in the bulk shear

modulus, but other effects on bulk mechanical behavior were observed depending on the heterogeneity type. Gelatin/PVA hydrogels with their viscous PVA inclusions presented distinct slip behavior with a low critical stress τ_S at which slip sets in and a very high slip velocity at stresses $\tau > \tau_S$. Gelatin/Laponite composites include dense nanoclay/polymer clusters resulting in brittle behavior under compression and a reduced shear stress τ_B at which the hydrogels break. Although the effects of both types of heterogeneities on the macro-mechanical properties are evidently different, in both cases smooth material extrusion at 20°C and reduced damage to cells during extrusion based bioprinting is observed. Objects with higher precision, uniformity and shape fidelity could be obtained without support material by using heterogeneous composite gels. However, size and fraction of heterogeneous inclusions has to be adjusted carefully in order to obtain excellent printing quality. The length scale of the heterogeneities must be well below the nozzle outlet diameter and the fraction of the (soft and viscous or solid) inclusions should not be too high (<24%) in order to achieve interruption free, uniform filaments. In this study we developed heterogeneous, highly elastic gels that allow for printing of complex self-standing 3D structures at room temperature with better resolution, shape retention and higher cell viability in comparison to the equivalent homogeneous gelatin hydrogel. Cell viability directly after printing was drastically increased when printing human hepatocarcinoma HepG2 cells embedded in heterogeneous gels. The effect was less pronounced for normal human dermal fibroblasts NHDF cells which exhibit a fairly high viability even if embedded in a homogeneous gelatin bioink.

MPT microstructural characterization can help tailor favorable microenvironment conditions and bulk elasticity for 3D printing with living cells. Modulation of the microstructure via inducing viscous pore-like inclusions or micro-heterogeneity formation caused by polymer-nanoclay interactions in gelatin networks is of great importance for printing quality as well as supportive microenvironment development for cell 3D printing. The concept of introducing micro-heterogeneities can be transferred to other hydrogel systems in a straight forward manner and thus may stimulate development of further strategies for improving print quality and cell viability.

Summary and Outlook

Bioinks are basically comprised of living cells embedded in biocompatible carrier materials, usually hydrogels. Bioink mechanical and chemical properties are critical and dictate how successful the 3D bioprinting process is in terms of cell viability and printability. Therefore, it is of great importance to thoroughly characterize the hydrogel as well as the precursor polymer solution used as part of the bioink. Hydrogels consisting of biopolymer networks, such as alginate, gelatin, chitosan and collagen, are usually employed as bioinks, due to their natural biocompatibility and affordability.

In the first publication of this thesis, classical bulk rheometry in combination with DWS and MPT optical microrheology were used to characterize linear viscoelastic properties of alginate solutions in water and, for the first time, in PBS and DMEM. When preparing bioinks, the polymer is often solubilized in PBS or DMEM solutions in order to maintain physiological conditions of pH and ionic strength. Besides, DMEM offers nutrients for cells when they are placed in culture chambers. The solvent quality can affect polymer conformation and therefore its structural and dynamical properties. At concentrations higher than 1wt.%, relevant for bioprinting, alginate solutions in salt free water and PBS exhibit scaling exponents for the concentration dependence of the specific viscosity η_{sp} and the plateau modulus G_0 that agree well with theoretical predictions for neutral polymers in good solvent. For the terminal relaxation time T_R, a slightly stronger concentration dependence is observed compared to theoretical predictions, presumably due to the formation of aggregates in this high alginate concentration regime. For alginate dissolved in DMEM, all scaling exponents for η_{sp}, G_0 and T_R agree with predictions for neutral polymers in theta solvents and lower persistence length values for alginate dissolved in DMEM were obtained directly from high frequency rheological measurements for the first time. The formation of polyelectrolyte complexes due to interactions between alginate and amino acids present only in DMEM might explain the distinct solvent quality. Chain flexibility, as characterized by the persistence length, might affect cell adhesion and proliferation [104]. Whether this difference in the chain flexibility due to solvent quality obtained in this work affects

the cell adhesion or not is a topic to be addressed in future research. Additionally, our findings suggest, that alginate chain conformation seems not to change with temperature, indicating the possibility of varying bioink temperature during bioprinting without any change of the polymer conformation. Regarding the presence of micro-heterogeneities, MPT results reveal a homogeneous structure of alginate solutions down to the 200 nm length scale in the concentration range investigated here. Further investigations with solutions of other biopolymers, such as gelatin, chitosan and collagen, in different solvents frequently used in bioprinting should be conducted in order to better understand the general role of solvent in polymer conformation and chain flexibility as well as in the rheological properties of precursor polymer solutions.

Hydrogels tend to slip under flow due to the high amount of water. Wall slip behavior depends on the wetting properties of the hydrogel and the nozzle material as well as of the magnitude of shear stress applied. When hydrogels are used as bioinks in 3D bioprinting it is of great interest to fully understand the impact of wall slip on the printing quality. In the second publication of this thesis, we thoroughly investigated wall slip, flow behavior and elasticity of alginate as well as gelatin-based hydrogels with respect to the impact of these rheological and wetting properties on EBB. At stresses below the yield stress τ_y, rotational rheometry revealed that alginate-based hydrogels presented stronger slip than gelatin samples. Regarding the substrate, wall slip at low stresses is more pronounced on PP and PTFE plates than on stainless steel plates for all samples. Capillary rheometry and printing tests using nozzles made from stainless steel, PP and PTFE confirm that slip effect is negligible at stresses $\tau > \tau_y$. The EBB experiments confirmed that a higher yield stress of the bioink requires a higher extrusion pressure but improves the shape fidelity of multilayered 3D constructs, while increasing gel elasticity enhanced layer stacking quality. Although yield stress and elasticity clearly impact printing quality, there is no systematic investigation on how these properties affect cell viability. Further research with homogeneous hydrogels that show varying degrees of yield stress as well as elasticity should be conducted in order to evaluate their impact on the cell viability after printing. The strong slip at low stresses observed for the alginate gels is indicative of a heterogeneous microstructure. This showed up when irregular lines were printed with alginate gel while uniform filaments were obtained

from gelatin sample with similar yield stress and viscosity. This finding demanded further systematic investigations regarding the impact of bioink heterogeneity on the micrometer scale on macro-rheology and printing quality.

Accordingly, several hydrogel systems with varying degrees of micro-heterogeneity were developed and characterized in terms of micro-heterogeneity characteristics, bulk elasticity and extrusion quality. The third publication of this thesis presents a new generic design concept that allows to adjust the elasticity of polymeric and particulate extrudable gels based on the formation of heterogeneities on the length scale 1-100µm via different mechanisms of micro-phase separation. This concept abandons the assumption of uniform sample composition assumed in almost all theories referring to the viscoelastic behavior of gels, and offers new possibilities for enhancing mechanical gel strength without increasing polymer / particle concentration or average crosslink density. Microstructural and mechanical heterogeneities were characterized and spatially visualized by employing MPT technique. Micro-heterogeneity was enhanced in alginate hydrogels by accelerating crosslinking kinetics, generating higher elastic materials with substantially improved filament extrudability and shape fidelity. The addition of PVA solution hindered alginate crosslinking and resulted in softer, more homogeneous hydrogels, with larger extruded lines. Introducing PVA solutions into gelatin gels resulted in the formation of pore-like micro-heterogeneities, which increased the gel overall elasticity and improved width of extruded lines. Higher ionic strength in pure Laponite-based hydrogels via salt addition induced nanoparticle aggregation and formation of dense clusters inaccessible to tracer particles, producing gels of higher bulk elasticity and superior extrusion quality. Furthermore, addition of alginate solution to Laponite hydrogels prevented cluster formation due to nanoparticle-polysaccharide interactions, resulting in more homogeneous, softer materials with larger filament spreading. As established in this work, different material compositions will have particular requirements for triggering micro-phase separation in order to reach a micro-heterogeneity intensity relevant for elasticity enhancement. Further research should be conducted with different combinations of polymeric as well as particulate materials that were not investigated here but are commonly applied in (bio)extrusion processes, such as chitosan, collagen, hyaluronic acid, PEG, bioactive glass or carbon and cellulose

nanofibers. Comprehension of the possible interactions among the hydrogel components is the basis for a targeted and efficient micro-phase separation leading to an increase in elasticity.

The design model developed in this work provides deeper insight into complex hydrogel micro-structures in the hydrated state and may have implications not only in bioprinting but also in several applications in which hydrogel mechanical strength as well as heterogeneity are relevant, namely food and cosmetic gels. However, further investigations were needed on the impact of micro-heterogeneity size, type and volume fraction on the printing quality of extruded hydrogel filaments and how this depends on specific system properties. This study was conducted on the fourth publication. Moreover, the micro-heterogeneity characteristics might be relevant for applications other than bioprinting, such as food and cosmetics. Further research is necessary to better understand how size, volume fraction as well as local mechanical properties of micro-heterogeneities affect hydrogel organoleptic, sensory and texture properties.

As already demonstrated in the third publication, targeted micro-phase separation generates highly elastic bioinks with a complex micro-structure. In the fourth publication of this thesis, non-functionalized gelatin-based bioinks were investigated and the introduced micro-heterogeneities were carefully characterized with respect to their size, shape, volume fraction, and local mechanical properties using MPT micro-rheology. In this work we demonstrated that different effects on bulk mechanical behavior were observed depending on the heterogeneity type. Gelatin/PVA hydrogels presented viscous pore-like inclusions consisting of PVA in solution which lead to evident slip behavior. A low critical stress τ_S for the onset of slip was found for this system, with a very high slip velocity at stresses $\tau > \tau_S$. Gelatin/Laponite composites include dense nanoclay/polymer clusters that act as stress concentration spots, resulting in brittle behavior under compression and a reduced breaking shear stress τ_B.

The heterogeneity type clearly has an impact on the bioinks macro-mechanical properties. However, in both cases investigated here, smooth material extrusion at 20°C and reduced damage to cells during extrusion based bioprinting is observed. Scaffolds with improved uniformity and shape fidelity could be obtained without support material by using heterogeneous gelatin-based composite bioinks. It is worth noting, that size

and fraction of heterogeneous inclusions have to be adjusted carefully in order to obtain satisfactory printing results. The length scale of the heterogeneities must be well below the nozzle outlet diameter and the fraction of the inclusions should not be too high (<25%, depending on size). Heterogeneous, highly elastic gelatin-based bioinks that allow for printing of complex self-standing 3D structures at room temperature and without supporting material were developed in this study.

The micro-heterogeneities effects on the macro-mechanical properties, i.e wall slip for the gelatin/PVA bioinks and brittleness for the gelatin/Laponite gel, clearly facilitated the extrusion process, exhibiting a favorable repercussion on the cell viability as well. Accordingly, cell viability directly after printing was increased when printing human hepatocarcinoma HepG2 and normal human dermal fibroblasts NHDF cells embedded in heterogeneous gels. These findings can help tailor favorable microenvironment conditions and bulk elasticity for 3D printing with living cells and thus may stimulate development of further strategies for improving printing quality and cell viability. According to the results obtained from the fourth publication, wall slip induced in gelatin gels seems to favor cell viability. A detailed study on how wall slip directly affects cell viability is therefore of high interest. Hydrogels consisting of other biocompatible polymers and particles with varying degrees of wall slip should be carefully investigated in order to characterize the general effect of wall slip on the cell viability during bioprinting. Moreover, careful and thorough investigations are necessary on the effect of bioink micro-heterogeneities and its properties, such as type and volume fraction, on cell viability of distinct cell lines as well as of cells that are cultured for longer periods of time. Accordingly, further research is needed on the potential effect of micro-heterogeneity in internal vascularization of mature 3D constructs.

References

[1] Grand View Research, 3D Bioprinting market size: Share and Trends analysis report.

[2] M. Askari, M. Afzali Naniz, M. Kouhi, A. Saberi, A. Zolfagharian, M. Bodaghi, Recent progress in extrusion 3D bioprinting of hydrogel biomaterials for tissue regeneration: a comprehensive review with focus on advanced fabrication techniques, Biomaterials science 9 (2021) 535–573. https://doi.org/10.1039/d0bm00973c.

[3] P.S. Gungor-Ozkerim, I. Inci, Y.S. Zhang, A. Khademhosseini, M.R. Dokmeci, Bioinks for 3D bioprinting: an overview, Biomaterials science 6 (2018) 915–946. https://doi.org/10.1039/c7bm00765e.

[4] M. Kapałczyńska, T. Kolenda, W. Przybyła, M. Zajączkowska, A. Teresiak, V. Filas, M. Ibbs, R. Bliźniak, Ł. Łuczewski, K. Lamperska, 2D and 3D cell cultures - a comparison of different types of cancer cell cultures, Archives of medical science AMS 14 (2018) 910–919. https://doi.org/10.5114/aoms.2016.63743.

[5] S.V. Murphy, P. de Coppi, A. Atala, Opportunities and challenges of translational 3D bioprinting, Nature biomedical engineering 4 (2020) 370–380. https://doi.org/10.1038/s41551-019-0471-7.

[6] M.P. Mani, M. Sadia, S.K. Jaganathan, A.Z. Khudzari, E. Supriyanto, S. Saidin, S. Ramakrishna, A.F. Ismail, A.A.M. Faudzi, A review on 3D printing in tissue engineering applications, Journal of Polymer Engineering 42 (2022) 243–265. https://doi.org/10.1515/polyeng-2021-0059.

[7] S. Panda, S. Hajra, K. Mistewicz, B. Nowacki, P. In-Na, A. Krushynska, Y.K. Mishra, H.J. Kim, A focused review on three-dimensional bioprinting technology for artificial organ fabrication, Biomaterials science 10 (2022) 5054–5080. https://doi.org/10.1039/D2BM00797E.

[8] Z. Yazdanpanah, J.D. Johnston, D.M.L. Cooper, X. Chen, 3D Bioprinted Scaffolds for Bone Tissue Engineering: State-Of-The-Art and Emerging Technologies, Frontiers in bioengineering and biotechnology 10 (2022) 824156. https://doi.org/10.3389/fbioe.2022.824156.

[9] J. Huang, J. Xiong, D. Wang, J. Zhang, L. Yang, S. Sun, Y. Liang, 3D Bioprinting of Hydrogels for Cartilage Tissue Engineering, Gels (Basel, Switzerland) 7 (2021). https://doi.org/10.3390/gels7030144.

[10] F. Fazal, S. Raghav, A. Callanan, V. Koutsos, N. Radacsi, Recent advancements in the bioprinting of vascular grafts, Biofabrication 13 (2021). https://doi.org/10.1088/1758-5090/ac0963.

[11] T. Weng, W. Zhang, Y. Xia, P. Wu, M. Yang, R. Jin, S. Xia, J. Wang, C. You, C. Han, X. Wang, 3D bioprinting for skin tissue engineering: Current status and perspectives, Journal of tissue engineering 12 (2021) 20417314211028574. https://doi.org/10.1177/20417314211028574.

[12] A.Y. Safhi, Three-Dimensional (3D) Printing in Cancer Therapy and Diagnostics: Current Status and Future Perspectives, Pharmaceuticals (Basel, Switzerland) 15 (2022). https://doi.org/10.3390/ph15060678.

[13] A. Malekpour, X. Chen, Printability and Cell Viability in Extrusion-Based Bioprinting from Experimental, Computational, and Machine Learning Views, Journal of functional biomaterials 13 (2022). https://doi.org/10.3390/jfb13020040.

[14] K. Hölzl, S. Lin, L. Tytgat, S. van Vlierberghe, L. Gu, A. Ovsianikov, Bioink properties before, during and after 3D bioprinting, Biofabrication 8 (2016) 32002. https://doi.org/10.1088/1758-5090/8/3/032002.

[15] S. Boularaoui, G. Al Hussein, K.A. Khan, N. Christoforou, C. Stefanini, An overview of extrusion-based bioprinting with a focus on induced shear stress and its effect on cell viability, Bioprinting 20 (2020) e00093. https://doi.org/10.1016/j.bprint.2020.e00093.

[16] M.E. Cooke, D.H. Rosenzweig, The rheology of direct and suspended extrusion bioprinting, APL bioengineering 5 (2021) 11502. https://doi.org/10.1063/5.0031475.

[17] P.-G. de Gennes, Scaling concepts in polymer physics, 8th ed., Cornell Univ. Press, Ithaca, NY, ca. 2005.

[18] M. Rubinstein, R.H. Colby, Polymer physics, Oxford university press, Oxford, 2008.

[19] B.H. Zimm, Dynamics of Polymer Molecules in Dilute Solution: Viscoelasticity, Flow Birefringence and Dielectric Loss, The Journal of chemical physics 24 (1956) 269–278. https://doi.org/10.1063/1.1742462.

[20] R.H. Colby, Structure and linear viscoelasticity of flexible polymer solutions: comparison of polyelectrolyte and neutral polymer solutions, Rheol Acta 49 (2010) 425–442. https://doi.org/10.1007/s00397-009-0413-5.

[21] M. Rubinstein, R.H. Colby, A.V. Dobrynin, Dynamics of semidilute polyelectrolyte solutions, Physical review letters 73 (1994) 2776–2779. https://doi.org/10.1103/PhysRevLett.73.2776.

[22] P.E. Rouse, A Theory of the Linear Viscoelastic Properties of Dilute Solutions of Coiling Polymers, The Journal of chemical physics 21 (1953) 1272–1280. https://doi.org/10.1063/1.1699180.

[23] M. Doi, S.F. Edwards, The theory of polymer dynamics, Clarendon Press, Oxford, 1986.

[24] G. Strobl, The Physics of Polymers: Concepts for understanding their structures and behavior, Springer Berlin Heidelberg, Berlin, Heidelberg, 2007.

[25] W.L. Ng, C.K. Chua, Y.-F. Shen, Print Me An Organ! Why We Are Not There Yet, Progress in polymer science 97 (2019) 101145. https://doi.org/10.1016/j.progpolymsci.2019.101145.

[26] S. Vanaei, M.S. Parizi, F. Salemizadehparizi, H.R. Vanaei, An Overview on Materials and Techniques in 3D Bioprinting Toward Biomedical Application, Engineered Regeneration 2 (2021) 1–18. https://doi.org/10.1016/j.engreg.2020.12.001.

[27] I.T. Ozbolat, M. Hospodiuk, Current advances and future perspectives in extrusion-based bioprinting, Biomaterials 76 (2016) 321–343. https://doi.org/10.1016/j.biomaterials.2015.10.076.

[28] T. Zhang, W. Zhao, Z. Xiahou, X. Wang, K. Zhang, J. Yin, Bioink design for extrusion-based bioprinting, Applied Materials Today 25 (2021) 101227. https://doi.org/10.1016/j.apmt.2021.101227.

[29] K. Hölzl, S. Lin, L. Tytgat, S. van Vlierberghe, L. Gu, A. Ovsianikov, Bioink properties before, during and after 3D bioprinting, Biofabrication 8 (2016) 32002. https://doi.org/10.1088/1758-5090/8/3/032002.

[30] N. Paxton, W. Smolan, T. Böck, F. Melchels, J. Groll, T. Jungst, Proposal to assess printability of bioinks for extrusion-based bioprinting and evaluation of rheological properties governing bioprintability, Biofabrication 9 (2017) 44107. https://doi.org/10.1088/1758-5090/aa8dd8.

[31] C.W. Macosko, Rheology: Principles, measurements and applications by Christopher W. Macosko, Wiley-VCH, Chichester, 1994.

[32] V.H.M. Mouser, F.P.W. Melchels, J. Visser, W.J.A. Dhert, D. Gawlitta, J. Malda, Yield stress determines bioprintability of hydrogels based on gelatin-methacryloyl and gellan gum for cartilage bioprinting, Biofabrication 8 (2016) 35003. https://doi.org/10.1088/1758-5090/8/3/035003.

[33] S. Aktas, D.M. Kalyon, B.M. Marín-Santibáñez, J. Pérez-González, Shear viscosity and wall slip behavior of a viscoplastic hydrogel, Journal of Rheology 58 (2014) 513–535. https://doi.org/10.1122/1.4866295.

[34] N. Ashammakhi, S. Ahadian, C. Xu, H. Montazerian, H. Ko, R. Nasiri, N. Barros, A. Khademhosseini, Bioinks and bioprinting technologies to make heterogeneous and biomimetic tissue constructs, Materials today. Bio 1 (2019) 100008. https://doi.org/10.1016/j.mtbio.2019.100008.

[35] D. Kang, G. Ahn, D. Kim, H.-W. Kang, S. Yun, W.-S. Yun, J.-H. Shim, S. Jin, Pre-set extrusion bioprinting for multiscale heterogeneous tissue structure fabrication, Biofabrication 10 (2018) 35008. https://doi.org/10.1088/1758-5090/aac70b.

[36] H. Li, C. Tan, L. Li, Review of 3D printable hydrogels and constructs, Materials & Design 159 (2018) 20–38. https://doi.org/10.1016/j.matdes.2018.08.023.

[37] F. Liu, X. Wang, Synthetic Polymers for Organ 3D Printing, Polymers 12 (2020). https://doi.org/10.3390/polym12081765.

[38] F. Gao, C. Ruan, W. Liu, High-strength hydrogel-based bioinks, Mater. Chem. Front. 3 (2019) 1736–1746. https://doi.org/10.1039/c9qm00373h.

[39] D. Ji, J. Kim, Recent Strategies for Strengthening and Stiffening Tough Hydrogels, Adv NanoBio Res 1 (2021) 2100026. https://doi.org/10.1002/anbr.202100026.

[40] M. Mobaraki, M. Ghaffari, A. Yazdanpanah, Y. Luo, D.K. Mills, Bioinks and bioprinting: A focused review, Bioprinting 18 (2020) e00080. https://doi.org/10.1016/j.bprint.2020.e00080.

[41] S. Heid, A.R. Boccaccini, Advancing bioinks for 3D bioprinting using reactive fillers: A review, Acta biomaterialia 113 (2020) 1–22. https://doi.org/10.1016/j.actbio.2020.06.040.

[42] D. Chimene, R. Kaunas, A.K. Gaharwar, Hydrogel Bioink Reinforcement for Additive Manufacturing: A Focused Review of Emerging Strategies, Advanced materials (Deerfield Beach, Fla.) 32 (2020) e1902026. https://doi.org/10.1002/adma.201902026.

[43] C. Du, J. Hu, X. Wu, H. Shi, H.C. Yu, J. Qian, J. Yin, C. Gao, Z.L. Wu, Q. Zheng, 3D printing of a tough double-network hydrogel and its use as a scaffold to construct a tissue-like hydrogel

composite, Journal of materials chemistry. B 10 (2022) 468–476. https://doi.org/10.1039/d1tb02465e.

[44] J.P. Gong, Why are double network hydrogels so tough?, Soft Matter 6 (2010) 2583. https://doi.org/10.1039/b924290b.

[45] A. Lee, A.R. Hudson, D.J. Shiwarski, J.W. Tashman, T.J. Hinton, S. Yerneni, J.M. Bliley, P.G. Campbell, A.W. Feinberg, 3D bioprinting of collagen to rebuild components of the human heart, Science (New York, N.Y.) 365 (2019) 482–487. https://doi.org/10.1126/science.aav9051.

[46] D. Chimene, C.W. Peak, J.L. Gentry, J.K. Carrow, L.M. Cross, E. Mondragon, G.B. Cardoso, R. Kaunas, A.K. Gaharwar, Nanoengineered Ionic-Covalent Entanglement (NICE) Bioinks for 3D Bioprinting, ACS applied materials & interfaces 10 (2018) 9957–9968. https://doi.org/10.1021/acsami.7b19808.

[47] A. Schwab, R. Levato, M. D'Este, S. Piluso, D. Eglin, J. Malda, Printability and Shape Fidelity of Bioinks in 3D Bioprinting, Chemical reviews 120 (2020) 11028–11055. https://doi.org/10.1021/acs.chemrev.0c00084.

[48] A. Blaeser, D.F. Duarte Campos, U. Puster, W. Richtering, M.M. Stevens, H. Fischer, Controlling Shear Stress in 3D Bioprinting is a Key Factor to Balance Printing Resolution and Stem Cell Integrity, Advanced healthcare materials 5 (2016) 326–333. https://doi.org/10.1002/adhm.201500677.

[49] L. Ouyang, R. Yao, Y. Zhao, W. Sun, Effect of bioink properties on printability and cell viability for 3D bioplotting of embryonic stem cells, Biofabrication 8 (2016) 35020. https://doi.org/10.1088/1758-5090/8/3/035020.

[50] A. Nadernezhad, J. Groll, Machine Learning Reveals a General Understanding of Printability in Formulations Based on Rheology Additives, Advanced science (Weinheim, Baden-Wurttemberg, Germany) 9 (2022) e2202638. https://doi.org/10.1002/advs.202202638.

[51] L. Quan, D.M. Kalyon, Parallel-Disk Viscometry of a Viscoplastic Hydrogel: Yield Stress and Other Parameters of Shear Viscosity and Wall Slip, Gels (Basel, Switzerland) 8 (2022). https://doi.org/10.3390/gels8040230.

[52] M. Daneshi, A. Pourzahedi, D.M. Martinez, D. Grecov, Characterising wall-slip behaviour of carbopol gels in a fully-developed poiseuille flow, Journal of Non-Newtonian Fluid Mechanics 269 (2019) 65–72. https://doi.org/10.1016/j.jnnfm.2019.06.003.

[53] N. Ashammakhi, S. Ahadian, C. Xu, H. Montazerian, H. Ko, R. Nasiri, N. Barros, A. Khademhosseini, Bioinks and bioprinting technologies to make heterogeneous and biomimetic tissue constructs, Materials today. Bio 1 (2019) 100008. https://doi.org/10.1016/j.mtbio.2019.100008.

[54] S. Lalitha Sridhar, M.C. Schneider, S. Chu, G. de Roucy, S.J. Bryant, F.J. Vernerey, Heterogeneity is key to hydrogel-based cartilage tissue regeneration, Soft Matter 13 (2017) 4841–4855. https://doi.org/10.1039/c7sm00423k.

[55] W. Dai, L. Zhang, Y. Yu, W. Yan, F. Zhao, Y. Fan, C. Cao, Q. Cai, X. Hu, Y. Ao, 3D Bioprinting of Heterogeneous Constructs Providing Tissue-Specific Microenvironment Based on Host–Guest Modulated Dynamic Hydrogel Bioink for Osteochondral Regeneration, Adv. Funct. Mater. 32 (2022) 2200710. https://doi.org/10.1002/adfm.202200710.

[56] S. Babu, F. Albertino, A. Omidinia Anarkoli, L. de Laporte, Controlling Structure with Injectable Biomaterials to Better Mimic Tissue Heterogeneity and Anisotropy, Advanced healthcare materials 10 (2021) e2002221. https://doi.org/10.1002/adhm.202002221.

[57] A.M. Soto, J.T. Koivisto, J.E. Parraga, J. Silva-Correia, J.M. Oliveira, R.L. Reis, M. Kellomäki, J. Hyttinen, E. Figueiras, Optical Projection Tomography Technique for Image Texture and Mass Transport Studies in Hydrogels Based on Gellan Gum, Langmuir the ACS journal of surfaces and colloids 32 (2016) 5173–5182. https://doi.org/10.1021/acs.langmuir.6b00554.

[58] T. Gao, G.J. Gillispie, J.S. Copus, A.K. Pr, Y.-J. Seol, A. Atala, J.J. Yoo, S.J. Lee, Optimization of gelatin-alginate composite bioink printability using rheological parameters: a systematic approach, Biofabrication 10 (2018) 34106. https://doi.org/10.1088/1758-5090/aacdc7.

[59] R.G. Larson, The structure and rheology of complex fluids, Oxford university press, New York, 1999.

[60] A. Forget, A. Blaeser, F. Miessmer, M. Köpf, D.F.D. Campos, N.H. Voelcker, A. Blencowe, H. Fischer, V.P. Shastri, Mechanically Tunable Bioink for 3D Bioprinting of Human Cells, Advanced healthcare materials 6 (2017). https://doi.org/10.1002/adhm.201700255.

[61] D. Ji, J. Kim, Recent Strategies for Strengthening and Stiffening Tough Hydrogels, Adv NanoBio Res 1 (2021) 2100026. https://doi.org/10.1002/anbr.202100026.

[62] J. Lee, S.J. Oh, S.H. An, W.-D. Kim, S.-H. Kim, Machine learning-based design strategy for 3D printable bioink: elastic modulus and yield stress determine printability, Biofabrication 12 (2020) 35018. https://doi.org/10.1088/1758-5090/ab8707.

[63] V. Ozbolat, M. Dey, B. Ayan, A. Povilianskas, M.C. Demirel, I.T. Ozbolat, 3D Printing of PDMS Improves Its Mechanical and Cell Adhesion Properties, ACS biomaterials science & engineering 4 (2018) 682–693. https://doi.org/10.1021/acsbiomaterials.7b00646.

[64] A. Ribeiro, M.M. Blokzijl, R. Levato, C.W. Visser, M. Castilho, W.E. Hennink, T. Vermonden, J. Malda, Assessing bioink shape fidelity to aid material development in 3D bioprinting, Biofabrication 10 (2017) 14102. https://doi.org/10.1088/1758-5090/aa90e2.

[65] N. Paxton, W. Smolan, T. Böck, F. Melchels, J. Groll, T. Jungst, Proposal to assess printability of bioinks for extrusion-based bioprinting and evaluation of rheological properties governing bioprintability, Biofabrication 9 (2017) 44107. https://doi.org/10.1088/1758-5090/aa8dd8.

[66] E.A. Kiyotake, A.W. Douglas, E.E. Thomas, S.L. Nimmo, M.S. Detamore, Development and quantitative characterization of the precursor rheology of hyaluronic acid hydrogels for bioprinting, Acta biomaterialia 95 (2019) 176–187. https://doi.org/10.1016/j.actbio.2019.01.041.

[67] L. Ouyang, J.P.K. Armstrong, Y. Lin, J.P. Wojciechowski, C. Lee-Reeves, D. Hachim, K. Zhou, J.A. Burdick, M.M. Stevens, Expanding and optimizing 3D bioprinting capabilities using complementary network bioinks, Science advances 6 (2020). https://doi.org/10.1126/sciadv.abc5529.

[68] J. Lee, S.J. Oh, S.H. An, W.-D. Kim, S.-H. Kim, Machine learning-based design strategy for 3D printable bioink: elastic modulus and yield stress determine printability, Biofabrication 12 (2020) 35018. https://doi.org/10.1088/1758-5090/ab8707.

[69] W. Hu, F. Martin, R. Jeantet, X.D. Chen, R. Mercadé-Prieto, Micromechanical Characterization of Hydrogels Undergoing Swelling and Dissolution at Alkaline pH, Gels (Basel, Switzerland) 3 (2017). https://doi.org/10.3390/gels3040044.

[70] S. Rattan, L. Li, H.K. Lau, A.J. Crosby, K.L. Kiick, Micromechanical characterization of soft, biopolymeric hydrogels: stiffness, resilience, and failure, Soft Matter 14 (2018) 3478–3489. https://doi.org/10.1039/c8sm00501j.

[71] H.A. Marin-Tapia, L. Romero-Salazar, J.C. Arteaga-Arcos, R. Rosales-Ibáñez, M. Mayorga-Rojas, Micro-mechanical properties of corneal scaffolds from two different bio-models obtained by an efficient chemical decellularization, Journal of the mechanical behavior of biomedical materials 119 (2021) 104510. https://doi.org/10.1016/j.jmbbm.2021.104510.

[72] J. Joshi, S.V. Homburg, A. Ehrmann, Atomic Force Microscopy (AFM) on Biopolymers and Hydrogels for Biotechnological Applications-Possibilities and Limits, Polymers 14 (2022). https://doi.org/10.3390/polym14061267.

[73] J. Hafner, D. Grijalva, A. Ludwig-Husemann, B. Bertels, L. Bensinger, A. Raic, J. Gebauer, C. Oelschlaeger, M. Bastmeyer, K. Bieback, C. Lee-Thedieck, N. Willenbacher, Monitoring matrix remodeling in the cellular microenvironment using microrheology for complex cellular systems, Acta biomaterialia 111 (2020) 254–266. https://doi.org/10.1016/j.actbio.2020.04.053.

[74] J. Roether, S. Bertels, C. Oelschlaeger, M. Bastmeyer, N. Willenbacher, Microstructure, local viscoelasticity and cell culture suitability of 3D hybrid HA/collagen scaffolds, PloS one 13 (2018) e0207397. https://doi.org/10.1371/journal.pone.0207397.

[75] U.A. Khan, C. Oelschlaeger, F.I. Ali, J. Roether, N. Willenbacher, I.A. Hashmi, Structural, macro- and micro-mechanical properties of supramolecular bi-component l-Lysine-sodium tetraphenyl borate based hydrogels, Colloids and Surfaces A: Physicochemical and Engineering Aspects 546 (2018) 366–377. https://doi.org/10.1016/j.colsurfa.2018.02.068.

[76] A. Bashari, A. Rouhani Shirvan, M. Shakeri, Cellulose-based hydrogels for personal care products, Polym Adv Technol 29 (2018) 2853–2867. https://doi.org/10.1002/pat.4290.

[77] H. Khalesi, W. Lu, K. Nishinari, Y. Fang, New insights into food hydrogels with reinforced mechanical properties: A review on innovative strategies, Advances in colloid and interface science 285 (2020) 102278. https://doi.org/10.1016/j.cis.2020.102278.

[78] M.K. Yazdi, V. Vatanpour, A. Taghizadeh, M. Taghizadeh, M.R. Ganjali, M.T. Munir, S. Habibzadeh, M.R. Saeb, M. Ghaedi, Hydrogel membranes: A review, Materials science &

engineering. C, Materials for biological applications 114 (2020) 111023. https://doi.org/10.1016/j.msec.2020.111023.

[79] F.E. Freeman, D.J. Kelly, Tuning Alginate Bioink Stiffness and Composition for Controlled Growth Factor Delivery and to Spatially Direct MSC Fate within Bioprinted Tissues, Scientific reports 7 (2017) 17042. https://doi.org/10.1038/s41598-017-17286-1.

[80] G. Cidonio, M. Glinka, J.I. Dawson, R.O.C. Oreffo, The cell in the ink: Improving biofabrication by printing stem cells for skeletal regenerative medicine, Biomaterials 209 (2019) 10–24. https://doi.org/10.1016/j.biomaterials.2019.04.009.

[81] J. Hafner, C. Oelschlaeger, N. Willenbacher, Microrheology imaging of fiber suspensions - a case study for lyophilized collagen I in HCl solutions, Soft Matter 16 (2020) 9014–9027. https://doi.org/10.1039/d0sm01096k.

[82] M. Vielreicher, S. Schürmann, R. Detsch, M.A. Schmidt, A. Buttgereit, A. Boccaccini, O. Friedrich, Taking a deep look: modern microscopy technologies to optimize the design and functionality of biocompatible scaffolds for tissue engineering in regenerative medicine, Journal of the Royal Society, Interface 10 (2013) 20130263. https://doi.org/10.1098/rsif.2013.0263.

[83] C. Weis, C. Oelschlaeger, D. Dijkstra, M. Ranft, N. Willenbacher, Microstructure, local dynamics, and flow behavior of colloidal suspensions with weak attractive interactions, Scientific reports 6 (2016) 33498. https://doi.org/10.1038/srep33498.

[84] T. Moschakis, Microrheology and particle tracking in food gels and emulsions, Current Opinion in Colloid & Interface Science 18 (2013) 311–323. https://doi.org/10.1016/j.cocis.2013.04.011.

[85] S. Shabaniverki, J.J. Juárez, Characterizing gelatin hydrogel viscoelasticity with diffusing colloidal probe microscopy, Journal of Colloid and Interface Science 497 (2017) 73–82. https://doi.org/10.1016/j.jcis.2017.02.057.

[86] B. Maciel, C. Oelschlaeger, N. Willenbacher, Chain flexibility and dynamics of alginate solutions in different solvents, Colloid Polym Sci 298 (2020) 791–801. https://doi.org/10.1007/s00396-020-04612-9.

[87] W. Hong, G. Xu, X. Ou, W. Sun, T. Wang, Z. Tong, Colloidal probe dynamics in gelatin solution during the sol-gel transition, Soft Matter 14 (2018) 3694–3703. https://doi.org/10.1039/c7sm02556d.

[88] L.-C. Cheng, L.C. Hsiao, P.S. Doyle, Multiple particle tracking study of thermally-gelling nanoemulsions, Soft Matter 13 (2017) 6606–6619. https://doi.org/10.1039/c7sm01191a.

[89] K.M. Schultz, E.M. Furst, Microrheology of biomaterial hydrogelators, Soft Matter 8 (2012) 6198. https://doi.org/10.1039/c2sm25187f.

[90] M. McKenna, D. Shackelford, H. Ferreira Pontes, B. Ball, E. Nance, Multiple Particle Tracking Detects Changes in Brain Extracellular Matrix and Predicts Neurodevelopmental Age, ACS nano 15 (2021) 8559–8573. https://doi.org/10.1021/acsnano.1c00394.

[91] A. Kowalczyk, C. Oelschlaeger, N. Willenbacher, Visualization of micro-scale inhomogeneities in acrylic thickener solutions: A multiple particle tracking study, Polymer 58 (2015) 170–179. https://doi.org/10.1016/j.polymer.2014.12.041.

[92] T.G. Mason, Estimating the viscoelastic moduli of complex fluids using the generalized Stokes-Einstein equation, Rheol Acta 39 (2000) 371–378. https://doi.org/10.1007/s003970000094.

[93] Mason, Weitz, Optical measurements of frequency-dependent linear viscoelastic moduli of complex fluids, Physical review letters 74 (1995) 1250–1253. https://doi.org/10.1103/PhysRevLett.74.1250.

[94] E.R. Weeks, J.C. Crocker, A.C. Levitt, A. Schofield, Da Weitz, Three-dimensional direct imaging of structural relaxation near the colloidal glass transition, Science (New York, N.Y.) 287 (2000) 627–631. https://doi.org/10.1126/science.287.5453.627.

[95] J. Xu, S.X. Liu, V.M. Boddu, Micro-rheological and micro-heterogeneity properties of soluble glutinous rice starch (SGRS) solutions studied by diffusing wave spectroscopy (DWS), Food Measure 13 (2019) 2822–2827. https://doi.org/10.1007/s11694-019-00202-8.

[96] M. Pilavtepe, S.M. Recktenwald, R. Schuhmann, K. Emmerich, N. Willenbacher, Macro- and microscale structure formation and aging in different arrested states of Laponite dispersions, Journal of Rheology 62 (2018) 593–605. https://doi.org/10.1122/1.5001382.

[97] P. Pawelzyk, N. Mücke, H. Herrmann, N. Willenbacher, Attractive interactions among intermediate filaments determine network mechanics in vitro, PloS one 9 (2014) e93194. https://doi.org/10.1371/journal.pone.0093194.

[98] N. Willenbacher, C. Oelschlaeger, M. Schopferer, P. Fischer, F. Cardinaux, F. Scheffold, Broad bandwidth optical and mechanical rheometry of wormlike micelle solutions, Physical review letters 99 (2007) 68302. https://doi.org/10.1103/PhysRevLett.99.068302.

[99] C. Oelschlaeger, M. Schopferer, F. Scheffold, N. Willenbacher, Linear-to-branched micelles transition: a rheometry and diffusing wave spectroscopy (DWS) study, Langmuir the ACS journal of surfaces and colloids 25 (2009) 716–723. https://doi.org/10.1021/la802323x.

[100] N. Willenbacher, C. Oelschlaeger, Dynamics and structure of complex fluids from high frequency mechanical and optical rheometry, Current Opinion in Colloid & Interface Science 12 (2007) 43–49. https://doi.org/10.1016/j.cocis.2007.03.004.

[101] C. Oelschlaeger, M. Cota Pinto Coelho, N. Willenbacher, Chain flexibility and dynamics of polysaccharide hyaluronan in entangled solutions: a high frequency rheology and diffusing wave spectroscopy study, Biomacromolecules 14 (2013) 3689–3696. https://doi.org/10.1021/bm4010436.

[102] D.C. Morse, Viscoelasticity of tightly entangled solutions of semiflexible polymers, Phys. Rev. E 58 (1998) R1237-R1240. https://doi.org/10.1103/PhysRevE.58.R1237.

[103] F. Gittes, F.C. MacKintosh, Dynamic shear modulus of a semiflexible polymer network, Phys. Rev. E 58 (1998) R1241-R1244. https://doi.org/10.1103/PhysRevE.58.R1241.

[104]J. Lee, B. Song, R. Subbiah, J.J. Chung, U.H. Choi, K. Park, S.-H. Kim, S.J. Oh, Effect of chain flexibility on cell adhesion: Semi-flexible model-based analysis of cell adhesion to hydrogels, Scientific reports 9 (2019) 2463. https://doi.org/10.1038/s41598-019-38951-7.

[105]Y. Fang, Y. Guo, T. Liu, R. Xu, S. Mao, X. Mo, T. Zhang, L. Ouyang, Z. Xiong, W. Sun, Advances in 3D Bioprinting, Chinese Journal of Mechanical Engineering: Additive Manufacturing Frontiers 1 (2022) 100011. https://doi.org/10.1016/j.cjmeam.2022.100011.

[106]K.A. Deo, K.A. Singh, C.W. Peak, D.L. Alge, A.K. Gaharwar, Bioprinting 101: Design, Fabrication, and Evaluation of Cell-Laden 3D Bioprinted Scaffolds, Tissue engineering. Part A 26 (2020) 318–338. https://doi.org/10.1089/ten.tea.2019.0298.

[107]S. Naghieh, X. Chen, Printability-A key issue in extrusion-based bioprinting, Journal of pharmaceutical analysis 11 (2021) 564–579. https://doi.org/10.1016/j.jpha.2021.02.001.

[108]H.-Q. Xu, J.-C. Liu, Z.-Y. Zhang, C.-X. Xu, A review on cell damage, viability, and functionality during 3D bioprinting, Military Medical Research 9 (2022) 70. https://doi.org/10.1186/s40779-022-00429-5.

[109]Y. Gu, A. Forget, V.P. Shastri, Biobridge: An Outlook on Translational Bioinks for 3D Bioprinting, Advanced science (Weinheim, Baden-Wurttemberg, Germany) 9 (2022) e2103469. https://doi.org/10.1002/advs.202103469.

[110]W. Liu, M.A. Heinrich, Y. Zhou, A. Akpek, N. Hu, X. Liu, X. Guan, Z. Zhong, X. Jin, A. Khademhosseini, Y.S. Zhang, Extrusion Bioprinting of Shear-Thinning Gelatin Methacryloyl Bioinks, Advanced healthcare materials 6 (2017). https://doi.org/10.1002/adhm.201601451.

[111]T. Billiet, E. Gevaert, T. de Schryver, M. Cornelissen, P. Dubruel, The 3D printing of gelatin methacrylamide cell-laden tissue-engineered constructs with high cell viability, Biomaterials 35 (2014) 49–62. https://doi.org/10.1016/j.biomaterials.2013.09.078.

[112]Y.A. Çengel, J.M. Cimbala, Fluid mechanics: Fundamentals and applications, McGraw-Hill, Boston, 2006.

[113]I. Donati, S. Paoletti, Material Properties of Alginates 13 1–53. https://doi.org/10.1007/978-3-540-92679-5_1.

[114]K.Y. Lee, D.J. Mooney, Alginate: properties and biomedical applications, Progress in polymer science 37 (2012) 106–126. https://doi.org/10.1016/j.progpolymsci.2011.06.003.

[115]P.S. Gungor-Ozkerim, I. Inci, Y.S. Zhang, A. Khademhosseini, M.R. Dokmeci, Bioinks for 3D bioprinting: an overview, Biomaterials science 6 (2018) 915–946. https://doi.org/10.1039/c7bm00765e.

[116]L. Li, Y. Fang, R. Vreeker, I. Appelqvist, E. Mendes, Reexamining the egg-box model in calcium-alginate gels with X-ray diffraction, Biomacromolecules 8 (2007) 464–468. https://doi.org/10.1021/bm060550a.

[117]A. Dodero, S. Vicini, M. Alloisio, M. Castellano, Sodium alginate solutions: correlation between rheological properties and spinnability, J Mater Sci 54 (2019) 8034–8046. https://doi.org/10.1007/s10853-019-03446-3.

[118]C. Rodríguez-Rivero, L. Hilliou, E.M. Del Martín Valle, M.A. Galán, Rheological characterization of commercial highly viscous alginate solutions in shear and extensional flows, Rheol Acta 53 (2014) 559–570. https://doi.org/10.1007/s00397-014-0780-4.

[119]S. Fu, A. Thacker, D.M. Sperger, R.L. Boni, I.S. Buckner, S. Velankar, E.J. Munson, L.H. Block, Relevance of rheological properties of sodium alginate in solution to calcium alginate gel properties, AAPS PharmSciTech 12 (2011) 453–460. https://doi.org/10.1208/s12249-011-9587-0.

[120]C.A. Bonino, M.D. Krebs, C.D. Saquing, S. in Jeong, K.L. Shearer, E. Alsberg, S.A. Khan, Electrospinning alginate-based nanofibers: From blends to crosslinked low molecular weight alginate-only systems, Carbohydrate Polymers 85 (2011) 111–119. https://doi.org/10.1016/j.carbpol.2011.02.002.

[121]H. Storz, U. Zimmermann, H. Zimmermann, W.-M. Kulicke, Viscoelastic properties of ultra-high viscosity alginates, Rheol Acta 49 (2010) 155–167. https://doi.org/10.1007/s00397-009-0400-x.

[122]A.V. Dobrynin, R.H. Colby, M. Rubinstein, Scaling Theory of Polyelectrolyte Solutions, Macromolecules 28 (1995) 1859–1871. https://doi.org/10.1021/ma00110a021.

[123]M.M. Cross, Rheology of non-Newtonian fluids: A new flow equation for pseudoplastic systems, Journal of Colloid Science 20 (1965) 417–437. https://doi.org/10.1016/0095-8522(65)90022-X.

[124]H.A. Barnes, Shear-Thickening ("Dilatancy") in Suspensions of Nonaggregating Solid Particles Dispersed in Newtonian Liquids, Journal of Rheology 33 (1989) 329–366. https://doi.org/10.1122/1.550017.

[125]N. Willenbacher, C. Oelschlaeger, M. Schopferer, P. Fischer, F. Cardinaux, F. Scheffold, Broad bandwidth optical and mechanical rheometry of wormlike micelle solutions, Physical review letters 99 (2007) 68302. https://doi.org/10.1103/PhysRevLett.99.068302.

[126]H. Zhang, H. Wang, J. Wang, R. Guo, Q. Zhang, The effect of ionic strength on the viscosity of sodium alginate solution, Polym. Adv. Technol. 12 (2001) 740–745. https://doi.org/10.1002/pat.97.

[127]I. Donati, A. Coslovi, A. Gamini, G. Skjåk-Braek, A. Vetere, C. Campa, S. Paoletti, Galactose-substituted alginate 2: conformational aspects, Biomacromolecules 5 (2004) 186–196. https://doi.org/10.1021/bm030063k.

[128]F.G.D. Baños, A.I. Díez Peña, J.G. Hernánez Cifre, M.C. López Martínez, A. Ortega, J. La García de Torre, Influence of ionic strength on the flexibility of alginate studied by size exclusion chromatography, Carbohydrate Polymers 102 (2014) 223–230. https://doi.org/10.1016/j.carbpol.2013.11.023.

[129]I.M.N. Vold, K.A. Kristiansen, B.E. Christensen, A study of the chain stiffness and extension of alginates, in vitro epimerized alginates, and periodate-oxidized alginates using size-exclusion chromatography combined with light scattering and viscosity detectors, Biomacromolecules 7 (2006) 2136–2146. https://doi.org/10.1021/bm060099n.

[130]B.T. Stokke, D.A. Brant, The reliability of wormlike polysaccharide chain dimensions estimated from electron micrographs, Biopolymers 30 (1990) 1161–1181. https://doi.org/10.1002/bip.360301303.

[131]B.T. Stokke, A. Elgsaeter, G. Skjåk-Braek, O. Smidsrød, The molecular size and shape of xanthan, xylinan, bronchial mucin, alginate, and amylose as revealed by electron microscopy, Carbohydrate research 160 (1987) 13–28. https://doi.org/10.1016/0008-6215(87)80300-2.

[132]I. Braccini, R.P. Grasso, S. Pérez, Conformational and configurational features of acidic polysaccharides and their interactions with calcium ions: a molecular modeling investigation, Carbohydrate research 317 (1999) 119–130. https://doi.org/10.1016/S0008-6215(99)00062-2.

[133]H. Hecht, S. Srebnik, Structural Characterization of Sodium Alginate and Calcium Alginate, Biomacromolecules 17 (2016) 2160–2167. https://doi.org/10.1021/acs.biomac.6b00378.

[134]F. Avaltroni, M. Seijo, S. Ulrich, S. Stoll, K.J. Wilkinson, Conformational changes and aggregation of alginic acid as determined by fluorescence correlation spectroscopy, Biomacromolecules 8 (2007) 106–112. https://doi.org/10.1021/bm060655d.

[135]E. Josef, H. Bianco-Peled, Conformation of a natural polyelectrolyte in semidilute solutions with no added salt, Soft Matter 8 (2012) 9156–9165. https://doi.org/10.1039/C2SM25733E.

[136]R.H. Colby, M. Rubinstein, M. Daoud, Hydrodynamics of polymer solutions via two-parameter scaling, J. Phys. II France 4 (1994) 1299–1310. https://doi.org/10.1051/jp2:1994201.

[137]J.J. Crassous, R. Régisser, M. Ballauff, N. Willenbacher, Characterization of the viscoelastic behavior of complex fluids using the piezoelastic axial vibrator, Journal of Rheology 49 (2005) 851–863. https://doi.org/10.1122/1.1917843.

[138]W. Oswald, N. Willenbacher, Controlling the elongational flow behavior of complex shear-thinning fluids without affecting shear viscosity, Rheol Acta 58 (2019) 687–698. https://doi.org/10.1007/s00397-019-01170-y.

[139]C. Oelschlaeger, M. Schopferer, F. Scheffold, N. Willenbacher, Linear-to-branched micelles transition: a rheometry and diffusing wave spectroscopy (DWS) study, Langmuir the ACS journal of surfaces and colloids 25 (2009) 716–723. https://doi.org/10.1021/la802323x.

[140]Microscale Diagnostic Techniques, 1st ed., Springer Berlin Heidelberg; Imprint: Springer, Berlin, Heidelberg, 2005.

[141]T.A. Waigh, Microrheology of complex fluids, Rep. Prog. Phys. 68 (2005) 685–742. https://doi.org/10.1088/0034-4885/68/3/R04.

[142]J.C. Crocker, D.G. Grier, Methods of Digital Video Microscopy for Colloidal Studies, Journal of Colloid and Interface Science 179 (1996) 298–310. https://doi.org/10.1006/jcis.1996.0217.

[143]E.R. Weeks, J.C. Crocker, A.C. Levitt, A. Schofield, Da Weitz, Three-dimensional direct imaging of structural relaxation near the colloidal glass transition, Science (New York, N.Y.) 287 (2000) 627–631. https://doi.org/10.1126/science.287.5453.627.

[144]A. Kowalczyk, C. Oelschlaeger, N. Willenbacher, Tracking errors in 2D multiple particle tracking microrheology, Meas. Sci. Technol. 26 (2015) 15302. https://doi.org/10.1088/0957-0233/26/1/015302.

[145]M.E. Di Cocco, C. Bianchetti, F. Chiellini, 1H NMR Studies of Alginate Interactions with Amino Acids, Journal of Bioactive and Compatible Polymers 18 (2003) 283–296. https://doi.org/10.1177/088391103037015.

[146]C. Esquenet, E. Buhler, Aggregation Behavior in Semidilute Rigid and Semirigid Polysaccharide Solutions, Macromolecules 35 (2002) 3708–3716. https://doi.org/10.1021/ma012047q.

[147]A. Charlot, R. Auzély-Velty, Novel Hyaluronic Acid Based Supramolecular Assemblies Stabilized by Multivalent Specific Interactions: Rheological Behavior in Aqueous Solution, Macromolecules 40 (2007) 9555–9563. https://doi.org/10.1021/ma071631h.

[148]T. Odijk, Polyelectrolytes near the rod limit, J. Polym. Sci. Polym. Phys. Ed. 15 (1977) 477–483. https://doi.org/10.1002/pol.1977.180150307.

[149]J. Skolnick, M. Fixman, Electrostatic Persistence Length of a Wormlike Polyelectrolyte, Macromolecules 10 (1977) 944–948. https://doi.org/10.1021/ma60059a011.

[150]K. Duval, H. Grover, L.-H. Han, Y. Mou, A.F. Pegoraro, J. Fredberg, Z. Chen, Modeling Physiological Events in 2D vs. 3D Cell Culture, Physiology (Bethesda, Md.) 32 (2017) 266–277. https://doi.org/10.1152/physiol.00036.2016.

[151]W.L. Ng, J.M. Lee, M. Zhou, Y.-W. Chen, K.-X.A. Lee, W.Y. Yeong, Y.-F. Shen, Vat polymerization-based bioprinting-process, materials, applications and regulatory challenges, Biofabrication 12 (2020) 22001. https://doi.org/10.1088/1758-5090/ab6034.

[152]X. Li, B. Liu, B. Pei, J. Chen, D. Zhou, J. Peng, X. Zhang, W. Jia, T. Xu, Inkjet Bioprinting of Biomaterials, Chemical reviews 120 (2020) 10793–10833. https://doi.org/10.1021/acs.chemrev.0c00008.

[153]D. Chimene, R. Kaunas, A.K. Gaharwar, Hydrogel Bioink Reinforcement for Additive Manufacturing: A Focused Review of Emerging Strategies, Advanced materials (Deerfield Beach, Fla.) 32 (2020) e1902026. https://doi.org/10.1002/adma.201902026.

[154]J. Li, C. Wu, P.K. Chu, M. Gelinsky, 3D printing of hydrogels: Rational design strategies and emerging biomedical applications, Materials Science and Engineering: R: Reports 140 (2020) 100543. https://doi.org/10.1016/j.mser.2020.100543.

[155]G. Poologasundarampillai, A. Haweet, S.N. Jayash, G. Morgan, J.E. Moore, A. Candeo, Real-time imaging and analysis of cell-hydrogel interplay within an extrusion-bioprinting capillary, Bioprinting 23 (2021) e00144. https://doi.org/10.1016/j.bprint.2021.e00144.

[156]S.-Q. Wang, S. Ravindranath, P.E. Boukany, Homogeneous Shear, Wall Slip, and Shear Banding of Entangled Polymeric Liquids in Simple-Shear Rheometry: A Roadmap of Nonlinear Rheology, Macromolecules 44 (2011) 183–190. https://doi.org/10.1021/ma101223q.

[157]C. Xu, M. Fies, N. Willenbacher, Impact of Wall Slip on Screen Printing of Front-Side Silver Pastes for Silicon Solar Cells, IEEE J. Photovoltaics 7 (2017) 129–135. https://doi.org/10.1109/JPHOTOV.2016.2626147.

[158]B. Stoimenov, V. Fridrici, P. Kapsa, H. Kosukegawa, M. Ohta, Bioengineering Materials and Conditions for Obtaining Low Friction with PVA Hydrogels, Tribology Online 8 (2013) 140–152. https://doi.org/10.2474/trol.8.140.

[159]J. Leppiniemi, P. Lahtinen, A. Paajanen, R. Mahlberg, S. Metsä-Kortelainen, T. Pinomaa, H. Pajari, I. Vikholm-Lundin, P. Pursula, V.P. Hytönen, 3D-Printable Bioactivated Nanocellulose-Alginate Hydrogels, ACS applied materials & interfaces 9 (2017) 21959–21970. https://doi.org/10.1021/acsami.7b02756.

[160]S. Sakai, A. Yoshii, S. Sakurai, K. Horii, O. Nagasuna, Silk fibroin nanofibers: a promising ink additive for extrusion three-dimensional bioprinting, Materials today. Bio 8 (2020) 100078. https://doi.org/10.1016/j.mtbio.2020.100078.

[161]J. Emmermacher, D. Spura, J. Cziommer, D. Kilian, T. Wollborn, U. Fritsching, J. Steingroewer, T. Walther, M. Gelinsky, A. Lode, Engineering considerations on extrusion-based bioprinting: interactions of material behavior, mechanical forces and cells in the printing needle, Biofabrication 12 (2020) 25022. https://doi.org/10.1088/1758-5090/ab7553.

[162]J. Göhl, K. Markstedt, A. Mark, K. Håkansson, P. Gatenholm, F. Edelvik, Simulations of 3D bioprinting: predicting bioprintability of nanofibrillar inks, Biofabrication 10 (2018) 34105. https://doi.org/10.1088/1758-5090/aac872.

[163]S.J. Müller, E. Mirzahossein, E.N. Iftekhar, C. Bächer, S. Schrüfer, D.W. Schubert, B. Fabry, S. Gekle, Flow and hydrodynamic shear stress inside a printing needle during biofabrication, PloS one 15 (2020) e0236371. https://doi.org/10.1371/journal.pone.0236371.

[164]M.G. Li, X.Y. Tian, X.B. Chen, Modeling of Flow Rate, Pore Size, and Porosity for the Dispensing-Based Tissue Scaffolds Fabrication, Journal of Manufacturing Science and Engineering 131 (2009). https://doi.org/10.1115/1.3123331.

[165]M. Sarker, X.B. Chen, Modeling the Flow Behavior and Flow Rate of Medium Viscosity Alginate for Scaffold Fabrication With a Three-Dimensional Bioplotter, Journal of Manufacturing Science and Engineering 139 (2017). https://doi.org/10.1115/1.4036226.

[166]A. Yoshimura, R.K. Prud'homme, Wall Slip Corrections for Couette and Parallel Disk Viscometers, Journal of Rheology 32 (1988) 53–67. https://doi.org/10.1122/1.549963.

[167]P. Coussot, Rheophysics, Springer International Pu, [Place of publication not identified], 2016.

[168]H.M. Shewan, J.R. Stokes, M. Cloitre, Particle-wall tribology of slippery hydrogel particle suspensions, Soft Matter 13 (2017) 2099–2106. https://doi.org/10.1039/c6sm01775d.

[169]P. Coussot, Rheometry of pastes, suspensions, and granular materials: Applications in industry and environment, Wiley, Hoboken, N.J, 2010.

[170]T.G. Mezger, The rheology handbook: For users of rotational and oscillatory rheometers, 2nd ed., Vincentz Network, Hannover, op. 2006.

[171]M. Mooney, Explicit Formulas for Slip and Fluidity, Journal of Rheology 2 (1931) 210–222. https://doi.org/10.1122/1.2116364.

[172]R. Matjie, S. Zhang, Q. Zhao, N. Mabuza, J.R. Bunt, Tailored surface energy of stainless steel plate coupons to reduce the adhesion of aluminium silicate deposit, Fuel 181 (2016) 573–578. https://doi.org/10.1016/j.fuel.2016.04.105.

[173]P.F. Rios, H. Dodiuk, S. Kenig, S. McCarthy, A. Dotan, The effect of polymer surface on the wetting and adhesion of liquid systems, Journal of Adhesion Science and Technology 21 (2007) 227–241. https://doi.org/10.1163/156856107780684567.

[174]K. Nayebzadeh, J. Chen, E. Dickinson, T. Moschakis, Surface structure smoothing effect of polysaccharide on a heat-set protein particle gel, Langmuir the ACS journal of surfaces and colloids 22 (2006) 8873–8880. https://doi.org/10.1021/la060419o.

[175]J.M. Lee, W.Y. Yeong, A preliminary model of time-pressure dispensing system for bioprinting based on printing and material parameters, Virtual and Physical Prototyping 10 (2015) 3–8. https://doi.org/10.1080/17452759.2014.979557.

[176]E.M. Ahmed, Hydrogel: Preparation, characterization, and applications: A review, Journal of advanced research 6 (2015) 105–121. https://doi.org/10.1016/j.jare.2013.07.006.

[177]G.D. Nicodemus, S.J. Bryant, Cell encapsulation in biodegradable hydrogels for tissue engineering applications, Tissue engineering. Part B, Reviews 14 (2008) 149–165. https://doi.org/10.1089/ten.teb.2007.0332.

[178]M. Villiou, J.I. Paez, A. Del Campo, Photodegradable Hydrogels for Cell Encapsulation and Tissue Adhesion, ACS applied materials & interfaces 12 (2020) 37862–37872. https://doi.org/10.1021/acsami.0c08568.

[179]E. Caló, V.V. Khutoryanskiy, Biomedical applications of hydrogels: A review of patents and commercial products, European Polymer Journal 65 (2015) 252–267. https://doi.org/10.1016/j.eurpolymj.2014.11.024.

[180]G. Chen, W. Tang, X. Wang, X. Zhao, C. Chen, Z. Zhu, Applications of Hydrogels with Special Physical Properties in Biomedicine, Polymers 11 (2019). https://doi.org/10.3390/polym11091420.

[181]S. Correa, A.K. Grosskopf, H. Lopez Hernandez, D. Chan, A.C. Yu, L.M. Stapleton, E.A. Appel, Translational Applications of Hydrogels, Chemical reviews 121 (2021) 11385–11457. https://doi.org/10.1021/acs.chemrev.0c01177.

[182]A. Herrmann, R. Haag, U. Schedler, Hydrogels and Their Role in Biosensing Applications, Advanced healthcare materials 10 (2021) e2100062. https://doi.org/10.1002/adhm.202100062.

[183]M. Klein, E. Poverenov, Natural biopolymer-based hydrogels for use in food and agriculture, Journal of the science of food and agriculture 100 (2020) 2337–2347. https://doi.org/10.1002/jsfa.10274.

[184]T.J. Gutiérrez, Polymers for Agri-Food Applications, Springer International Publishing, Cham, 2019.

[185]S. Bhattacharya, R. Shunmugam, Polymer based gels and their applications in remediation of dyes from textile effluents, Journal of Macromolecular Science, Part A 57 (2020) 906–926. https://doi.org/10.1080/10601325.2020.1782229.

[186]S.-L. Loo, L. Vásquez, A. Athanassiou, D. Fragouli, Polymeric Hydrogels—A Promising Platform in Enhancing Water Security for a Sustainable Future, Adv Materials Inter 8 (2021) 2100580. https://doi.org/10.1002/admi.202100580.

[187]M.A. Cerqueira, L.H. Fasolin, C.S.F. Picone, L.M. Pastrana, R.L. Cunha, A.A. Vicente, Structural and mechanical properties of organogels: Role of oil and gelator molecular structure, Food research international (Ottawa, Ont.) 96 (2017) 161–170. https://doi.org/10.1016/j.foodres.2017.03.021.

[188]R.M. Martinez, C. Rosado, M.V.R. Velasco, S.C.S. Lannes, A.R. Baby, Main features and applications of organogels in cosmetics, International journal of cosmetic science 41 (2019) 109–117. https://doi.org/10.1111/ics.12519.

[189]Y. Seida, H. Tokuyama, Hydrogel Adsorbents for the Removal of Hazardous Pollutants-Requirements and Available Functions as Adsorbent, Gels (Basel, Switzerland) 8 (2022). https://doi.org/10.3390/gels8040220.

[190]J. Jang, Y.-J. Seol, H.J. Kim, J. Kundu, S.W. Kim, D.-W. Cho, Effects of alginate hydrogel cross-linking density on mechanical and biological behaviors for tissue engineering, Journal of the mechanical behavior of biomedical materials 37 (2014) 69–77. https://doi.org/10.1016/j.jmbbm.2014.05.004.

[191]T. Birman, D. Seliktar, Injectability of Biosynthetic Hydrogels: Consideration for Minimally Invasive Surgical Procedures and 3D Bioprinting, Adv. Funct. Mater. 31 (2021) 2100628. https://doi.org/10.1002/adfm.202100628.

[192]M. Guvendiren, H.D. Lu, J.A. Burdick, Shear-thinning hydrogels for biomedical applications, Soft Matter 8 (2012) 260–272. https://doi.org/10.1039/c1sm06513k.

[193]A. Raza, M. Mumtaz, U. Hayat, N. Hussain, M.A. Ghauri, M. Bilal, H.M. Iqbal, Recent advancements in extrudable gel-based bioinks for biomedical settings, Journal of Drug Delivery Science and Technology 75 (2022) 103697. https://doi.org/10.1016/j.jddst.2022.103697.

[194]Y. Wang, R.K. Kankala, K. Zhu, S.-B. Wang, Y.S. Zhang, A.-Z. Chen, Coaxial Extrusion of Tubular Tissue Constructs Using a Gelatin/GelMA Blend Bioink, ACS biomaterials science & engineering 5 (2019) 5514–5524. https://doi.org/10.1021/acsbiomaterials.9b00926.

[195]F.-F. Cai, S. Heid, A.R. Boccaccini, Potential of Laponite® incorporated oxidized alginate-gelatin (ADA-GEL) composite hydrogels for extrusion-based 3D printing, Journal of biomedical materials research. Part B, Applied biomaterials 109 (2021) 1090–1104. https://doi.org/10.1002/jbm.b.34771.

[196]F. Cilurzo, F. Selmin, P. Minghetti, M. Adami, E. Bertoni, S. Lauria, L. Montanari, Injectability Evaluation: An Open Issue, AAPS PharmSciTech 12 (2011) 604–609. https://doi.org/10.1208/s12249-011-9625-y.

[197]C. Xu, G. Dai, Y. Hong, Recent advances in high-strength and elastic hydrogels for 3D printing in biomedical applications, Acta biomaterialia 95 (2019) 50–59. https://doi.org/10.1016/j.actbio.2019.05.032.

[198]M. Rubinstein, S. Panyukov, Nonaffine Deformation and Elasticity of Polymer Networks, Macromolecules 30 (1997) 8036–8044. https://doi.org/10.1021/ma970364k.

[199]A. Basu, Q. Wen, X. Mao, T.C. Lubensky, P.A. Janmey, A.G. Yodh, Nonaffine Displacements in Flexible Polymer Networks, Macromolecules 44 (2011) 1671–1679. https://doi.org/10.1021/ma1026803.

[200]R. Bansil, J.P. Celli, J.M. Hardcastle, B.S. Turner, The Influence of Mucus Microstructure and Rheology in Helicobacter pylori Infection, Frontiers in immunology 4 (2013) 310. https://doi.org/10.3389/fimmu.2013.00310.

[201]J. Mewis, N.J. Wagner, Colloidal Suspension Rheology, University Press, Cambridge, United Kingdom, 2012.

[202]E. Koos, N. Willenbacher, Capillary forces in suspension rheology, Science (New York, N.Y.) 331 (2011) 897–900. https://doi.org/10.1126/science.1199243.

[203]F. Pignon, A. Magnin, J.-M. Piau, B. Cabane, P. Lindner, O. Diat, Yield stress thixotropic clay suspension: Investigations of structure by light, neutron, and x-ray scattering, Phys. Rev. E 56 (1997) 3281–3289. https://doi.org/10.1103/PhysRevE.56.3281.

[204]B. Ruzicka, E. Zaccarelli, A fresh look at the Laponite phase diagram, Soft Matter 7 (2011) 1268. https://doi.org/10.1039/c0sm00590h.

[205]C. Oelschlaeger, J. Marten, F. Péridont, N. Willenbacher, Imaging of the microstructure of Carbopol dispersions and correlation with their macroelasticity: A micro- and macrorheological study, Journal of Rheology 66 (2022) 749–760. https://doi.org/10.1122/8.0000452.

[206]C.K. Kuo, P.X. Ma, Ionically crosslinked alginate hydrogels as scaffolds for tissue engineering: Part 1. Structure, gelation rate and mechanical properties, Biomaterials 22 (2001) 511–521. https://doi.org/10.1016/S0142-9612(00)00201-5.

[207]A.M. Comey, A Dictionary of Chemical Solubilities: Inorganic, McMillan & Co., New York, 1921.

[208]W.H. WALTON, Feret's Statistical Diameter as a Measure of Particle Size, Nature 162 (1948) 329–330. https://doi.org/10.1038/162329b0.

[209]D. Larobina, L. Cipelletti, Hierarchical cross-linking in physical alginate gels: a rheological and dynamic light scattering investigation, Soft Matter 9 (2013) 10005. https://doi.org/10.1039/c3sm52006d.

[210]G. Skjåk-Bræk, H. Grasdalen, O. Smidsrød, Inhomogeneous polysaccharide ionic gels, Carbohydrate Polymers 10 (1989) 31–54. https://doi.org/10.1016/0144-8617(89)90030-1.

[211]K. Ingar Draget, K. Østgaard, O. Smidsrød, Homogeneous alginate gels: A technical approach, Carbohydrate Polymers 14 (1990) 159–178. https://doi.org/10.1016/0144-8617(90)90028-Q.

[212]C. Oelschlaeger, F. Bossler, N. Willenbacher, Synthesis, Structural and Micromechanical Properties of 3D Hyaluronic Acid-Based Cryogel Scaffolds, Biomacromolecules 17 (2016) 580–589. https://doi.org/10.1021/acs.biomac.5b01529.

[213]N. Golafshan, R. Rezahasani, M. Tarkesh Esfahani, M. Kharaziha, S.N. Khorasani, Nanohybrid hydrogels of laponite: PVA-Alginate as a potential wound healing material, Carbohydrate Polymers 176 (2017) 392–401. https://doi.org/10.1016/j.carbpol.2017.08.070.

[214]M.S. Islam, M.R. Karim, Fabrication and characterization of poly(vinyl alcohol)/alginate blend nanofibers by electrospinning method, Colloids and Surfaces A: Physicochemical and Engineering Aspects 366 (2010) 135–140. https://doi.org/10.1016/j.colsurfa.2010.05.038.

[215]Q. Wei, R. Yang, D. Sun, J. Zhou, M. Li, Y. Zhang, Y. Wang, Design and evaluation of sodium alginate/polyvinyl alcohol blend hydrogel for 3D bioprinting cartilage scaffold: molecular dynamics simulation and experimental method, Journal of Materials Research and Technology 17 (2022) 66–78. https://doi.org/10.1016/j.jmrt.2021.12.130.

[216]S. Alberti, A. Gladfelter, T. Mittag, Considerations and Challenges in Studying Liquid-Liquid Phase Separation and Biomolecular Condensates, Cell 176 (2019) 419–434. https://doi.org/10.1016/j.cell.2018.12.035.

[217]C. Fernández-Rico, T. Sai, A. Sicher, R.W. Style, E.R. Dufresne, Putting the Squeeze on Phase Separation, JACS Au 2 (2022) 66–73. https://doi.org/10.1021/jacsau.1c00443.

[218]S. Jabbari-Farouji, H. Tanaka, G.H. Wegdam, D. Bonn, Multiple nonergodic disordered states in Laponite suspensions: a phase diagram, Physical review. E, Statistical, nonlinear, and soft matter physics 78 (2008) 61405. https://doi.org/10.1103/PhysRevE.78.061405.

[219]L. Li, L. Harnau, S. Rosenfeldt, M. Ballauff, Effective interaction of charged platelets in aqueous solution: investigations of colloid laponite suspensions by static light scattering and small-angle x-ray scattering, Physical review. E, Statistical, nonlinear, and soft matter physics 72 (2005) 51504. https://doi.org/10.1103/PhysRevE.72.051504.

[220]T.B. Becher, C.B. Braga, D.L. Bertuzzi, M.D. Ramos, A. Hassan, F.N. Crespilho, C. Ornelas, The structure-property relationship in LAPONITE® materials: from Wigner glasses to strong self-healing hydrogels formed by non-covalent interactions, Soft Matter 15 (2019) 1278–1289. https://doi.org/10.1039/c8sm01965g.

[221]A. Sheikhi, S. Afewerki, R. Oklu, A.K. Gaharwar, A. Khademhosseini, Effect of ionic strength on shear-thinning nanoclay-polymer composite hydrogels, Biomaterials science 6 (2018) 2073–2083. https://doi.org/10.1039/C8BM00469B.

[222]F. Xie, C. Boyer, V. Gaborit, T. Rouillon, J. Guicheux, J.-F. Tassin, V. Geoffroy, G. Réthoré, P. Weiss, A Cellulose/Laponite Interpenetrated Polymer Network (IPN) Hydrogel: Controllable Double-Network Structure with High Modulus, Polymers 10 (2018). https://doi.org/10.3390/polym10060634.

[223]M. Ghadiri, W. Chrzanowski, W.H. Lee, A. Fathi, F. Dehghani, R. Rohanizadeh, Physico-chemical, mechanical and cytotoxicity characterizations of Laponite®/alginate nanocomposite, Applied Clay Science 85 (2013) 64–73. https://doi.org/10.1016/j.clay.2013.08.049.

[224]D.M. Knapp, V.H. Barocas, A.G. Moon, K. Yoo, L.R. Petzold, R.T. Tranquillo, Rheology of reconstituted type I collagen gel in confined compression, Journal of Rheology 41 (1997) 971–993. https://doi.org/10.1122/1.550817.

[225]Z. Xing, H. Lu, Y.Q. Fu, Local conservation law of rubber elasticity in hydrogel networks undergoing microphase separation and toughening, Polymer 222 (2021) 123656. https://doi.org/10.1016/j.polymer.2021.123656.

[226]S.L. Vega, M.Y. Kwon, J.A. Burdick, Recent Advances In Hydrogels For Cartilage Tissue EngineeringRecent Advances In Hydrogels For Cartilage Tissue Engineering, European Cells and Materials 33 (2017) 59–75.

[227]A. Kumar, S.S. Han, PVA-based hydrogels for tissue engineering: A review, International Journal of Polymeric Materials and Polymeric Biomaterials 66(4) (2017) 159–182.

[228]H. Kim, G.H. Yang, C.H. Choi, Y.S. Cho, G. Kim, Gelatin/PVA scaffolds fabricated using a 3D-printing process employed with a low-temperature plate for hard tissue regeneration: Fabrication and characterizations, International journal of biological macromolecules 120 (2018) 119–127. https://doi.org/10.1016/j.ijbiomac.2018.07.159.

[229]E. Hago, X. Li, Interpenetrating Polymer Network Hydrogels Based on Gelatin and PVA by Biocompatible Approaches: Synthesis and Characterization, Advances in Material Science and Engineering (2013).

[230]T. Miao, E.J. Miller, C. McKenzie, R.A. Oldinski, Physically crosslinked polyvinyl alcohol and gelatin interpenetrating polymer network theta-gels for cartilage regeneration, Journal of materials chemistry. B 3 (2015) 9242–9249. https://doi.org/10.1039/c5tb00989h.

[231]Y. Jiang, N. Krishnan, J. Heo, R.H. Fang, L. Zhang, Nanoparticle-hydrogel superstructures for biomedical applications, Journal of controlled release official journal of the Controlled Release Society 324 (2020) 505–521. https://doi.org/10.1016/j.jconrel.2020.05.041.

[232]T. Ahlfeld, G. Cidonio, D. Kilian, S. Duin, A.R. Akkineni, J.I. Dawson, S. Yang, A. Lode, R.O.C. Oreffo, M. Gelinsky, Development of a clay based bioink for 3D cell printing for skeletal application, Biofabrication 9 (2017) 34103. https://doi.org/10.1088/1758-5090/aa7e96.

[233]S. Afewerki, Magalhães, L. S. S. M., A.D.R. Silva, T.D. Stocco, E.C.S. Filho, F.R. Marciano, A.O. Lobo, Bioprinting a Synthetic Smectic Clay for Orthopedic Applications, Advanced healthcare materials 8 (2019).

[234]H. Mao, L. Yang, H. Zhu, L. Wu, P. Ji, J. Yang, Z. Gu, Recent advances and challenges in materials for 3D bioprinting, Progress in Natural Science: Materials International 30 (2020) 618–634. https://doi.org/10.1016/j.pnsc.2020.09.015.

[235]A. Malekpour, X. Chen, Printability and Cell Viability in Extrusion-Based Bioprinting from Experimental, Computational, and Machine Learning Views, Journal of functional biomaterials 13 (2022). https://doi.org/10.3390/jfb13020040.

[236]S. Lalitha Sridhar, M.C. Schneider, S. Chu, G. de Roucy, S.J. Bryant, F.J. Vernerey, Heterogeneity is key to hydrogel-based cartilage tissue regeneration, Soft Matter 13 (2017) 4841–4855. https://doi.org/10.1039/c7sm00423k.

[237]T. Moschakis, Microrheology and particle tracking in food gels and emulsions, Current Opinion in Colloid & Interface Science 18 (2013) 311–323. https://doi.org/10.1016/j.cocis.2013.04.011.

[238]B.R. Maciel, K. Wang, M. Müller, C. Oelschlaeger, N. Willenbacher, Targeted Micro-Phase separation – A generic design concept to control the elasticity of extrudable hydrogels, Materials & Design 227 (2023) 111803. https://doi.org/10.1016/j.matdes.2023.111803.

[239]M. McKenna, D. Shackelford, H. Ferreira Pontes, B. Ball, E. Nance, Multiple Particle Tracking Detects Changes in Brain Extracellular Matrix and Predicts Neurodevelopmental Age, ACS nano 15 (2021) 8559–8573. https://doi.org/10.1021/acsnano.1c00394.

[240]S. Neser, Bechinger C., Leiderer P., Palberg T., Finite-Size Effects on the Closest Packing of Hard Spheres, Phys. Rev. Lett. 79 (1997) 2348–2351.

[241]R. Bubeck, Bechinger C., Neser S., Leiderer P., Melting and Reentrant freezing of Two-Dimensional Colloidal Crystals in Confined Geometry, Phys. Rev. Lett. 82 (1999) 3364–3367.

[242]J.C. Crocker, D.G. Grier, Methods of Digital Video Microscopy for Colloidal Studies, J. Colloid Interface Sci. 179 (1995) 298–310.

[243]D. Wirtz, Particle-Tracking Microrheology of Living Cells: Principles and Applications, Annu. Rev. Biophys. 38 (2009) 301–326.

[244]N. Pawar, H.B. Bohidar, Surface selective binding of nanoclay particles to polyampholyte protein chains, The Journal of chemical physics 131 (2009) 45103. https://doi.org/10.1063/1.3184803.

[245]W.D. Callister JR., Fundamentals of Materials Science and Engineering, 5th ed., John Wiley & Sons, Inc., New York, 2001.

[246]M.M. Islam, D.R. Lester, Superposed shear and compression of strong colloidal gels, Journal of Rheology 65 (2021) 837–853. https://doi.org/10.1122/8.0000258.

[247]B. Sung, J. Krieger, B. Yu, M.-H. Kim, Colloidal gelatin microgels with tunable elasticity support the viability and differentiation of mesenchymal stem cells under pro-inflammatory conditions, Journal of biomedical materials research. Part A 106 (2018) 2753–2761. https://doi.org/10.1002/jbm.a.36505.

[248]S.M. Hull, L.G. Brunel, S.C. Heilshorn, 3D Bioprinting of Cell-Laden Hydrogels for Improved Biological Functionality, Advanced materials (Deerfield Beach, Fla.) 34 (2022) e2103691. https://doi.org/10.1002/adma.202103691.

[249]A. Marnot, A. Dobbs, B. Brettmann, Material extrusion additive manufacturing of dense pastes consisting of macroscopic particles, MRS Communications (2022). https://doi.org/10.1557/s43579-022-00209-1.

[250]V.B. Djagny, Z. Wang, S. Xu, Gelatin: a valuable protein for food and pharmaceutical industries: review, Critical reviews in food science and nutrition 41 (2001) 481–492. https://doi.org/10.1080/20014091091904.

[251]A.B. Bello, D. Kim, D. Kim, H. Park, S.-H. Lee, Engineering and Functionalization of Gelatin Biomaterials: From Cell Culture to Medical Applications, Tissue engineering. Part B, Reviews 26 (2020) 164–180. https://doi.org/10.1089/ten.teb.2019.0256.

Notations

Abbreviations

AFM atomic force microscopy

DLS dynamic light scattering

DMEM Dulbecco Modified Eagle Medium

$DPBS^{-/-}$ Dulbecco's phosphate-buffered saline, without magnesium and calcium

DWS diffusing wave spectroscopy

EBB extrusion-based bioprinting

FRESH freeform reversible embedding of suspended hydrogels

FTIR Fourier-transform infrared spectroscopy

GDL D-Glucono-1.5-lacton

GSE generalized Stokes-Einstein equation

HepG2 hepatocellular carcinoma

H-NMR proton nuclear magnetic ressonance

ICF intensity autocorrelation function

MPT multiple particle tracking

MRM micro-rheo-mapping

MSD mean square displacement

µCT micro-tomography

NHDF normal human dermal fibroblasts

NICE nanoengineered ionic-covalent entanglement

OSF Odijk-Skolnick-Fixman

PAV piezo-driven axial vibrator

PBS phosphate-buffered saline

PP polypropylene

PTFE polytetrafluoroethylene

PVA poly(vinyl alcohol)

SAXS small-angle x-ray scattering

SEM scanning electron microscopy

XRD x-ray diffraction

Symbols

A [m²] area

l_B [m] Bjerrum length

t_c [s] characteristic time constant

C [-] circularity

c [wt.%];[mol.l^{-1}] concentration

c_e [wt.%];[mol.l^{-1}] entanglement concentration

c_f [mol.l^{-1}] free ion concentration

c_s [mol.l^{-1}] excess salt concentration

c_i [mol.l^{-1}] ion concentration

c^* [wt.%];[mol.l^{-1}] overlap concentration

d [m] diameter

D [m².s^{-1}] diffusion coefficient

E_A [J.mol^{-1}] activation energy

h [mm] gap height

I [mol.l^{-1}] ionic strength

z_i [-] ion charge

k_B [J.K^{-1}] Boltzmann constant

L [m] length

l_p [nm] persistence length

$l_{p,0}$ [nm] intrinsic persistence length

$l_{p,e}$ [nm] electrostatic persistence length

$\Delta r^2(\tau)$ [µm²] mean square displacement

M_w [kg.mol^{-1}] molar mass

F_N [N] normal force

G' [Pa] storage modulus

G'' [Pa] loss modulus

G_0 [Pa] plateau shear modulus

G^* [Pa] complex shear modulus

n [s^{-1}] plate rotational velocity

x [mm] position along a printed strut

Pe [m] perimeter

P_r [-] printability index

r [mm] radius

R; a [m] radius of tracer particle

R_z [µm] roughness

T [K] temperature

T_c [K] critical temperature

T_0 [s] shortest Rouse relaxation time

T_r [ms] terminal relaxation time

t [s] time

V_s [$mm.s^{-1}$] slip velocity

G' [Pa] storage modulus

E [Pa] Young's modulus

x^n [-] n^{th} moment of the probability distribution of particle displacement

Greek symbols

ω [$rad.s^{-1}$] angular frequency

γ_{app} [-] apparent elastic deformation

β [$Pa.m^4$] bending modulus

κ [m] Debye-Hückel screening length

ω_0 [$rad.s^{-1}$] inverse of the shortest relaxation time

ξ [m] network mesh size

α [-] non-Gaussian parameter

ΔP [Pa] pressure difference

δ [-] scaling exponent

$\dot{\gamma}$ [s^{-1}] shear rate

τ [Pa] shear stress

τ_A [Pa] shear stress amplitude

τ_S [Pa] slip stress

τ_B [Pa] breakage stress

γ [-] true elastic strain

γ_A [-] strain amplitude

η [Pa.s] shear viscosity

$|\eta^*|$ [Pa.s] complex viscosity

η_s [Pa.s] solvent viscosity

η_{sp} [-] specific viscosity

η_0 [Pa.s] zero shear viscosity

τ [s] lag time

τ_w [Pa] wall shear stress

τ_y [Pa] yield stress